MUON RECONSTRUCTION AND PHYSICS COMMISSIONING OF THE CMS EXPERIMENT WITH COSMIC MUONS

A Dissertation

Submitted to the Faculty

of

Purdue University

by

Chang Liu

In Partial Fulfillment of the

Requirements for the Degree

of

Doctor of Philosophy

December 2009

Purdue University

West Lafayette, Indiana

To my parents, G. Y. Liu and Z. X. Zhu

ACKNOWLEDGMENTS

While I was working on my thesis I had the pleasure to collaborate with many passionate and intelligent people and I have learned a lot from them. I would like to express my thanks to them here.

I am most grateful to my supervisor Prof. Norbert Neumeister for his full guidance throughout the course of this thesis. The thesis would have never reached its current status without his encouragement. Thank him also for teaching me everything to be a physicist, programmer, and researcher.

I would like to thank my Purdue colleagues, Edwin Antillon, Adam Everett, Hwidong Yoo, and Prof. David Miller. They have kindly offered their valuable help which made my life much easier. I thank Prof. Cui, Jones, and Love for being my committee members. They have taught me wonderful physics courses and encouraged me to survive the course.

I would like to thank my CMS colleagues working on software development within the muon physics object group, especially Nicola Amapane, Riccardo Bellan, Ivan Belotelov, Ingo Bloch, Dmytro Kovalskyi, Vyacheslav Krutelyov, Martijn Mulders, Jim Pivarski, and Slava Valuev, as well as colleagues outside the muon POG, Boris Mangano, Ianna Osborne, Nhan Tran, and Giuseppe Zito. Grazie!

For the physics analyses, I had significant collaboration with Dimitri Bourilkov, Ivan Furic, Nick Kypreos, Jonatan Piedra, and Michael Schmitt from the University of Florida. They have been extremely helpful and supportive. I also had a fruitful collaboration and productive discussions with Maria Aldaya, Philipp Biallass, Francesca Cavallo, Senka Djuric, Alessandra Fanfani, Kerstin Hoepfner, Anna Meneguzzo, Ivan Mikulec and Michael Unger while conducting my analyses. The cosmic analyses were guided by Pablo Garcia and Luca Malgeri, who have been consistently supportive regardless of the slow progress we had. I thank them very much.

The technical staff at the Purdue Tier-2 center were always available and willing to help. Most of my analysis could not be conducted without their work. Thanks to David Braun, Fengping Hu, Preston Smith, and Haiying Xu.

The draft of this thesis was proofread by Heather Anthrop, Adam Everett, Yu Zheng Prof. David Miller, Prof. Norbert Neumeister and the committee members. Boyang Liu has read and corrected the theory part.

I thank my friends outside particle physics who made my life more colorful. I appreciate Yu Zheng's support which made this hard time easier. Last but not least, I thank my parents for their life long education, unconditional support, and patience. I am sorry for not visiting them more often.

TABLE OF CONTENTS

Page

LIST OF TABLES

LIST OF FIGURES

Figure Page

ABSTRACT

Liu, Chang Ph.D., Purdue University, December 2009. Muon Reconstruction and Physics Commissioning of the CMS Experiment with Cosmic Muons. Major Professor: Neumeister N. Professor.

In this thesis, the first physics measurements using the Compact Muon Solenoid (CMS) at the Large Hadron Collider (LHC) are presented. These physics measurements were performed using cosmic ray muons traversing the CMS detector. The CMS detector is optimized for the detection of muons and the results presented here also have a purpose of helping in the commissioning of the detector for the LHC collisions.

Two analyses were conducted; the first is a measurement of the charge ratio of positive to negative muons, and the second is a measurement of the differential and absolute flux of incident cosmic rays. The charge ratio measurement was made using both the muon and tracking detectors and is highlighted by its data-driven method. The charge ratio over the momentum range starting from 10 GeV were measured at the detector center and then transferred to the earth's surface. The flux measurement was performed using the muon system only and more relied on Monte Carlo samples. The flux was measured over the momentum range from 15 GeV to over 1 TeV at the CMS outer surface and then transferred to the earth's surface. These measurements required the development of specialized reconstruction and analysis tools since cosmic rays pass through the CMS detector in a different pattern than the particles from the LHC collisions. Good precision and agreement with previous experiments was observed. These measurements demonstrate the capability of the CMS detector for physics analyses and are the first physics result of the CMS collaboration.

Besides the cosmic muon analyses, an analysis of Monte Carlo samples, with full detector simulation and reconstruction of collisions at 10 TeV, was performed. This

analysis focused on the fundamental Drell-Yan process as an essential part of discovery physics in the dimuon channel. The results show that it is possible to measure the cross section precisely with the first 100 pb^{-1} data from the LHC, and the systematic uncertainty is dominated by the expected uncertainty in the luminosity measurement.

1. INTRODUCTION

Humanity's quest to understand the world in which we live has a history as long as human civilization. Starting from the era of Sir Isaac Newton, the experimental tools physicists use to explore the deep mysteries of the universe became more and more powerful and sophisticated. At the frontier of physics, particle physics studies the most elementary constituents of matter and the interactions between them. To the best of our current knowledge in the field, all known elementary particles and interactions can be described by a theory called the Standard Model of particle physics. In this model, the world is constituted by matter particles, interacting by strong, weak, and electromagnetic forces through mediating gauge bosons.

The Standard Model is one of the greatest achievements of particle physics in the 20th century. Despite the striking success of the Standard Model, there are many unsolved problems such as the large hierarchy in energy scales, the presence of dark matter in the universe, and the origin of the many fundamental parameters. While in general we do not know what the relevant energy scale is for the solution of the above problems, the electroweak scale is pointing us to new phenomena at the TeV scale. Many theoretical models beyond the Standard Model have predicted that there will be new physics at the TeV scale.

To further study the properties of the elementary particles, experimental particle physicists utilize large particle accelerators to accelerate particles to the highest achievable energies and bring them to collision. The higher the center-of-mass energy of the collision, the more likely it is to produce new particles. In particular, the trillion electron-volt (TeV) region of energy is of special interest because it may provide the answers to some of the most pressing questions in particle physics. The Large Hadron Collider (LHC) is built for this purpose. The accelerator will have the highest energy and the most intense beams in the world. It is being commissioned at

the European Organization for Nuclear Research (CERN) and has started 900 GeV collisions in Winter 2009. The Compact Muon Solenoid (CMS) experiment is one of the two general-purpose experiments at the LHC. The CMS detector is designed to detect and measure precisely all particles that will be generated by the p-p collisions, from which exotic physics processes indicating new physics phenomena could be found.

I anticipated and prepared to search for new physics in the dimuon channel once the LHC is turned on. Before any discovery of new physics can be claimed at the LHC, a detailed understanding of the detector has to be demonstrated through the precise measurement of Standard Model processes. The Drell-Yan process provides a very clean signature and can be regarded as a 'standard candle' at the LHC.

In order to be able to discover any new physics and to make precise measurements, robust and efficient online selection and offline reconstruction software is essential. My main activity in the CMS collaboration has been to prepare tools for early data analysis and detector commissioning, mainly focusing on the reconstruction of muons. In particular I developed new algorithms for global and cosmic muon reconstruction and made important contributions to the muon high-level trigger system. The software commissioning required not only the development of new components but also a revision of the entire muon reconstruction strategy, and resulted in an overall improvement of the muon reconstruction performance.

In the process of preparing for collisions at the LHC, the schedule of the commissioning of the LHC was delayed several times due to various reasons. At the end of 2006, the LHC was expected to start with a pilot run at the end of 2007 followed by a first physics run in Spring 2008. However, the commissioning of the LHC was then delayed to September 2008 and the analysis was anticipated to finish in Spring 2009. On September 10, 2008, the LHC beam was successfully accelerated to 5 TeV for the first time. However one week later, a magnet quench occurred and six tons of helium leaked from the LHC, which delayed the collisions for at least a year. Nature always

sides with the hidden flaw, as does the LHC. It is not a surprise that a large complex instrument such as the LHC was bitten by Murphy's law.

In spite of the disappointment of the incident, and also the fact that the CMS detector is by no means designed as a cosmic muon spectrometer, the CMS collaboration used the commissioned CMS detector to collect particles from a much larger accelerator, the universe, which provides ultra high energy beams that are unrivaled by artificial sources. In addition, there are still physics topics concerning the properties of the particle spectra from cosmic rays. The cosmic muon measurements from the CMS experiment can also contribute to the understanding of the cosmic ray sources. More important, the measurements can demonstrate the great potential of the CMS detector to produce high-quality physics measurements. During the Cosmic Run at Four Tesla (CRAFT) in October and November 2008, about 300 million cosmic events were recorded with the full detector. This provided a significant amount of data which allowed the study of detector performance and physics analyses using cosmic rays.

I significantly contributed to two physics analyses: the measurement of the charge ratio of muons from cosmic rays and the measurement of the cosmic muon flux, which are the first physics results of the CMS collaboration. In particular I was in charge of the Monte Carlo study to understand the molasse shielding the CMS detector from cosmic rays in the charge ratio analysis. I co-led the flux measurement and contributed to many aspects of the analysis. In addition I analyzed the properties of the interaction between high energy muons and the CMS detector. For all these analyses I developed novel reconstruction and analysis tools.

Besides the study of cosmic ray muons, I performed a physics analysis based on Monte Carlo samples in preparation for first data at the LHC. In this exercise a measurement of the differential Drell-Yan cross section in the dimuon channel was conducted assuming an initial dataset of 100 pb^{-1}. The Drell-Yan dimuon production constitutes an important Standard Model background for all searches for new physics in the dimuon final state. The Drell-Yan process has been studied in the mass range, starting from the Υ peaks up to the kinematic limit. Events at the Υ and the Z

peak are used to measure the trigger and reconstruction efficiencies from data. I contributed to the development of analysis tools for measuring muon reconstruction efficiencies from data.

It is also interesting to notice that the topology of cosmic muons traversing the entire CMS detector looks very similar to dimuon events from LHC collisions, as illustrated in figure 1.1. The cosmic muon analysis effort is, therefore, an excellent dress rehearsal for the analysis of physics processes with a dimuon signature at the LHC.

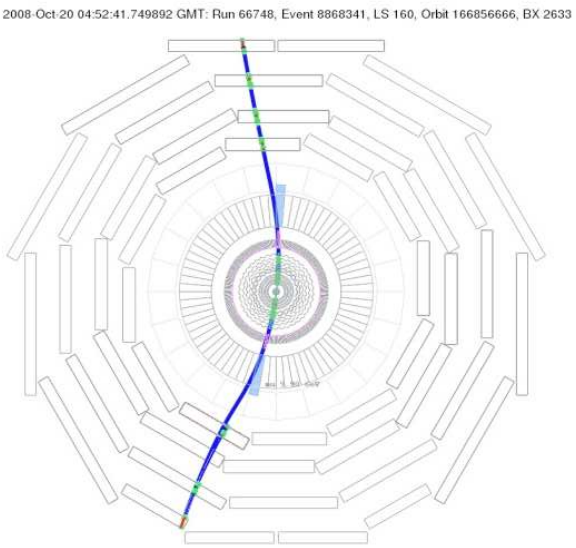

Figure 1.1. A cosmic muon traversing the whole CMS detector looks like an event with two muons which are produced back-to-back at the center of the detector.

This thesis is arranged in the following order. After this brief introduction, a general theoretical background and motivations for high energy physics research and the Large Hadron Collider is described in Chapter 2. The design and performance of the CMS detector is described in Chapter 3. In Chapter 4 a description of the muon reconstruction is presented. Particular emphasis is given to the parts I contributed to. In Chapter 5 the muon high-level trigger system is described with emphasis on the level-3 muon trigger algorithm. In Chapter 6, several physics analyses with cosmic

ray muons are presented. The study on the measurement of the differential Drell-Yan production cross section is described in Chapter 7.

2. THEORY

This chapter gives a short overview of the Standard Model (SM) and describes the the Drell-Yan process, followed by a brief introduction to theoretical models beyond the SM. More details about the SM can be found in [1–3].

2.1 The Standard Model

The SM of particle physics is the most successful achievement of modern particle physics. It is based on two fundamental symmetries: Lorentz invariance and gauge symmetry. The SM describes how matter is composed of elementary particles and how matter interacts in the form of electromagnetic, weak, and strong forces. It unifies the electromagnetic and the weak forces, and incorporates the strong force.

In the SM, matter is composed of fundamental fermions. There are twelve kinds of fundamental fermions divided into two categories, leptons and quarks. The leptons include electrons, muons, taus, and their corresponding neutrinos. The quarks include up, down, charm, strange, top, and bottom quarks. Quarks have fractional charges and can not exist freely in nature. The difference between the two categories of fermions is that leptons do not experience strong interactions, while quarks do. A complete list of these fundamental fermions is given in table 2.1. The interactions between them are described in terms of the exchange of integer spin gauge bosons. Electromagnetic, weak, and strong forces are exchanged by photons, Z and W bosons, and gluons, respectively.

The SM provides a unified framework to describe these three forces based on the electroweak theory describing electromagnetic and weak interactions between quarks and leptons [4–6] and quantum chromo-dynamics (QCD) [7–10]. The Standard Model is based on the principle of local gauge symmetry under the gauge group $SU(3)_C \otimes$

$SU(2)_L \otimes U(1)_Y$ and on spontaneous breakdown of the $SU(2)_L \otimes U(1)_Y$ symmetry to the $U(1)_Q$ symmetry of QED via the Higgs mechanism.

The electroweak gauge symmetry group $SU(2)_L \otimes U(1)_Y$ has four generators, the weak isospin I_1, I_2, I_3 and the weak hypercharge Y. Local gauge symmetry invariance requires that each of these generalized charges is associated with a vector field. The non-Abelian weak isospin group $SU(2)_L$ introduces three massless vector bosons, which couple with strength g to all left-handed fermions. The Abelian group $U(1)_Y$ introduces one massless vector boson, which couples with strength g' to all particles with a weak hypercharge Y. The theory of the strong interactions between colored (C) quarks is based on the $SU(3)_C$ group.

In the SM all interactions between fermions and bosons are the result of the gauge symmetries. For example, electromagnetic interactions between fermions and photons arise naturally by requiring local gauge invariance of the Dirac Lagrangian of free fermions $\mathcal{L}_F = \bar{\psi}(i\gamma \cdot \partial - m)\psi$. This Lagrangian is not invariant under the $U(1)$ transformation $\psi \rightarrow e^{ie\Lambda(x)}\psi$. However if one introduces a gauge field A_μ, which transforms like $A_\mu \rightarrow A_\mu - \partial_\mu \Lambda(x)$, and defines $D_\mu \equiv \partial_\mu + ieA_\mu$, then $\mathcal{L}_F$ takes a new form of $\mathcal{L}_F + \mathcal{L}_{GF}$ ($\mathcal{L}_{GF} = -e\bar{\psi}\gamma^\mu\psi A_\mu$), which is now invariant under $U(1)$ transformation. The term $\mathcal{L}_{GF}$ presents the coupling between the fermion ψ and the gauge field A_μ. The Lagrangian of a free photon $\mathcal{L}_G = -\frac{1}{4}F_{\mu\nu}F^{\mu\nu}$, where $F_{\mu\nu} = \partial_\mu A_\nu - \partial_\nu A_\mu$, is invariant under the gauge transformation. These Lagrangians describe the quantum electrodynamics (QED).

However, all particles in the SM are massless up to this point. Any mass term for the gauge bosons would violate the gauge invariance. A mechanism to introduce masses in the SM is called the Higgs mechanism [11,12]. It describes the spontaneous symmetry breaking of $SU(2)_L \otimes U(1)_Y$ to the $U(1)_Q$ symmetry by introducing the Higgs field, a $SU(2)$ doublet of complex scalar fields, $\Phi = (\phi^+, \phi^0)^T$. The Lagrangian of this field must be invariant under $SU(2)_L \otimes U(1)_Y$ local gauge transformations and includes a special potential term $-\mu^2\Phi\Phi^\dagger + \lambda(\Phi\Phi^\dagger)^2$. The minimum point of

Name (Abbreviation)	Charge(e)	Mass	Interactions
down (d)	-1/3	3 to 7 MeV	electroweak, strong
up (u)	2/3	1.5 to 3 MeV	electroweak, strong
strange (s)	-1/3	95 ± 25 MeV	electroweak, strong
charm (c)	2/3	1.25 ± 0.09 GeV	electroweak, strong
bottom (b)	-1/3	4.20 ± 0.07 GeV	electroweak, strong
top (t)	2/3	174.2 ± 3.3 GeV	electroweak, strong
electron (e)	-1	0.51099892(4) MeV	electroweak
muon (μ)	-1	105.658369(9) MeV	electroweak
tau (τ)	-1	$1776.99^{+0.29}_{-0.26}$ MeV	electroweak
electron neutrino (ν_e)	0	~ 0	weak
muon neutrino (ν_μ)	0	~ 0	weak
tau neutrino (ν_τ)	0	~ 0	weak

Table 2.1
Table of fundamental fermions.

this potential term is not at the origin, but a manifold of values. The Higgs doublet $\Phi = (\phi^+, \phi^0)^T$ then take the form of $(0, \frac{(v+H)}{\sqrt{2}})^T$, where $v^2 = \frac{\mu^2}{\lambda}$.

Name (Abbreviation)	Charge(e)	Mass	Interactions
photon (γ)	0	0	Electromagnetic
Z^0	0	91 GeV	Weak
$W^\pm$	± 1	89 GeV	Weak
8 colored gluons	0	0	Strong

Table 2.2
Table of fundamental bosons.

The $SU(2)_L$ transformation acts on left-handed doublets and right-handed singlets. The invariance introduces four massless vector fields, $W_\mu^{1,2,3}$ and B_μ, that couple to fermions with two coupling constants, g and g'. The physical fields $W^\pm$, γ, and Z, are linear combinations of the four vector fields: $W_\mu^\pm = \sqrt{\frac{1}{2}}(W_\mu^1 \pm \imath W_\mu^2)$, and $A_\mu = B_\mu \cos\theta_W + W_\mu^3 \sin\theta_W$, respectively. The Weinberg angle θ_W is defined as the mixing angle of the neutral fields W_μ^3 and B_μ, and the relation $g \sin\theta_W = g' \cos\theta_W = e$ is concluded, which presents the electroweak unification.

Masses of fermions and gauge bosons W^+, W^-, and Z^0 are generated by the couplings of the non-zero vacuum expectation value of the Higgs field to them, while the photon is massless. The Higgs mechanism also predicts the existence of one additional scalar gauge boson, called the Higgs boson. The search for the Higgs boson has been a main focus of current high energy experiments.

2.2 Physics of Proton-Proton Collisions

The LHC was conceived to accomplish the important task of shedding light on the consistency of the SM at energy scales up to about 1 TeV and to study the spontaneous electroweak symmetry breaking. Besides this, a wide research program including different physics topics has been developed at the LHC.

Protons are composed of more elementary partons (quarks and gluons). In high energy inelastic proton collisions, partons are involved in the interactions. The effective center-of-mass energy $\sqrt{\hat{s}}$, is proportional to the fractional energies carried by the two interacting partons, $\sqrt{\hat{s}} = \sqrt{s x_a x_b}$, where x_a and x_b are the parton's fractions of the total proton energy, and $\sqrt{s}$ is the center-of-mass energy of the proton beams.

The momentum distribution of the partons inside the protons is described by the parton density functions (PDFs). The PDFs are different for valence quarks, sea quarks, and gluons. They are functions of the exchanged four-momentum squared, Q^2. PDFs are measured and fitted from experimental data in various regions. Two examples of PDFs under two different Q-values are shown in figure 2.1.

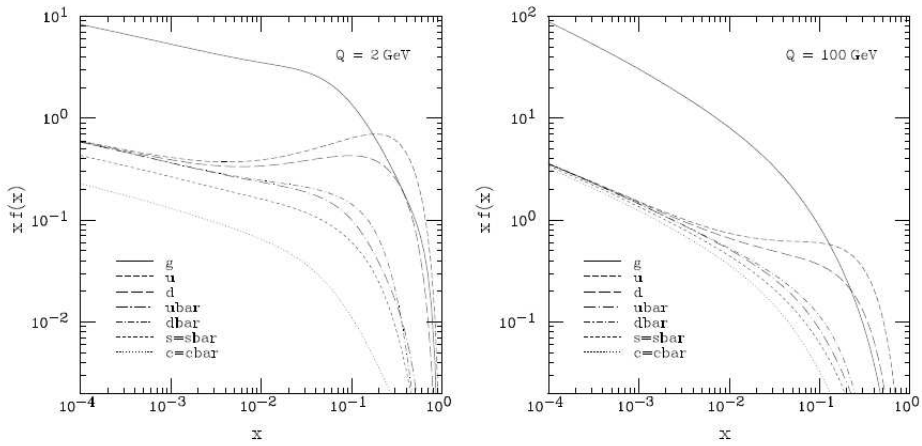

Figure 2.1. The parton density functions for $Q = 2$ and $Q = 100$ GeV [13].

The effective center-of-mass energies carried by the interacting partons are unknown. Many partons are scattered at small angles and lost in the beam pipe, and the center-of-mass may be boosted along the beam direction. Experimentally it is necessary to use quantities that are invariant under Lorentz boosts along the beam line, such as rapidity and transverse momentum. Rapidity is defined as $y = \frac{1}{2}\ln(\frac{E+p_z}{E-p_z})$ and transverse momentum (p_T) is defined as the component of the particle momentum which is transverse to the beam line. $p_T = |\vec{p}| \cdot \sin\theta$.

2.3 The Drell-Yan Process

The lepton pair production mechanism via quark-antiquark annihilation by the exchange of a virtual photon or Z-boson is known as the "Drell-Yan" process [14]. The process has a clean signature and low experimental backgrounds. Measurements of Drell-Yan production have historically been good probes of the structure of the proton and are important for understanding of QCD. The measurement of the Drell-Yan cross section is also a prerequisite for the discovery of new physics.

Figure 2.2 shows the leading order Feynman diagram of the Drell-Yan process in p-p collisions. A quark and an antiquark annihilate to produce a virtual photon or Z boson, which then decays into an opposite-sign lepton pair.

In this section, the theory of Drell-Yan production is described within the naive parton model. In this model, protons are made up of partons, and all parton-parton interactions are ignored.

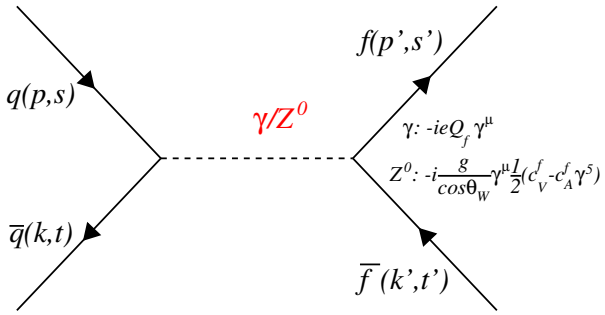

Figure 2.2. Illustration of the leading order Drell-Yan process.

The scattering amplitude of the process as illustrated in figure 2.2 has the form

$$S(q\bar{q} \xrightarrow{\gamma/Z^0} f\bar{f}) = \frac{(2\pi)^4\delta^4(p'+k'-p-k)}{4V^2(p_0k_0k'_0p'_0)^{1/2}}(A_\gamma + A_Z) \tag{2.1}$$

Where A_γ and A_Z are

$$\begin{aligned} A_\gamma &= -if(p',s')i(eQ_f)\gamma^\mu \bar{f}(k',t') \\ &\times \frac{g_{\mu\nu} - ((k+p)_\mu(k+p)_\mu)/(k+p)^2)}{(k+p)^2} \\ &\times i\bar{q}(k,t)i(eQ_q)\gamma^\nu q(p,s) \end{aligned} \tag{2.2}$$

$$\begin{aligned} A_Z &= -if(p',s')(-i)\frac{g}{cos\theta_W}\gamma^\mu\tfrac{1}{2}(c_V^f - c_A^f\gamma^5)\bar{f}(k',t') \\ &\times \frac{g_{\mu\nu} - ((k+p)_\mu(k+p)_\mu)/M_Z^2)}{(k+p)^2 - M_Z^2 + i\epsilon} \\ &\times i\bar{q}(k,t)(-i)\frac{g}{cos\theta_W}\gamma^\nu\tfrac{1}{2}(c_V^f - c_A^f\gamma^5)q(p,s) \end{aligned} \tag{2.3}$$

Where c_V^f and c_A^f are the vector and axial-vector coupling constants. They are determined in the electroweak spontaneous symmetry breaking. For charged leptons, $c_V^f = -\frac{1}{2}$ and $c_A^f = -\frac{1}{2} + 2\sin^2\theta_W \approx -0.03$.

The differential cross section can then be written as

$$\frac{d\hat{\sigma}[q\bar{q} \to f\bar{f}]}{d\Omega} = \frac{(2\pi)^4}{32k_0|p|}\frac{1}{4}\sum_{s,s',t,t'}\int_0^\infty \frac{|p'|^2 d|p'|}{(2\pi)^3 p_0'}\int \frac{d^3k'}{(2\pi)^3 k_0'}\delta^4(p'+k'-p-k)|A_\gamma + A_Z|^2 \tag{2.4}$$

In the naive parton model, the cross section of the leading order contribution is

$$\hat{\sigma}[q\bar{q} \to l^+l^-] = \frac{4\pi\alpha^2}{9M^2}e_q^2 \tag{2.5}$$

where e_q is the charge of the quark and M is the invariant mass of the lepton pair.

The differential cross section $\frac{d\hat{\sigma}}{dx_a dx_b}$ is

$$\frac{d\hat{\sigma}[q\bar{q} \to l^+l^-]}{dx_a dx_b} = G_q(x_a)G_{\bar{q}}(x_b)\hat{\sigma}[q\bar{q} \to l^+l^-] \tag{2.6}$$

where $G_q(x_a)$ is defined as the probability of finding a quark q, with x_a, $G_{\bar{q}}(x_b)$ is defined as the probability of finding an antiquark $\bar{q}$, with x_b, where x , is the fraction of the longitudinal momentum carried by a given parton of the hadron, $p_q = x_a P_p$, and $p_{\bar{q}} = x_b P_{\bar{p}}$, where P_p and $P_{\bar{p}}$ are the momenta of the proton and antiproton respectively.

The expression can be further simplified by introducing the Mandelstam variables

$$s \equiv (P_p + P_p)^2 \tag{2.7}$$

$$\hat{s} \equiv (p_q + p_{\bar{q}})^2 = x_a x_b s \tag{2.8}$$

and

$$\tau \equiv M^2/s = s x_a x_b \ . \tag{2.9}$$

After putting in all these ingredients, the differential cross section becomes

$$\frac{d^2\sigma}{d\tau dx_L} = \frac{4\pi\alpha^2}{9M^2}\frac{1}{(x_a + x_b)}\sum e_q^2[G_q(x_a)G_{\bar{q}}(x_b) + G_{\bar{q}}(x_a)G_q(x_b)] \tag{2.10}$$

where $x_L = x_a - x_b$, and after integrating it,

$$\frac{d\sigma}{d\tau} = \frac{4\pi\alpha^2}{9M^2}\int_\tau^1 \frac{dx_a}{x_a}\sum e_q^2[G_q(x_a)G_{\bar{q}}(\frac{\tau}{x_a}) + G_{\bar{q}}(x_a)G_q(\frac{\tau}{x_a})] = \frac{1}{M^2}\mathcal{F}(\tau) \tag{2.11}$$

which can also be expressed as

$$\frac{d\sigma}{dM} = \frac{1}{M^3}\mathcal{F}'(\tau) \tag{2.12}$$

Thus, the leading-order Drell-Yan differential cross section depends on $\tau \equiv \frac{M^2}{s}$ only.

The Drell-Yan model leads to the prediction of a simple decay angular distribution of the leptons in the rest frame of the dilepton pair. The spin of the γ/Z generated from annihilation is aligned along the beam axis. The amplitude for the decay into a dilepton pair is

$$A(\theta,\psi) = \uparrow\uparrow Y_0^1(\theta,\psi) + \uparrow\downarrow Y_1^1(\theta,\psi) \tag{2.13}$$

where the arrows indicate the spin alignments of the leptons (up being parallel to the beam, and down being the opposite), and Y are the spherical harmonic functions of the polar angles θ and ψ with respect to the beam axis.

The angular distribution is

$$\frac{d\sigma}{d\Omega} = |A(\theta,\psi)|^2 \tag{2.14}$$

integrating over the azimuth angle ψ, the differential cross section becomes

$$\frac{d\sigma}{d\theta} = 1 + \cos^2\theta\ . \tag{2.15}$$

However, the above θ is in the center-of-mass frame of the quark-antiquark system. It is not directly measurable in the lab frame because the input quarks also have initial transverse momentum p_T. The Collins-Soper reference frame [15], in which angles are measured with respect to the axis that bisects the two beam axes in the dimuon center-of-mass frame, is generally regarded as the best frame for minimizing the effect of p_T on the measurement of $\cos\theta$. The angular distribution is an important quantity to measure for possible discovery of new physics.

The Drell-Yan process provides an adequate explanation of high-mass continuum lepton pair production by hadrons and is in great agreement with all experimental measurements so far. Because of the large cross section of the process, it can be used as a bright "candle" for exploration of the physics beyond the SM.

2.4 Physics Beyond the Standard Model

Although the SM has been experimentally confirmed with high accuracy, there are a number of shortcomings and problems with it. The SM does not include gravity, one of the four fundamental forces. There is no known way of adapting the quantum field theory with general relativity. It is expected that new physics could appear at the LHC. One exceptional example is the supersymmetry theory [16], while another category is the extra-dimension theories briefly introduced here.

In the past, physicists used to describe the world with three space dimensions until the beginning of the 20th century when Einstein introduced time as the fourth dimension [17]. In 1921, Theodor Kaluza extended the general theory of relativity to a five-dimensional space-time to unify gravity and electromagnetic forces [18]. In the theory, Einstein field equations and Maxwell's equations for the electromagnetic field have the same origin. In 1926, Oskar Klein proposed that the fifth dimension is curled up in a circle of a very small radius, so that a particle moving along that axis would return to where it began [19]. The distance a particle can travel before reaching its initial position is said to be the size of the dimension. This phenomenon of compact dimensions in space-time is referred to as compactification.

Many approaches to the unification of the forces by proposing extra dimensions is taken by modern theories, such as string theory [20] and M-theory [21]. In the 1990s, many new theories involving extra dimensions have been proposed [22–29]. Unlike string theories, these models gave experimental predictions that could be verified by colliders. They are proposed to solve the gauge hierarchy problem, the puzzle of the weakness of gravity relatively to the other three fundamental forces.

One such model is the ADD model [22], also known as the model with large extra dimensions, proposed by Nima Arkani-Hamed, Savas Dimopoulos, and Gia Dvali in 1998. It explains the hierarchy problem by imagining a universe in which the fields of the SM are confined to a higher-dimensional membrane, while gravity can propagate in several additional spatial dimensions that are compact but large.

The ADD signal may appear as a deviation of the dimuon spectra from the SM predictions for Drell-Yan processes. A variation of the model also predictes the existence of Kaluza-Klein excitation of gauge bosons, a series of Z' resonances that can be found in the dilepton channel [30].

Randall-Sundrum models [31], proposed in 1999, imagine that the real world is a higher-dimensional universe described by wrapped geometry. Our universe is a five-dimensional anti de Sitter space [32] and the elementary particles, except for the graviton, are localized on a $(3+1)$-dimensional brane or branes. There are two popular RS models. The first, called RS1, has a finite size for the extra dimension with two branes, one at each end. The second, RS2, is similar to the first, but one brane has been placed infinitely far away.

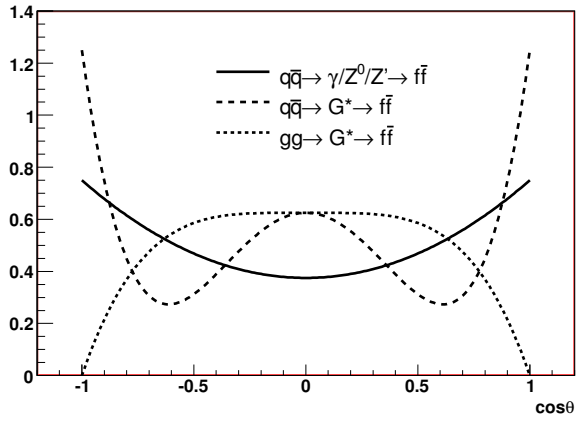

Figure 2.3. Illustration of the angular distribution shapes for spin-1 and spin-2 resonances.

The Randall-Sundrum models predict a mass spectrum of graviton excitations in the dilepton channel.

In summary, there are several possibilities of new physics showing up at the LHC. When searching for new physics in a yet-unexplored energy regime, one has to be prepared for the possibility of one or several signatures of new physics models. A discovery of a new resonance or deviation has to be followed by a detailed study to determine its theoretical origin. One characteristic feature is its spin. The spin is 2 for a graviton and 1 for a Z', which can be distinguished by the angular distributions of the decay products, as listed in table 2.3 and illustrated in figure 2.3.

Process	Angular distribution
$q\bar{q} \to \gamma/Z^0/Z' \to f\bar{f}$	$\frac{3}{8}(1+\cos^2\theta^*)$
$q\bar{q} \to G^* \to f\bar{f}$	$\frac{5}{8}(1-3\cos^2\theta^*+4\cos^4\theta^*)$
$gg \to G^* \to f\bar{f}$	$\frac{5}{8}(1-\cos^4\theta^*)$

Table 2.3
Different processes and their characteristic angular distribution.

3. THE CMS EXPERIMENT

3.1 The Large Hadron Collider

The Large Hadron Collider (LHC), currently under commissioning and testing at CERN and scheduled to start operating in 2009, provides a crucial new capability for physics research. For the next two decades the LHC will probe the TeV frontier of energies to search for new phenomena. Among currently approved projects in high energy physics the LHC uniquely has sufficient energy and luminosity to probe in detail the TeV energy scale relevant to electroweak symmetry breaking.

The LHC is installed in the existing Large Electron-Positron Collider (LEP) tunnel and utilizes the Super Proton Synchrotron (SPS) accelerator at CERN. In the LHC, proton bunches are accelerated to 7 TeV and collide head-on. In the first years of operation, the center-of-mass energy will be 7 TeV, and will increase steadily when the machine is better understood and finally should reach the design energy at 14 TeV.

The LHC bunch crossing frequency for proton-proton collisions is 40 MHz. At the design luminosity of 10^{34} $\mathrm{cm}^{-2}\mathrm{s}^{-1}$, approximately 20 interactions occur at each bunch crossing, corresponding to a total interaction rate of the order of 1 GHz. In the first years of operation, the LHC is expected to run at a much reduced luminosity starting from 10^{29} $\mathrm{cm}^{-2}\mathrm{s}^{-1}$, and only after some years of operation, the design luminosity of 10^{34} $\mathrm{cm}^{-2}\mathrm{s}^{-1}$ will be reached. The rate of interesting physics processes like the production of the Higgs bosons is more than ten orders of magnitudes smaller. The input rate of 10^9 interactions every second must be reduced by a factor of at least 10^7 to $\mathcal{O}(100)$ Hz, in order to match the capabilities of the mass storage and offline computing systems of the experiments.

Parameter	Value for p-p collision
center-of-mass energy (TeV)	14
Number of particles per bunch	1.1×10^{11}
Number of bunches	2808
Design luminosity ($\mathrm{cm}^{-2}\mathrm{s}^{-1}$)	10^{34}
Luminosity lifetime (h)	10
Bunch length (mm)	53
Beam radius at interaction point (μm)	15
Time between collisions (ns)	24.95
Bunch crossing rate (MHz)	40.08
Circumference (km)	26.659
Dipole field (T)	8.3

Table 3.1
Table of LHC design parameters for p-p collisions.

In collider physics, a certain physics process, characterized by a cross section σ, occurs with a rate R, defined as the number of events per second, which is given by

$$R = \mathcal{L}\sigma, \tag{3.1}$$

where the $\mathcal{L}$ is denoted as *luminosity*, which is defined as

$$\mathcal{L} = fk\frac{n_1 n_2}{\sigma_x \sigma_y}, \tag{3.2}$$

where f is the revolution frequency, k is the number of bunches composed of n_1 and n_2 particles and $\sigma_x\sigma_y$ is the overlapping cross sectional area (inn the x-y plane) of the beams.

The design parameters of the LHC are summarized in table 3.1. An illustration of the LHC accelerator complex is shown in figure 3.1.

There are two general purpose experiments installed at the LHC: A Toroidal LHC ApparatuS (ATLAS) and the Compact Muon Solenoid (CMS). Their designs signif-

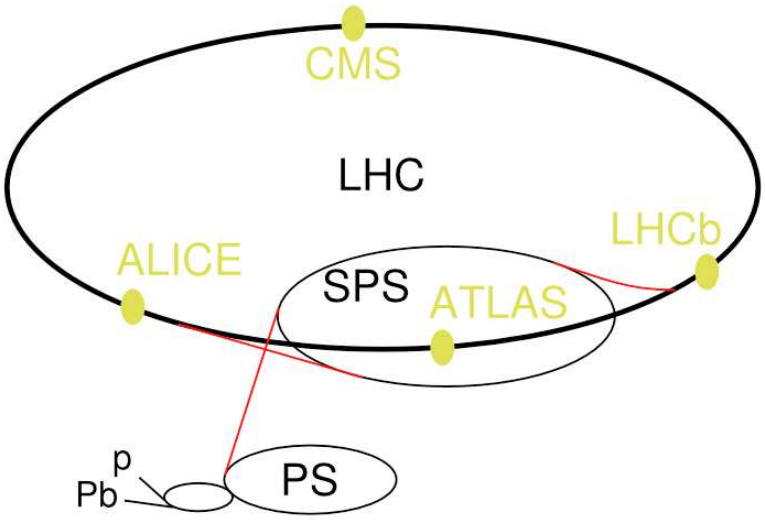

Figure 3.1. Overview of the detectors and accelerator complex at the LHC.

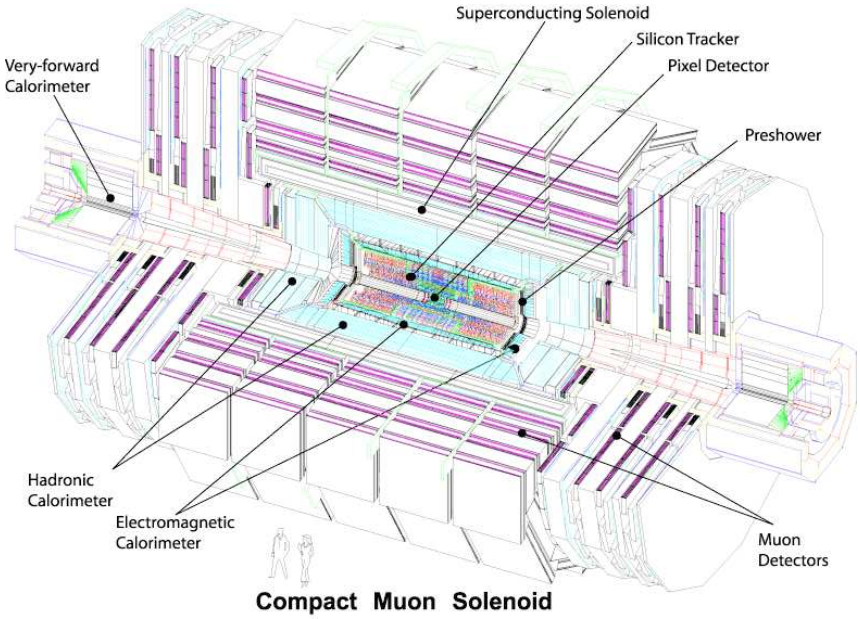

Figure 3.2. The CMS detector.

icantly differ from each other, because the CMS detector uses a solenoidal magnetic field generated by a superconducting solenoid, while the ATLAS detector uses a toroid

magnetic field generated by three sets of air-core toroids complemented by a small inner solenoid.

The CMS experiment is described in more detail in the following part of this chapter. A schematic picture of the CMS is shown in figure 3.2.

3.2 The Compact Muon Solenoid

The CMS [33,34] is a general purpose detector operating at the LHC. As its name indicates, it is designed to precisely measure muons with a relatively compact design, by utilizing a 3.8 T superconducting solenoid. The 3.8 T magnetic field allows precise tracking in the silicon inner tracker and reduces the pile-up from soft hadrons in the muon system, which is installed outside the solenoid.

3.2.1 Overall Design

The CMS detector is composed of a cylindrical barrel and two endcaps. It has a total length of 21.6 m, a diameter of 15 m, and a total weight of about 12500 tons. The design is driven by the choice of its magnet, a 13 m long superconducting solenoid [35] with a diameter of 5.9 m. From inside-out the silicon tracker, the electromagnetic calorimeter, and the hadron calorimeter are placed inside the coil. The muon chambers are embedded between iron layers of the magnetic return yoke outside the superconducting solenoid.

The reference coordinate system of the CMS experiment is defined as following. The x-axis points toward the center of the LHC circle, the y-axis points upward and the z-axis points along the beam to the Jura mountains. The three axes form a right-handed system. A pseudo-spherical coordinate system is also widely used, where r is the distance to the beam-line, ϕ is the angle with respect to the y-axis and the pseudo-rapidity η as defined in equation 3.3.

$$\eta = -\ln(\tan\frac{\theta}{2}), \tag{3.3}$$

where θ is the angle with respect to the beam line. The pseudo-rapidity is a good approximation of rapidity when a particle's momentum is much larger than its mass.

In the rest of the chapter, the detector subsystems are described with their specific characteristics, with an emphasis on the detectors involved in muon reconstruction and identification, such as the silicon tracking system and the muon system. This is followed by an overview of the CMS trigger system.

3.2.2 Tracker

The inner tracking detectors are designed to reconstruct muons, electrons, and hadrons, with good momentum resolution and high efficiencies in the range of $|\eta| < 2.5$. The resolution of the muon reconstruction is dominated by the measurements in the tracking detector, which is discussed in Section 4.

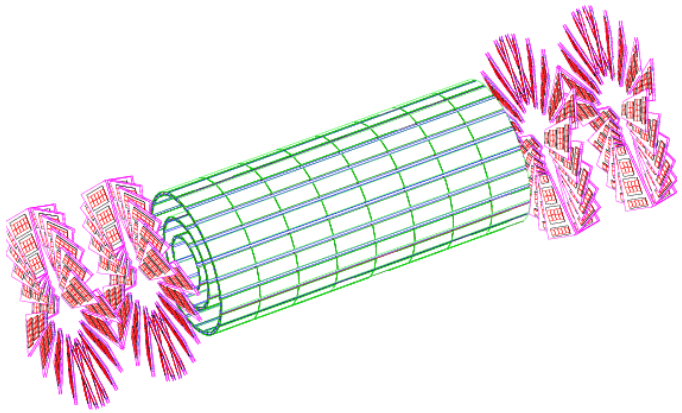

Figure 3.3. An illustration of the pixel tracker detector.

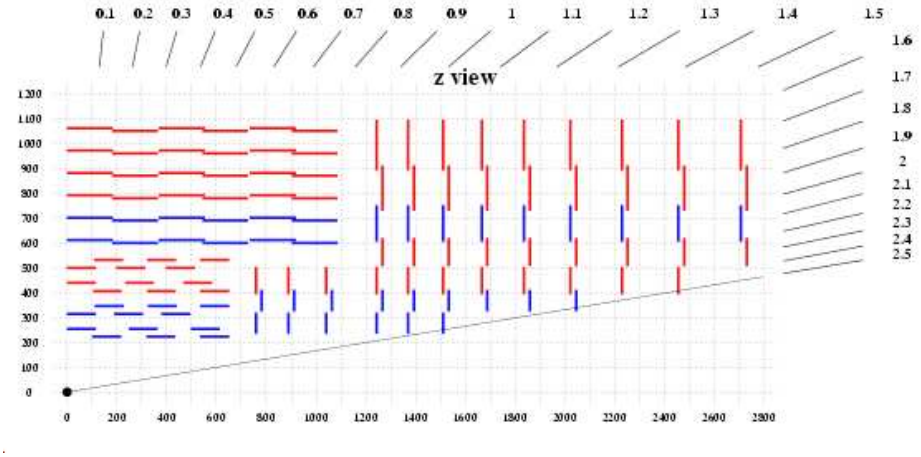

Figure 3.4. A sketch of the longitudinal view of a quarter of the silicon strip tracker. Mono modules are presented by red, and stereo modules are presented by blue.

The Pixel Detector

The pixel tracker was motivated by the need to measure the impact parameters of charged particles in order to achieve high efficiency of b-tagging and vertex reconstruction. It is the component that is closest to the interaction point. The pixel detector is composed of three barrel layers and two endcap disks at each endcap, as illustrated in figure 3.3. The barrel layers have a length of 53 cm and are located at cylinders with mean radii of 4.4 cm, 7.3 cm, and 10.2 cm respectively. The endcap layers are arranged in a turbine-like shape with a 20° tilt, covering the radius from 6 to 15 cm and are placed at $|z| = 34.5$ cm and 46.5 cm. The design of the pixel detector allows the measurement of at least two points per track in the $|\eta| < 2.2$ region for tracks originating within $2\sigma_z$ from the interaction point, where σ_z is the longitudinal size of the luminosity region of the LHC collisions, which is about 5.3 cm. The total number of the channels of the pixel detector is approximately 44 million.

The Silicon Detector

The silicon tracker based on silicon strips, is just outside the pixel tracker. The detector modules are made of p^+ strips on a n-type bulk silicon whose thickness is about 320 and 500 μm respectively in the inner and outer tracker.

As illustrated in figure 3.4, there are four inner barrel layers called tracker inner barrel (TIB) and six outer barrel layers called tracker outer barrel (TOB). At each endcap side, there are three inner layers called tracker inner disks (TID) and nine outer layers called tracker end cap (TEC).

The first two TIB layers and the first two TOB layers are made of double-sided ("stereo") modules, composed of two modules mounted back-to-back with their strips tilted by 100 mrad. The rest of the TIB and TOB are made of single-sided ("mono") modules. The whole silicon tracker is made of about 10 million channels for an active area close to 198 m^2. The components of the silicon strip tracker are listed in table 3.2.

Part	Number of detectors	mean pitch (μm)
TIB	2724	81/118
TOB	5208	81/183
TID	816	97/128/143
TEC	2512	96/126/128/143
TEC(2)	3888	143/158/183

Table 3.2
Components in the silicon strip tracker.

3.2.3 Calorimeters

Electromagnetic Calorimeter

The electromagnetic calorimeter (ECAL) was designed to measure the energy of electrons and photons. The physics motivation of the design is driven by the search for the Higgs boson in the channel $H \rightarrow \gamma\gamma$, where the H signal has to be distinguished from a continuous background in the differential di-photon invariant mass spectrum.

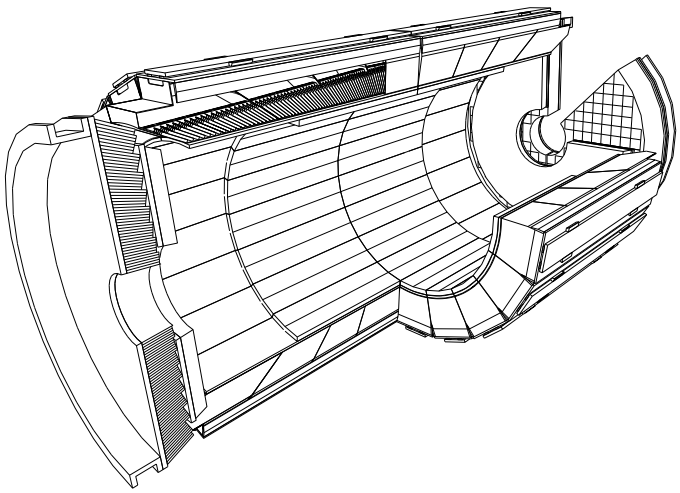

Figure 3.5. An illustration of the barrel and the endcaps of the ECAL.

The ECAL is a hermetic homogeneous calorimeter made of lead tungstate ($PbWO_4$) crystals and is placed inside the magnetic coil. Lead tungstate was chosen because of its excellent radiation hardness. Lead tungstate crystals have a short radiation length ($X_0 = 0.89$ cm) and a small Moliere radius ($R_M = 2.2$ cm). About 80% of the scintillation light is emitted within 25 ns. The ECAL is composed of 61200 crystals in the central barrel part, and 7324 crystals in each endcap, as illustrated in figure 3.5.

In the barrel, silicon avalanche photodiodes (APDs) are employed, while vacuum phototriodes (VPTs) are used in the endcaps. The temperature of the system is kept stable at 0.1°C by a water cooling system since both the crystals and the APDs

response are sensitive to temperature changes. The barrel region of ECAL covers the pseudorapidity region up to $|\eta| < 1.479$. The barrel part has an inner radius of 129 cm and is composed of 36 supermodules, each containing 1700 crystals. The barrel crystals have a front face cross section of 22×22 mm^2 and a length of 230 mm corresponding to $25.8X_0$. The granularity of the barrel is $\Delta\phi \times \Delta\eta = 0.0175 \times 0.0175$.

The endcaps cover the $|\eta|$ region from 1.48 to 3.0. The endcap crystals have dimensions of $28.6 \times 28.6 \times 220$ mm^2. A preshower device, which is introduced to identify π^0 in the endcaps, is located in front of the endcaps. Two planes of silicon strip detectors are placed behind disks of lead absorber at depths of $2X_0$ and $3X_0$.

The energy resolution of a calorimeter can be parametrized as the sum in quadrature of three different terms:

$$\frac{\sigma_E}{E} = \frac{a}{\sqrt{E}} \oplus \frac{b}{E} \oplus c \tag{3.4}$$

In the equation, a is the stochastic term, including the fluctuations in the number of electrons which reach the preamplifier (n_e). The fluctuations are proportional to $\sqrt{n_e}$ and thus proportional to E. b is the noise term, accounting for all the effects that can affect the measurements of E independently of the E, and c is the constant term related to calibration, temperature and other issues with the stability of the detector. Muons are minimum ionizing particles (MIP) and leave only a small energy deposit in the calorimeters. A 100 GeV muon usually leaves about one or two GeV in the ECAL.

Hadronic Calorimeter

The hadron calorimeter (HCAL) is placed just outside the electromagnetic calorimeter and inside the superconducting coil. The HCAL is designed to reconstruct jets and missing energy (missing E_T) with high precision. Its resolution must ensure a good reconstruction of the di-jet events and an efficient measurement of missing E_T. HCAL has to provide a large coverage and fine granularity for this purpose. It has to

be able to detect signals ranging from the signal of a single minimum ionizing muon up to a deposited energy of 3 TeV. The HCAL barrel region covers an $|\eta|$ range up to 1.74, and the endcaps cover an $|\eta|$ region up to 3. The HCAL is composed of brass layers as absorbers, interleaved by thick plastic scintillator layers. The brass layers have thicknesses of 60 mm in the barrel and 80 mm in the endcaps. The scintillator layers are 4 mm thick. The light is collected by wavelength shifters. The scintillator in each layer is divided into tiles with a granularity matching the granularity of the ECAL trigger towers ($\Delta\eta \times \Delta\phi = 0.0875 \times 0.0875$).

The two hadronic forward calorimeters covering the pseudorapidity region $3 < |\eta| < 5$, are placed at $|z|$ =11.15 m from the interaction point outside the magnetic field. Because of the extremely harsh radiation environment near the beam, a different detection technique using a grid of quartz (radiation hard) fibers parallel to the beam embedded in a iron absorber is employed.

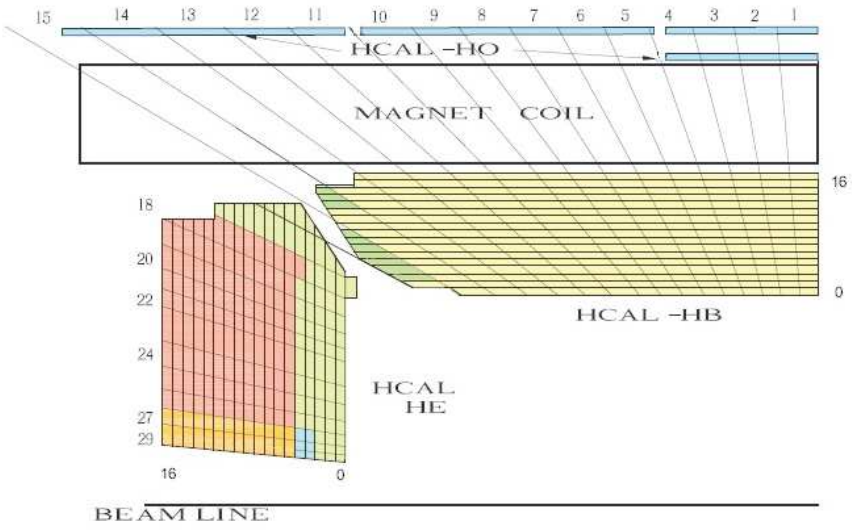

Figure 3.6. A longitudinal view of one quarter of the HCAL.

3.2.4 The Magnet

The CMS experiment is highlighted by its strong magnetic field provided by its superconducting coil. The magnet system is composed of three main parts, the superconducting solenoid, and the iron return yoke in the barrel and the endcap. The 3.8 T magnetic field allows the precise measurement of muon momenta up to $|\eta| \approx 2.4$. The barrel return yoke is a 12-sided cylindrical structure with a length of 11 m divided into 5 rings. The iron yoke has a weight of 7000 tons, more than half of the total weight of the CMS detector. The superconducting coil is placed in a vacuum tank and kept at the temperature of liquid helium. The weight of the vacuum tank is supported by the central barrel ring of the iron yoke.

The magnetic field layout is shown in figure 3.7.

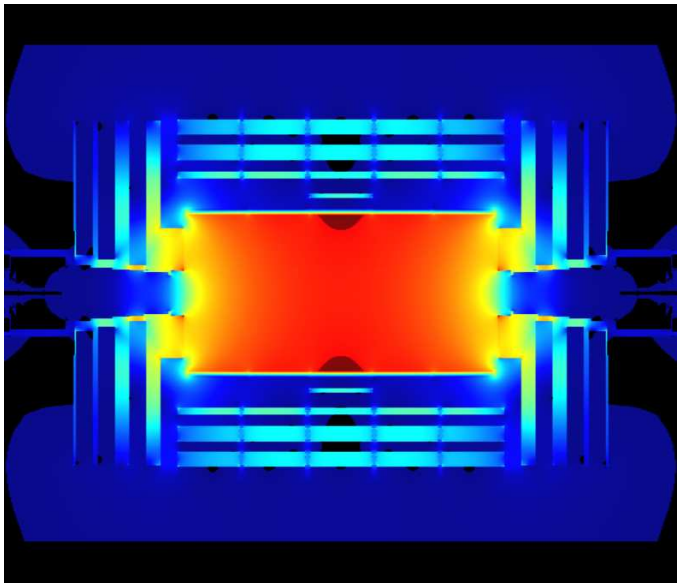

Figure 3.7. The magnetic field layout.

3.2.5 The Muon System

The muon system is designed to identify muons and measure their momenta accurately. The muon system is very important because muons provide clean signatures for many physics processes.

The muon system, as shown in figure 3.8, is the outermost part of the CMS detector and is embedded in the magnetic iron return yoke. The magnetic field inside the plates of the yoke bends the particles and allows the measurement of momenta.

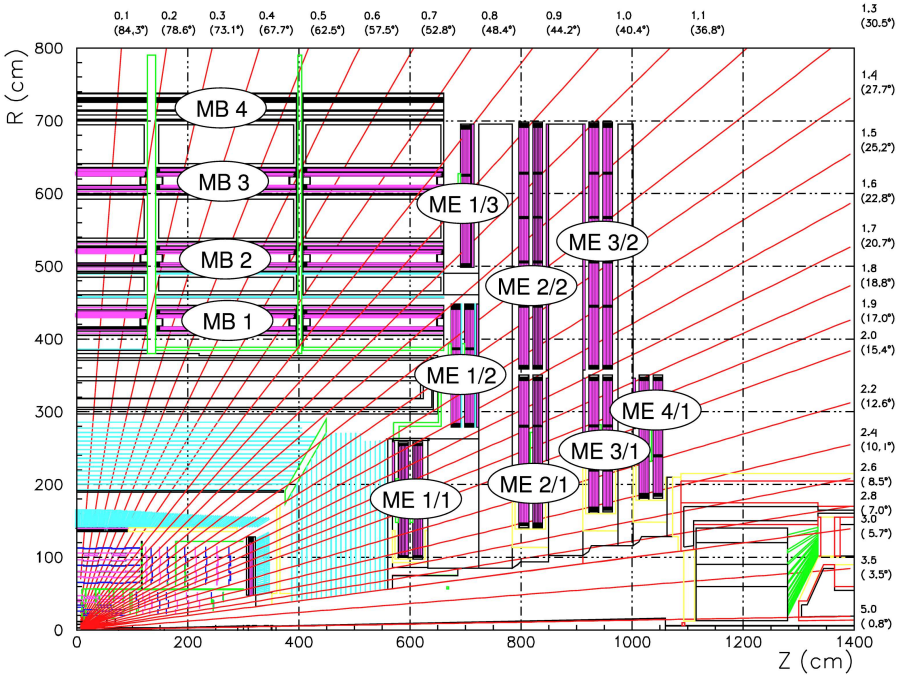

Figure 3.8. A quarter of the muon system.

The whole muon system is composed of three independent subsystems. In the barrel region ($|\eta| < 1.0$), Drift Tube (DT) detectors are installed, and Cathode Strip Chambers (CSC) are used in the endcap regions ($0.8 < |\eta| < 2.4$). Resistive Plate Chambers (RPC) are installed in the $|\eta| < 1.6$ region, covering both the barrel and the endcaps. RPCs have limited spatial resolution, but good time resolution thus can provide excellent bunch crossing identification.

The Drift Tube Chambers (DT)

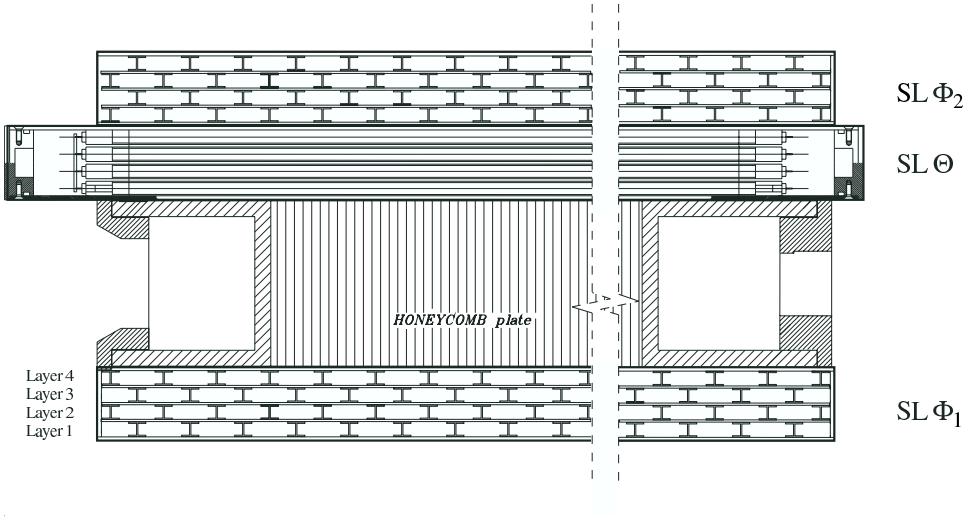

Figure 3.9. The layout of a DT chamber inside a barrel muon station.

The barrel muon system consists of five wheels along the z-axis, each one divided into 12 sectors and four stations called MB1, MB2, MB3, MB4 from the inside out. Each station consists of 12 chambers, except for MB4, which has 14 chambers.

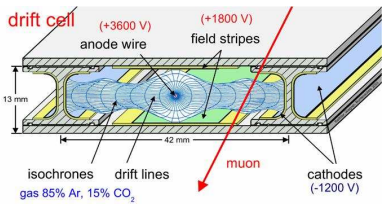

Figure 3.10. A drift cell.

Each DT chamber, as shown in figure 3.9 consists of two or three *superlayer*s, one or two superlayers measure the $r-\phi$ coordinate, and another orthogonal superlayer measures the $r-z$ coordinate. Each superlayer is composed of four layers of parallel cells. The most basic element is the drift tube cell, whose cross section is shown in figure 3.10. Each drift cell has a size of 42×13 mm^2. A layer of cells is constructed by two parallel aluminum planes and by "I" shaped aluminum beams that define the

boundary of the cells and serve as cathodes. The I-beams are insulated from the planes by a 0.5 mm thick plastic profile. The anode is a 50 μm stainless steel wire placed in the center of the cell. The distance of the track from the wire is measured by the drift time of electrons. To improve the distance-time linearity, additional field shaping is obtained with two positively-biased insulated strips, glued on the planes in correspondence to the wire. Typical voltages are +3600 V, +1800 V and -1200 V for the wires, the strips and the cathodes, respectively. The gas used is an 85%/15% mixture of Ar/CO_2, which provides good quenching properties and a saturated drift velocity of about 5.6 cm/μs. A single cell has an efficiency of about 99.8% and a resolution of 180 μm.

The Cathode Strip Chambers (CSC)

The endcap muon system is arranged in four stations at each end of the detector. They are numbered from ME1 to ME4 in order of their distances to the center. The innermost CSC stations are composed of three concentric rings (ME1/1, ME1/2, ME1/3), while the other stations are composed of two disks only (MEn/1 and MEn/2). Each ring consists of 18 or 36 trapezoidal chambers. All but the ME1/3 chambers overlap in ϕ and, therefore, form rings seamless in azimuth.

Each CSC chamber, as shown in figure 3.11, is composed of six layers. Each layer consists of an array of anode wires between two cathode planes. Strips are arranged in the radial direction and measure the ϕ coordinate. Wires are in the orthogonal direction and measure the r coordinate. The spatial resolution provided by each chamber from the strips is typically about 200 μm (100 μm for ME1/1). The angular resolution in ϕ is of the order of 10 mrad.

The Resistive Plate Chambers (RPC)

Resistive Plate Chambers are gaseous parallel-plate detectors that combine good spatial resolution with a time resolution comparable to that of scintillators. Fig-

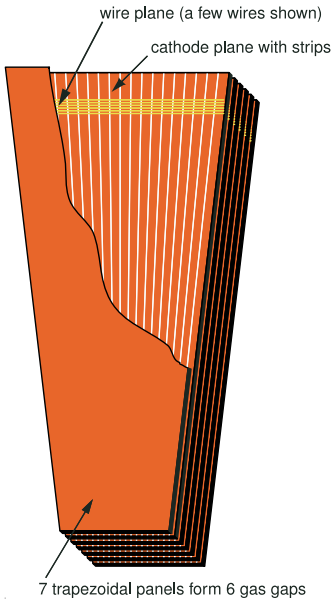

Figure 3.11. Schematic view of a CSC chamber.

ure 3.12 illustrates that each RPC is a double-gap bakelite chamber operating in avalanche mode. A robust signal amplification is introduced at the front-end level. The gaps have a 2 mm width. A total of six layers of RPCs is embedded in the barrel iron yoke, two located in each of the muon stations MB1 and MB2, and one in each of the stations MB3 and MB4. In each barrel chamber, the strips, which run along the beam direction, are segmented into two parts for stations MB1, MB3, and MB4 or three parts in some chambers in the MB2 station. In the forward region, three layers of RPCs cover the region up to $\eta = 1.6$.

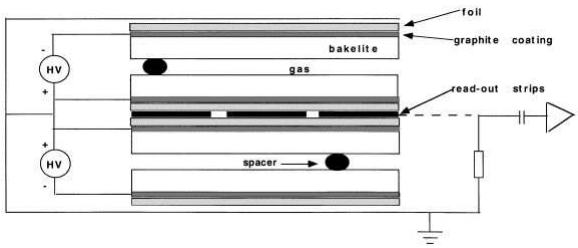

Figure 3.12. Schematic view of the RPC double-gap structure.

3.2.6 Trigger System

At the LHC design luminosity, the total event rate is expected to be about 10^9 Hz. However it is impossible to record all events. Therefore the trigger system must reduce the input rate down to $\mathcal{O}(100)$ Hz as well as maintain high efficiencies on the potentially interesting events by selecting events based on their physics signatures. The online selection process consists of two main steps: the level-1 (L1) trigger and the high-level trigger (HLT) [36, 37]. The concepts of the L1 trigger is described in the following part of this section, while the muon HLT is described in Chapter 5.

The Level-1 Trigger

The level-1 trigger needs to reduce the event rate down to 50 (100) kHz for the low (high) luminosity running and is implemented in dedicated programmable hardware. The L1 trigger has to make an accept-reject decision of an event within 3.2 μs to allow more time for more sophisticated algorithms in the HLT. Therefore the L1 trigger only accesses information from the calorimeters and muon systems.

The Level-1 trigger is organized into a calorimeter trigger and a muon trigger and the information is transferred to the Global Trigger (GT) which makes the final accept-reject decision.

The calorimeter trigger is based on trigger towers with a size of $\Delta\phi \times \Delta\eta = 0.087 \times 0.087$ in the barrel, or a larger region in the endcaps. The calorimeter trigger identifies four candidates for five types each, isolated electrons/photons, non-isolated electrons/photons, central jets, forward jets, and tau jets, from the calorimetric region information. The information of these candidates, as well as the measured missing E_T, is passed to the GT.

The muon trigger is implemented for DT, CSC, RPC muon detectors separately. The candidates from each muon detector are then merged, and the best four muon candidates are transferred to the GT. The GT makes the accept-reject decision exploiting both the characteristics of the single objects and from the combination.

In the DT subsystem, the DT trigger front-end is called the Bunch and Track Identifier (BTI). The BTI performs a straight segment fit within a superlayer using at least three hits out of the four layers of a superlayer. Segments in different $r-\phi$ superlayers of the same chamber are matched by the track correlator, and the angular resolutions are improved by the larger lever arm. The trigger server selects the two segments corresponding to the highest p_T among all segment pairs in a chamber and passes them to the drift tube track finder (DTTF). DTTF uses pre-computed, memory-resident Look-Up Tables (LUT) to link the segments between stations and to group matching segments. The muon candidate parameters are estimated with other LUTs and based on the ϕ direction of the segments in the two innermost stations. The DTTF matches the segments reconstructed in the four muon stations and builds a single muon track candidate with η, ϕ, p_T and a quality word. Finally, the candidates are sorted and the four L1 muon candidates with highest p_T are delivered to the global muon trigger (GMT).

In the CSC subsystem, the CSC local trigger reconstructs segments in each chamber independently using the strips and the wires of the six layers. Cathode strips, used to reconstruct the ϕ coordinate, are employed to measure the track p_T. The strips are digitized with half strip resolution first, using an interpolation based on a comparator that analyzes the charge in three adjacent strips. The hits in the six layers are then searched for patterns compatible with high-p_T tracks. The anode wires provide the information on η and precise bunch crossing assignment. A coincidence of two hits in different layers is needed to assign the bunch crossing, and reconstructing a segment requires four hits out of the six CSC planes. After this, 3-dimensional segments are reconstructed by the anode and cathode segments and sent to the CSC Track Finder, which links the segments of different stations to build a muon candidate. The CSC trigger electronics were not installed in the region $|\eta| > 2.1$ in chamber ME1/1, while the CSC system covers up to $\eta \approx 2.4$.

In the RPC subsystem, there is no local reconstruction performed in the trigger. A pattern comparator trigger (PACT) collects the hits and looks for time and space

correlation in the four RPC stations. Hits are matched with pre-defined patterns in LUTs to provide identification and the estimation of p_T, η, ϕ position and quality of the muon. The pattern identifies muons with at least three hits in four stations. In the barrel where there are six RPC layers, the search is done for low-p_T muons in the first four RPC layers in the first two stations and for high-p_T muons with one layer from each of the four stations. The four highest p_T candidates in barrel and endcaps are sent to the GMT separately.

The DT and CSC subsystem records four level-1 muon candidates at most, while the RPC records four barrel and four endcaps candidates at most. The candidates with information of η, ϕ, p_T and quality are passed to the GMT.

The GMT matches the muon candidates from different subsystems and combines their parameters by comparing the spatial η, ϕ coordinates in an optimized way. If two candidates are matched, the parameters of the track are chosen according to a programmable logic. The GMT accepts candidates triggered by two systems or having a certain quality. The selection criteria can be refined to balance high efficiency and background rejection. The GMT also looks for the MIP and quiet bits in the corresponding calorimeter regions. Finally, the GMT sends the four muons with highest p_T to the GT.

The High-Level Trigger

Upon receipt of a level-l trigger accept, the data are transferred to the front-end readout buffers. The HLT processes all events triggered by the level-1 trigger in a single computer processor farm and reduces the rate from 100 kHz down to 100 Hz. The CPU usage of the HLT is optimized by the concept of "regional reconstruction" and by rejecting events as early as possible. The basic strategy is to reconstruct each physics object in different subsystems which can be used to make decisions first and then involve information from more subsystems and make decisions at a higher level.

HLT paths are usually divided into several "virtual" levels, each level involves more information than its previous level, and reduces the event rate from its previous level.

The total CPU usage depends on the performance of the software components in all levels, but with different weights. If assuming the CPU takes T_i milli-second (ms) to process one event once activated for level-i, and the level-i has a rejection factor R_i ($R_i > 1$), which means one out of R_i events could be accepted on this level. Then the total CPU time for this HLT path is

$$T_{total} = \sum_{i=2}^{max}(T_i/(\prod_{j=2}^{i} R_j)) \text{ ms}, \tag{3.5}$$

noticing the HLT starts from level-2. The equation illustrates that the optimal strategy for the HLT is to have large rejection factors in the early phase and then more sophisticated algorithms taking longer times can be implemented at the higher level. The overall HLT strategy needs to be designed and tuned according to different luminosity scenarios. The muon HLT is introduced in more detail in Chapter 5.

4. MUON RECONSTRUCTION

4.1 Software Design, Requirements and Framework

The CMS simulation, reconstruction and analysis software, referred to as CMS SoftWare (CMSSW), is built around a framework, an Event Data Model (EDM), and a set of services needed by simulation, calibration and alignment, and event reconstruction. The CMSSW is designed using the object-oriented programming paradigm and is implemented in the C++ programming language [38].

The CMSSW event processing model consists of one executable and many plug-in modules which are managed by the CMSSW framework. All the code needed for event processing (calibration, reconstruction algorithms, etc.) is contained in *modules*. The same executable is used for both detector data and Monte Carlo sample processing. The CMSSW executable is configured by a configuration file in Python programming language [39], which specifies the input, output, processing sequences, and parameter settings for each module. In order to keep the CMSSW executable lightweight, only the required modules are dynamically loaded at the beginning of the job.

The CMS EDM is centered around the concept of an *event*. An *event* is a C++ object container for all raw and reconstructed data related to a particular collision. During processing, data are passed from one module to the next via the *event*, and can be accessed only through the *event*. All objects in the event can be individually or collectively stored in ROOT [40] files, and are thus directly browsable within ROOT.

The muon reconstruction software is designed to reconstruct muon tracks in the muon system and the silicon tracker. It is designed to be used for both online event selection and offline analysis. The software packages are integrated in CMSSW as different modules. Muon reconstruction is performed in three stages: local recon-

struction, standalone reconstruction, and global reconstruction, which are described in this chapter.

4.2 Tracking of Charged Particles

Before the description of the muon reconstruction, the basic concepts used for track reconstruction are introduced. The first step (*pattern recognition*) in track reconstruction is to identify a set of detector measurements which correspond to a single track. The higher the track multiplicity of an event, the more complicated it is to find the correct set of measurements. This process is performed using various pattern recognition algorithms. In a next step (*track fit*), all measurements corresponding to a track are fit in order to determine the best estimate of the track parameters. In the case of charged particles in a magnetic field, the parameters to describe the helix at each measurement surface can be presented as $(q/p, \tan\phi, \tan\theta, x, y)$, where q is the charge, p is the momentum, ϕ and θ identify the track direction, and x and y identify the local position on a given surface. The ultimate goal is to extract the track parameters, e.g., charge, p_T, η, ϕ, and quality parameters, e.g. χ^2, at the point of the closest approach (PCA) to the interaction point.

In CMS the algorithms for both steps, pattern recognition and track fit, are based on the Kalman filter technique [41]. The Kalman filter is a recursive method of estimating the states of evolving stochastic systems. The Kalman filter method is equivalent to the least squares method, but accommodates modeling the complicated magnetic field and materials between measurements. It also avoids calculations involving a large matrices. The computational cost is proportional to the number of surfaces crossed by a track.

For example, suppose a particle is traveling through ordered detector surfaces, numbered 1 to n, in a non-uniform magnetic field. Different detector components collect the signals generated by the particle. For example, the drift time in each drift cell is recorded in the DT, and the amount of charge is recorded in each CSC

sub-layer. All those signals are converted into spatial measurements used in the track fitting.

The track states on two adjacent surfaces of a particle trajectory have a certain relation determined by the modeling of the materials and magnetic field in between. The relationship can be presented by the *system equation*:

$$p_k = f_k(p_{k-1}) + P_k\sigma_k, \tag{4.1}$$

where f_k is a deterministic function presenting the track model between surfaces k and $k-1$. σ_k is a random disturbance which describes the effect of matter between the surfaces on the trajectory, mainly multiple scattering. It is called the *process noise* and holds the relation $\langle\sigma_k\rangle = 0$. Its covariance matrix, denoted as Q_k, is assumed to be known for all k. The matrix P_k is introduced because the noise may have different effects on different state parameters.

Usually the track states can not be measured directly. The observables, position measurements converted from other lower-level measurements, are functions of the track states superimposed by measurement errors. This relation is summarized in the *measurement equation*:

$$m_k = h_k(p_k) + \epsilon_k, \tag{4.2}$$

where h_k maps the track states (p_k) to the measurable variables (m_k) on surface k. ϵ_k is another random disturbance which describes the measurement errors. It has a mean $\langle\epsilon_k\rangle = 0$ and covariance matrix $V_k \equiv W_k^{-1}$.

If $p_{k|j}$ denotes the track state p_k based on measurements $\{m_1, ..., m_j\}$, then once $p_{k-1|k-1}$ is available, $p_{k|k}$ can be deduced in the following way. For the sake of convenience, all the above equations are assumed to be presented by linear matrix calculations without loss of generality.

First, the predicted track state on surface k without considering the noise is

$$p_{k|k-1} = f_k(p_{k-1|k-1}). \tag{4.3}$$

The covariance of the process noise is updated as:

$$C_{k|k-1} = f_k C_{k-1|k-1} f_k^T + P_k Q_k P_k^T \tag{4.4}$$

The covariance matrix is the sum of two terms, the first one is the propagation of the previous covariance, and the second one takes the process noise into account.

Updating with the current measurement m_k, p_k should minimize the following objective function

$$Lp_k = (m_k - h_k p_k)^T W_k (m_k - h_k p_k) + (p_{k|k-1} - p_k)^T C_{k|k-1}^{-1} (p_{k|k-1} - p_k), \qquad (4.5)$$

which presents the overall effect of process noise and measurement errors.

After some algebra, one can derive

$$p_{k|k} = p_{k|k-1} + K_k(m_k - h_k p_{k|k-1}) \qquad (4.6)$$

$$C_{k|k} = (C_{k|k-1}^{-1} + h_k^T W_k h_k)^{-1} = (I - K_k h_k) C_{k|k-1} \qquad (4.7)$$

where $K_k = C_{k|k-1} h_k^T (V_k + h_k C_{k|k-1} h_k^T)^{-1}$.

The $p_{k|k}$ is a combination of the predicted track state and the correction by including the current measurement. It has all the optimum properties of a linear least squares estimator.

The Kalman filter requires a starting track state $p_{1|1}$, defined as a *trajectory seed*, to begin the recursive process. However, in general the first measurement m_1 is not sufficient to determine the initial state completely. Usually the seeds are estimated by imposing some other assumptions or including a few measurements with large errors.

4.3 Local Reconstruction

Local reconstruction is performed using several individual packages of CMSSW dedicated to different subsystems. Local reconstruction generates reconstructed hits and segments with a common interface after local pattern recognition performed within a chamber.

In the DT system , the position of 1-dimensional hits in drift cells are extracted from Time to Digital Converter (TDC) measurements. First, an average value for the drift velocity is used to fit a 2-dimensional segment in a super-layer. The segments

reconstructed in the two super-layers in each chamber are then fit together, and produce a 4-dimensional (3-dimensional position and 3-dimensional direction) segment. The direction resolution of the resulting segments in the r-ϕ plane is about 0.9 mrad. In the r-z (non-bending) plane, it is about 9 to 13 mrad.

In the CSC system, each CSC plane measures a point in two dimensions. One coordinate is measured by the wires, while the other coordinate is measured by the strips. The charge deposits of neighboring strips are collected to obtain a precise position measurement. The 2-dimensional hits in a chamber are used to fit a 4-dimensional straight line segment with direction.

In the RPC system , the RPC hits are obtained by clustering the strips and calculating the center of gravity of the area covered by the strips in the cluster (i.e. the width of the strips times their full length).

4.4 Standalone Muon Reconstruction

Standalone muon reconstruction reconstructs trajectories from the segments and hits built in different muon subsystems. Both tracking detectors (DT and CSC) and RPCs participate in the reconstruction. Despite the coarser spatial resolution, the RPCs complement the tracking chambers, especially in the barrel-endcap overlap region, where the geometrical coverage is problematic.

The reconstruction starts with the locally reconstructed track segments from the muon chambers. The state vectors (track position, momentum, and errors) associated with the segments, usually in the innermost chambers, are used to seed the muon trajectories. A specified *navigation* defines the compatible layers according to the position and direction of each trajectory state, where compatible layers are the possible layers that the track will pass through. The *trajectory builder* iterates over all compatible layers using the Kalman filter technique. There are two steps in the trajectory building process, a forward fit and a backward refit. In the forward step, all track segments are used as measurements, while the individual reconstructed hits

are used in the backward step in order to get better curvature information. The track parameters and the corresponding errors are updated at each step. Finally, the state at the innermost muon station is extrapolated to the interaction point in order to define the track parameters at the PCA, which are stored into the event in a compact way for later processes.

4.4.1 Seed Generation

The first step of standalone muon reconstruction is to generate trajectory seeds. A trajectory seed contains a state vector associated with one or more DT or CSC hits or segments. Trajectory seeds are the input to the following trajectory building step, and are usually the starting point to build a trajectory. In the standard standalone muon seed generation algorithm, the state vector of a seed is estimated by a parameterization according to the relative positions of selected segments and the interaction point.

Seeds in the DT and CSC system are constructed by searching for certain patterns of DT and CSC segments. Once a pattern of segments has been found (it may also consist of just one segment), the p_T of the seed candidate is estimated using parameterizations of the form:

$$p_T = A - \frac{B}{\Delta\phi} \tag{4.8}$$

For DT seed candidates with segments in MB1 or MB2, $\Delta\phi$ is the bending angle of the segment with respect to the direction pointing to the vertex. This part of the algorithm assumes the muon has been produced at the interaction point. If segments in both MB1 and MB2 exist, the weighted mean of the estimated transverse momenta is taken. If the seed candidate only has segments in MB3 and MB4, the difference in bending angle between the segments in the two stations is used to calculate p_T.

In the CSC system, seed candidates are built from a pair of segments in either the first and second stations or the first and third stations. $\Delta\phi$ is the difference in

ϕ position between the two segments. Otherwise, the direction of the highest quality segment is used.

4.4.2 Navigation in the Muon Detector

The track fitting method does not require the full set of reconstructed hits to be available before the fit. Instead, at each step during the fit, the track parameters are used to identify the detectors that most probably contain the next hit to be included in the trajectory, such that the pattern recognition and fit are performed simultaneously. The algorithmic problem of finding the next detector crossed by one trajectory, given its parameters at a given point, is called *navigation*.

The tracking detectors in CMS can be abstracted as a series of layers, cylinders in the barrel region and disks in the endcap region. A muon trajectory starting from the interaction point crosses the layers in a well-defined sequence, i.e. always in an inside-out sequence and within a small η window.

The problem of navigation is therefore solved by organizing the detectors in a hierarchical structure. The first level of the hierarchy is a full layer of detectors. In the barrel muon system it consists of a cylinder, corresponding to either one DT or one RPC station. In the endcaps, layers are flat vertical disks corresponding to either one CSC or one RPC station, except for the first station (ME1), which is split into two layers at different positions in z. Layers are sorted by their distance from the detector center. This is the order in which they are traversed by a trajectory coming from the interaction point, so that, at each fitting step, reconstructed hits are looked for in the next layer in the list (provided that the track direction with its error is within the layer's η boundaries).

According to the geometry described in Chapter 3, each barrel muon layer consists of rods, and each rod consists of five chambers. There are 12 rods in each layer, except for MB4, where there are 14. Chambers in a rod lie on the same plane, are contiguous in z, and are all at the same r and ϕ coordinates. Rods in a layer are quasi-periodic in

ϕ and, in some cases, slightly overlap in this coordinate. Endcap layers are organized in rings of chambers. All chambers in one ring are located at the same r and are periodic in ϕ. In all endcap layers, with the exception of ME1/3, the chambers in a ring are staggered in z. In this case, the ring's nominal surface is a flat disk placed between the two planes of chambers.

When the layer is queried for the measurements compatible with a track, a first extrapolation is made to the layer's surface. Then, selected chambers are individually queried for compatibility with the track, and compatible measurements are determined on those chambers.

4.4.3 Trajectory Building

There are two steps in trajectory building, a forward fit and backward refit. Both are based on the same Kalman filter method described in section 4.2.

The forward fit starts from the state vector provided by a trajectory seed and located at the innermost compatible muon detector layer, and grows the trajectory inside-out. At each step the track parameters are propagated from one layer of muon detectors to the next. The propagation includes magnetic field, material effects, and is also optimized for speed. The trajectory is extrapolated in sequential steps using a helix parameterization. The required precision is obtained by using smaller steps in regions with larger magnetic field inhomogeneities. Multiple scattering and energy losses in each step are estimated from fast parameterizations, avoiding time-consuming accesses to the detailed material and geometry descriptions. The resulting propagated state contains these effects in its parameters and errors. A configurable χ^2 cut is used in order to reject bad segments or hits, mostly due to showering, delta rays, and pair production. In case no matching hits or segments are found (e.g. due to detector inefficiencies, geometrical cracks, or hard showering), the search is continued in the next station. The state is propagated from one station to the next, taking into account the muon energy loss in the material, the effect of multiple

scattering, and the nonuniform magnetic field in the muon system. The backward refit starts from the last and most precise state vector in the forward fit and grows the trajectory outside-in. After the fit and refit, a precise state vector is built at the surface with the innermost hits. Finally, the track parameters at the PCA are obtained by extrapolation under the assumption that the muon originated from the interaction region (defined by the beam spot size, $\sigma_{xy} = 15$ μm and $\sigma_z = 5.3$ cm as default). The beam spot can be determined from minimum bias events at the very start of a run.

4.5 Global Muon Reconstruction

Global muon reconstruction starts from the track built by the standalone muon reconstruction and extends the track to include hits in the silicon tracker.

For offline global muon reconstruction, there are already tracks built by track reconstruction in the tracker system. For each standalone muon track, a collection of tracker tracks are selected first in the *track matching* step. Then those tracker tracks are combined with the standalone muon track, and the combined track with best global fit is the resultant global muon.

4.5.1 Track Matching

The first step in global muon reconstruction is to identify which silicon tracker track to combine with the standalone muon track. The large multiplicity of tracks in the central tracker necessitates the selection of a subset of tracker tracks that roughly correspond in momentum and position to the standalone muon track. The method of track matching proceeds in two steps. The first step of the track matching process is to define a region of interest that is rectangular in η-ϕ space and to select a subset of tracker tracks that are in this tracking region of interest. The second step is to iterate over the subset of tracker tracks, applying more stringent spatial and

momentum matching criteria to choose the best tracker track to combine with the standalone muon.

A rectangular η-ϕ tracking region is used to choose the initial set of tracker tracks that roughly correspond to the standalone muon track. The definition of the region of interest has a strong impact on the reconstruction efficiency, fake rate, and CPU time. A silicon track is compatible with a rectangular η-ϕ tracking region if its η-ϕ parameters are within the region and its p_T above a minimum threshold so that it can reach the muon system.

The matching of two disjoint tracks is performed by comparing the five parameters describing the trajectory. This is best done by propagating the tracks onto a common reference point or surface; the choice of a surface constraint provides one more degree of freedom on the fit as opposed to a point constraint, and it is therefore better at incorporating random scattering effects.

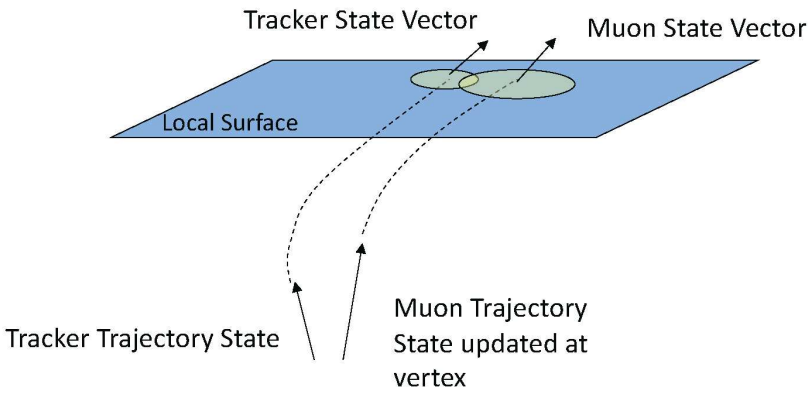

Figure 4.1. Illustration of matching the error matrix of two trajectory states on a common surface.

The two competing objectives that determine the choice of the common surface for track matching are choosing the plane that (1) minimizes the covariant error matrix of the propagated track parameters and (2) reduces the number of matches per standalone muon. It is possible to propagate the tracker track and standalone muon track to any common plane. Some of the natural choices for a common sur-

face are the tracker system outer boundary, the muon system inner boundary, the detector surface of the outermost tracker track hit, and the detector surface of the innermost muon track hit. After examining the discriminating power using different surfaces, the innermost muon track hit surface is chosen because tracker tracks are reconstructed more precisely and can maintain reasonable precision even after long distance propagation.

Once the tracks are propagated to the common surface, the track parameters (p_T, η, ϕ, local χ^2 compatibility, and local position distance) between the tracker track candidates and the standalone muon track are compared, and compatible matches are determined. If no match is found based on certain cuts on the distributions, the best match is chosen based on a loose cut on the track directions at the interaction point.

4.5.2 Navigation in the Muon and Tracker Detector

Similar to the navigation in the muon system, a separate navigation system was designed to treat the muon layers and tracker layers in a consistent way, such that muon layers and tracker layers are connected with each other.

A full layer of detectors consists of a cylinder corresponding to one DT, RPC, TOB, TIB, or pixel layer in the barrel, and a disk corresponding to one CSC, RPC, TEC, TID, or pixel layer in the endcaps.

4.5.3 Trajectory Refitting

In the global refitting step, all hits from the standalone muon and its matched tracker tracks are sorted. Starting from the trajectory states derived from the separate tracks, another Kalman fitting process is applied hit by hit, inside-out and outside-in. This step is relatively fast since all hits are well-confined and no additional pattern recognition needs to be performed. After building the trajectories, all trajectories in each event are sent to the *trajectory cleaner*. The cleaner resolves ambiguities

between multiple trajectories that may result from a single real track on the basis of their direction, momentum, and hit information.

In the final step, all reconstructed tracks are stored in the event in a compact format. A muon object contains a standalone muon track, a tracker track, and a combined track.

Additional refitting options are available for high-energy muons in the final refitting. Muons with energies of several hundred GeV and more have a high probability of producing electromagnetic showers in the iron of the CMS magnet return yoke. These large energy losses can significantly degrade the performance of muon reconstruction. Including these measurements in the track fit can lead to incorrect reconstructed momentum values.

There are several approaches to optimize the reconstruction quality for high energy muons. In addition to the global fit, several refits of the global muon trajectory are performed with different sets of hits. One fit, referred to as Tracker Plus First Muon Station (TPFMS), only uses the hits from the tracker and the first muon station with hits. Another fit selects hits by applying tight cuts for muon hit compatibility with the trajectory. These two refits, optimized for showering muons, are considered along with the standard global muon fit and the fit using only the hits from the inner tracker, and the global goodness-of-fit of each of the four trajectories is evaluated.

To demonstrate the effect for physics of the high energy refits, the dimuon resolution as a function of mass for five resonances: J/Ψ, Z, and a 1, 2, and 3 TeV Sequential Standard Model Z' is shown in figure 4.2. The same track selection conditions are applied and results from four different detector alignment scenarios are presented.

4.6 Cosmic Muon Reconstruction

Cosmic muons are the most abundant particles originating from cosmic rays at sea level [42]. Beam-halo muons are machine-induced particles that travel along the

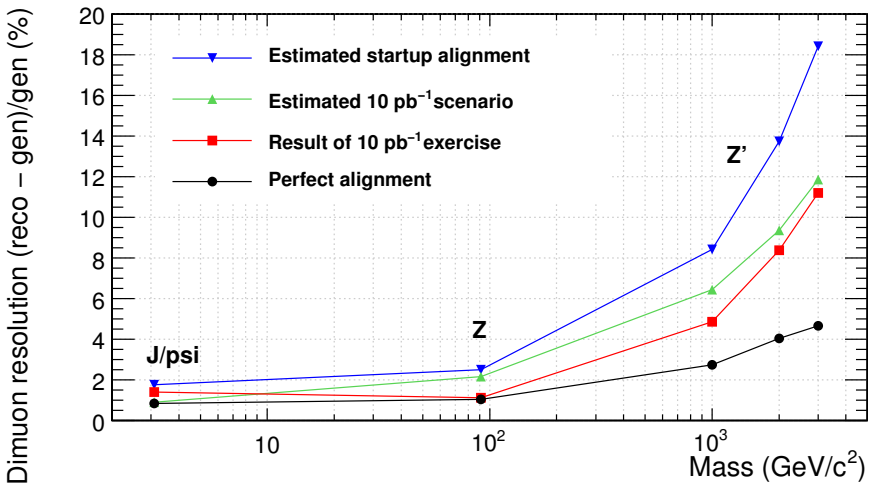

Figure 4.2. Dimuon mass resolution for four alignment scenarios.

beam line. Although in physics analyzes these types of muons are generally considered as sources of background, they can be used for detector alignment, calibration, performance validation and even physics analysis. The efficient reconstruction of cosmic and beam-halo muons is especially important for the commissioning phase of the detector [43]. However, the detection and reconstruction of cosmic and beam-halo muons are different from that of muons from p-p collisions.

Since the standard muon reconstruction software has been optimized to identify and reconstruct muons originating from p-p collisions, a different optimization must be carried out to effectively reconstruct muons coming from outside the detector. A dedicated cosmic muon reconstruction software was developed and the performance was tested with real data taken during the several cosmic runs including Cosmic Runs At Four Tesla (CRAFT). Unlike muons from collisions, which are moving radially outward, cosmic muons arrive at the detector from random directions and at random times. They can traverse either both hemispheres or only a small part of the detector depending on their energy and direction. Figure 4.3 illustrates the different topologies of muons coming from outside and from p-p collisions. In some cases, as indicated in

figure 4.3(b) and (c), the standard muon reconstruction algorithm can reconstruct a cosmic muon, but the muon will be recognized as 2 separate tracks.

The standard reconstruction algorithms are designed with the assumption that muons are coming from the interaction point and the direction of the energy flow of trajectories is always out-going from the center of the detector. Pattern recognition based on this assumption is not suitable for the reconstruction of muons coming from outside the detector, except for some special cases when the direction of cosmic muons is pointing to the interaction point. To correctly and efficiently reconstruct cosmic muons and beam-halo muons, the cosmic muon reconstruction algorithm assumes that muons are coming from outside, and is optimized by utilizing properties of cosmic muons and beam-halo muons as discussed below.

The cosmic muon reconstruction software is available to the CMS community as a part of the official CMS software releases since 2006. Although the initial motivation of the design was to reconstruct cosmic muons, the reconstruction algorithm can also be applied to beam-halo muons. It was employed successfully to reconstruct cosmic muons traversing the CMS detector during cosmic runs and beam commissioning during the first LHC start-up.

The assumption that muons come from the interaction point is implemented in all steps in the standard sequence of reconstruction chain and has to be turned off when dealing with cosmic or beam-halo muons. The new cosmic muon reconstruction software follows the same reconstruction structure and uses as many common tools as possible, specializing and optimizing each individual component to adapt to the properties of cosmic and beam-halo muons.

Here the strategies of standalone and global reconstruction for cosmic and beam-halo muons are discussed.

4.6.1 Readout for Cosmic and Beam-Halo Muons

The synchronization among sectors for cosmic and beam-halo muons is different from that for muons from p-p collisions because cosmic and beam-halo muons move in different directions and arrive randomly in time. The typical time interval for a cosmic muon traversing the entire CMS detector from top to bottom is around 50 ns (2 Bunch Crossing (BX)s). Beam-halo muons arrive at the interaction point at the same time as the beam (up to a few nanoseconds). However, they pass through one end of the detector before the other. The typical time interval for a beam-halo muon to traverse the CMS detector from one endcap to the other is less than 70 ns, thus within 3 BXs. A piece of the track in one hemisphere can be used to trigger the event, while the other piece is usually suppressed by the trigger, but can still be read out in the same event. For the DT system, the measured drift time for each recorded hit in the drift tube cells is buffered within a programmable time window of the order of 20–30 BXs. For the CSC system, the signals of deposited charges is buffered in switched capacitor arrays in 8 time bins, where the width of each time bin is 50 ns. When a trigger fires, the counts of the deposited charges in the 8 time bins are stored as a vector of integers [34]. Therefore, with a well-defined cosmic or beam-halo trigger strategy and local calibration, DT and CSC systems are able to take a "snap shot" of the full trajectory of a cosmic or beam-halo muon that includes 2 track pieces on opposite hemispheres in an event.

4.6.2 Standalone Cosmic Muon Reconstruction

Seed Generation

As discussed in Section 4.4.1, the first step of standalone muon reconstruction is to generate trajectory seeds. Each muon trajectory seed is built from either one DT or CSC segment, or a DT segment pair. Segments located higher (holding a larger y value in the CMS reference coordinates [34]) in the DT system are preferred to lower

ones for consideration of the place where cosmic muon trajectories start, while the segments located in the outermost endcap layers are preferred to inner ones for beam-halo muons. The direction of the trajectory state vector is determined by the direction of the segment, which excludes the parameterization involving the interaction point. The momentum direction for all cosmic muons is set to be downward because most cosmic muons travel this way. However, only segments with measurements in all space coordinates can ensure a qualified cosmic trajectory seed. While segments without information in one coordinate are used in standard seed generation, in cosmic seed generation they are used only when there is no better segment available in the event.

Navigation for Cosmic and Beam-Halo Muons in the Muon Detector

The next step is to identify the allowed path of a muon trajectory starting from the trajectory seed.

The navigation used for cosmic muons is fundamentally different from the navigation used for the reconstruction of muons from collisions. The difference is illustrated by the examples in figure 4.4. Taking a trajectory state as indicated by the arrow with the direction pointing to bottom-right, for example, the standard method checks the η of the position of the trajectory state, and chooses all muon layers that cover or intersect the η window around the state. The order of compatible layers is determined by their relative distances with respect to the interaction point. The new *direct muon navigation* algorithm used in cosmic muon reconstruction does a straight-line extrapolation along the direction of the trajectory state from its position, and chooses all muon layers that intersect or are close to it. The order of the compatible layers is determined by their relative positions with respect to the trajectory state's position and direction. In figure 4.4, the layers filled with green color (or dark shadow) are determined as compatible layers with the given trajectory state by two different methods. For beam-halo muons, the direct navigation method picks up all layers in both endcaps and skips all barrel layers, as indicated in figure 4.4(c). The direct

muon navigation method can also be used for muons from *p*-*p* collisions with similar performance to the standard one.

Trajectory Building

As described before, standalone cosmic muon reconstruction builds trajectories starting from trajectory seeds, by including hits and segments built in different muon subsystems. The method for trajectory building is essentially the same in both the cosmic and the *p*-*p* sequences. There are several aspects that need to be taken care of for cosmic muon reconstruction. First, the hits in each track segment in the muon system are put into the trajectory in an order called the *navigation direction*. The navigation direction is used locally within each chamber and is defined as outside-in or inside-out according to the distance with respect to the interaction point (radius in the barrel region and absolute z component value in the endcap region). The navigation direction never changes during a fit or refit for a muon from *p*-*p* collisions. For cosmic muons, the navigation direction may change when the location changes, e.g. when a muon enters from endcap to barrel, as illustrated in figure 4.3(f). Assuming the cosmic muon is coming from above and the fit is performed along the momentum direction, the navigation direction is outside-in in the endcap region, but becomes inside-out in the barrel region. The navigation direction is carefully checked in cosmic muon trajectory building when the location changes. For beam-halo muons, the navigation direction is set as outside-in in one endcap and inside-out in the other.

A special algorithm is needed to build those trajectories that are referred to as *traversing muons* in the following text (see figure 4.3(b)), or as *1-leg standalone muons* (as opposed to *2-leg standalone muons*, which are reconstructed in one side of the detector only). Traversing cosmic muons come from outside, traverse the detector, and leave from the other side, passing through some cylinders in the barrel region twice. When grouping all compatible layers together, those cylinders appear in the list twice. Thus the next layer of the innermost cylinder can be the cylinder itself

in a middle refit step. In this case, when the trajectory state of the current layer is propagated to the next layer, the predicted state is on the same surface and is the same as the original state, and the trajectory building cannot be continued to the other hemisphere. Therefore, the compatible layers in the two hemispheres should be determined separately. After the fit in the first hemisphere is finished, if the trajectory ends up in an inner cylinder, the mechanism of building traversing muons is turned on. The last trajectory state of the trajectory in the first hemisphere is propagated inward to construct a trajectory state on a virtual plane, which is perpendicular to the direction of the last trajectory state and passing through the origin. The trajectory state on the virtual plane is used as the seed for the rest of the trajectory building process. Compatible layers of this trajectory state are iterated to update the trajectory with measurements. The trajectory building is then continued in the other hemisphere with the opposite navigation direction. To avoid the trajectory state propagating back to the first hemisphere, the propagation direction has to be explicitly specified as *along momentum* or *opposite to momentum* according to the location of the existing half of the trajectory. While propagating between layers within the same hemisphere, the propagation direction can be automatically decided.

As the final step of trajectory building, the trajectories are smoothed to obtain better track parameters. When smoothing a trajectory, the propagation from the last trajectory state in one hemisphere to a hit located in another hemisphere is treated in a special way, because the propagation direction has to be determined as along momentum or opposite to momentum by the relative position of the destination plane and the direction of the starting state. When the destination plane is far from or almost parallel to the direction of the starting trajectory state, it is likely that the propagation direction is estimated incorrectly and thus the propagation to the destination plane fails. In this case, several virtual planes are built between the starting state and the next hit, and the trajectory state is propagated one by one, as illustrated in figure 4.5.

4.6.3 Global Cosmic Muon Reconstruction

Global cosmic muon reconstruction starts from tracks built by the standalone cosmic muon reconstruction and extends the track to include hits from the silicon tracker, if they exist.

The tracks in the tracker system are built by other track reconstruction algorithms dedicated to reconstruct cosmic muons within the tracker system [44]. For each standalone muon track, only the tracks that match its momentum direction within an η-ϕ region around the cosmic muon track are selected. Compared with standard global muon reconstruction, the matching step is looser.

In the next step, all hits in the standalone muon and its matched tracker track are sorted. Each cosmic muon trajectory is divided into two parts in two opposite hemispheres of the muon system. The part containing the injection point with higher latitude should be the place where the cosmic muon entered the detector, and hits in this hemisphere are sorted as outside-in, while hits in the other part are sorted as inside-out. The tracker hits are inserted between the two parts of muon hits with an order sorted by their vertical positions. After the order of hits is decided and a starting trajectory state is chosen from the muon track, another Kalman fitting process is applied to iterate over the hits along and opposite to momentum. In this case, the number of hits in a single muon track can be more than 100, which allows a very precise measurement.

4.7 Performance

The performance of the muon reconstruction algorithms was evaluated using the full detector simulation as well as the cosmic ray data collected before the LHC start-up in 2008.

4.7.1 Performance of Reconstruction Sequences for p-p Collisions

The efficiencies and resolutions are measured using different simulated samples. To match the simulated muon with the reconstructed track, a cone criterion has been used that requires $\Delta R = \sqrt{(\Delta\phi)^2 + (\Delta\eta)^2}$ less than 0.1. No charge dependent differences were observed during the study, and no distinction is made between different charges.

Efficiencies

For the standalone and global reconstruction the efficiencies can be factorized as follows:

$$\begin{aligned} \varepsilon_{seed} &= \varepsilon_{seed-algo} \times \varepsilon_{\mu-acceptance}, \\ \varepsilon_{sa} &= \varepsilon_{seed} \times \varepsilon_{sa-algo}, \\ \varepsilon_{glb} &= \varepsilon_{sa} \times \varepsilon_{tk} \times \varepsilon_{matching}, \end{aligned}$$

where ε_{seed} is the efficiency for finding a seed and $\varepsilon_{\mu-acceptance}$ accounts for the muon system geometry acceptance. ε_{sa} is the total efficiency of reconstruction normalized to the number of simulated tracks. $\varepsilon_{sa-algo}$ is the efficiency with respect to the previous seeding step. ε_{glb} and $\varepsilon_{glb-algo}$ are defined similarly.

Standalone Muon Reconstruction In figure 4.6 the total efficiencies for the muon seeding step (ε_{seed}) and the algorithmic efficiency of the pattern recognition in the muon system ($\varepsilon_{sa-algo} = \varepsilon_{sa,seed} = \varepsilon_{sa}/\varepsilon_{seed}$) are shown. The loss in efficiency at $|\eta| \sim 0.3$ is due to a geometrical effect, since in that region there is a discontinuity between the central wheel and its neighbors. The dips in the $0.8 < |\eta| < 1.2$ region are due to the complicated geometry of the barrel-endcap overlap region. These figures show that the standalone muon reconstruction efficiency is determined by the seed, as $\varepsilon_{sa,seed}$ is close to 100%. The inefficiency is due to incorrectly estimated parameters at the seeding stage, which may lead to a failure in the pattern recognition.

The overall integrated efficiency for momenta above 10 GeV is above 97%. For low momenta the efficiency decreases because it is less likely for low-p_T muons to penetrate all four muon stations.

In order to decouple the algorithmic efficiency from this effect, simulated tracks that leave more than a given number of simulated hits in the muon detector are selected. The reconstruction efficiency to find a seed or a track is then determined as a function of the minimum required number of *true* hits in the detector. In figure 4.7 this efficiency is shown both for the seed, $\varepsilon_{seed}(n^{min}_{simhits})$, and for the algorithmic standalone muon reconstruction, $\varepsilon_{sa,seed}(n^{min}_{simhits})$. The curves in figure 4.7 are integral and the n^{th} point means that only simulated tracks with *n or more* associated simulated hits in the muon spectrometer are selected and used to calculate the efficiency.

The curves show the expected trend of a monotonic increase reaching a plateau. Two regions can be identified for muons with p_T less than a TeV, one is from 0 to about 9 hits and the other from 9 to the plateau. The first interval is defined by the minimum number of reconstructed hits required to have a segment in either a CSC or DT station in addition to an RPC measurement. Requiring at least 9 simulated hits is equivalent to having at least two segments in the muon system. The curves asymptotically reach a maximum, which is the efficiency for the reconstruction of a high quality muon. For the TeV-muons the pattern recognition efficiency (figure 4.7) decreases above 24 hits. This is due to the high probability that a TeV-muon generates secondary particles or an electromagnetic shower in the spectrometer. Many segments can be generated and the probability of building fake segments (or segments with incorrect parameters) increases considerably, reducing the algorithmic efficiency of the pattern recognition. Therefore, for TeV-muons the requirement on the *minimum* number of simulated hits is no longer a useful parameter for establishing the quality of the track, and $\varepsilon(n_{simhits})$ should be evaluated instead. The conclusion of the observation is that the loss in efficiency in the muon track reconstruction is entirely due to the acceptance.

Global Muon Reconstruction Global muon reconstruction requires the matching of reconstructed tracks in both the muon system and the tracker and the overall efficiency is a product of the standalone, the tracker track, and the matching efficiencies. The results are shown in the following figures: figure 4.8 shows the global efficiency ε_{glb} and $\varepsilon_{glb,sa} = \varepsilon_{glb}/\varepsilon_{sta}$.

The efficiency plots shown in figure 4.8 exhibit a number of lower efficiency structures which correspond to discontinuities in the geometry of the detector as mentioned before. These are as follows:

- $\eta \simeq 0$: junction surface between the two tracker barrels;
- $|\eta| \simeq 0.3$: inter-space between the DT central wheel and its neighbors;
- $0.8 < |\eta| < 1.2$: problematic DT and CSC overlap region;
- $|\eta| \simeq 1.8$: problematic region for tracker track reconstruction (transition from TID to TID/TEC subsystem);
- $\phi \simeq 1.2$: barrel inactive region (chimney), because of instrumentation services;
- periodic structure in ϕ: loss in efficiency in the standalone muon reconstruction due to muons which escape in the space between two adjacent sectors or chambers in CSCs (although all chambers overlap in ϕ, except those in ME1/3).

$\varepsilon_{glb,sta}$, as shown in 4.8 (left), shows that the standalone muon efficiency dominates the final muon reconstruction efficiency.

The muon reconstruction efficiency increases up to a plateau value which is approximately constant from $p_T = 8$ GeV to 1 TeV (starting from $p_T = 5$ GeV more than 50% of muons are reconstructed). At TeV momenta the muon reconstruction efficiency decreases slowly due to the effects of bremsstrahlung on finding correct seeds.

Data-Driven Efficiency Measurements For the early CMS data-sets, reliance on efficiency predications from Monte Carlo (MC) simulation will produce large systematic errors due to imperfections in modeling both the data and the detector response. Ideally therefore, one would like to measure particle efficiencies from the data itself, with no reference to simulation. One well established data-driven approach to measuring particle efficiencies is the so called tag-and-probe method [45].

The tag-and-probe method utilizes a known mass resonance (e.g. J/Ψ, Υ, Z) to select particles of the desired type, and probe the efficiency of a particular selection criterion on those particles. In general the "tag" is an object that passes a set of very tight selection criteria designed to isolate the required particle type. In the case of muons, the tag will in general be a global muon with some additional p_T cuts imposed such that the fake-rate is very small. A generic set of the desired particle type (i.e. with potentially very loose selection criteria) known as "probes" is selected by pairing these objects with tags such that the invariant mass of the combination is consistent with the mass of the resonance. Combinatoric backgrounds may be eliminated through any of a variety of background subtraction methods such as fitting, or sideband subtraction. The definition of the probe object depends on the specifics of the selection criterion being examined. The efficiency itself is measured by counting the number of "probe" particles that pass the desired selection criteria:

$$\varepsilon = \frac{P_{\text{pass}}}{P_{\text{all}}}, \tag{4.9}$$

where P_{pass} is the number of probes passing the selection criteria and P_{all} is the total number of probes counted using the resonance. It is worthwhile to note that in some cases a probe object will also pass the tag selection criteria. In this case it will appear in both the tag and probe lists, and produce a double pairing in the same event. The efficiency formula as written above accounts for these double pairings.

For offline muons the total efficiency measurement can be broken down (factorized) into three sequential measurements. The three steps are muon tracking efficiency,

standalone muon reconstruction efficiency, and matching efficiency. The global efficiency is thus given by the product

$$\varepsilon_{global} = \varepsilon_{standalone} \times \varepsilon_{tracker} \times \varepsilon_{matching} \tag{4.10}$$

Figure 4.9 shows an example of the fit output at the Z resonance. The example fit is shown for a particular p_T and η range in the measurement of muon standalone reconstruction efficiency. For the standalone muon reconstruction efficiency, the set of all probes is the collection of all tracks from the inner (silicon) trackers. A passing probe is then a probe that is also matched (geometrically) to a standalone muon track.

Momentum Resolution

To measure the momentum resolution of reconstructed muons, q/p_T is used as the variable of interest because q/p_T is, locally, directly proportional to the curvature in the bending plane. Moreover q/p_T is more suitable than p_T because it has a Gaussian distribution around the true value. The resolution of this parameter is defined as the Gaussian width of:

$$\sigma(\frac{q}{p_T}) = \frac{\delta(\frac{q}{p_T})}{\frac{q}{p_T}} = \frac{q^{\mathrm{rec}}/p_{\mathrm{T}}^{\mathrm{rec}} - q^{\mathrm{sim}}/p_{\mathrm{T}}^{\mathrm{sim}}}{q^{\mathrm{sim}}/p_{\mathrm{T}}^{\mathrm{sim}}}, \tag{4.11}$$

where q is the charge and $p_{\mathrm{T}}^{\mathrm{sim}}$ and $p_{\mathrm{T}}^{\mathrm{rec}}$ are the simulated and reconstructed transverse momenta, respectively. In the following the resolution is indicated as $\sigma(\frac{q}{p_T})$. The resolution depends on the geometry of the detector and the properties of each detector component. Although it is complicated and can only be estimated by Monte Carlo samples, it approximately holds a relation of $\sigma(\frac{q}{p_T}) = \sqrt{A_N} \cdot \frac{\sigma_T}{L^2} \cdot \frac{p_T}{|qB|}$, where, σ_T is the uncertainty associated with position measurements, L is the track path length, B is the magnitude of the magnetic field, $A_N = \frac{720(N-1)^3}{(N-2)N(N+1)(N+2)}$ and N is the number of measurements [46]. In addition, multiple-scattering also introduces a constant term to the resolution $\frac{\delta p_T}{p_T} \simeq 0.045\frac{1}{B\sqrt{LX_0}}$. The resolution depends on the position resolutions

of each measurement, the p_T itself, the magnetic field, the number of measurements, and the length of the lever arm.

The q/p_T resolution as function of p_T for the standalone, tracker track and global muon reconstruction are shown in figure 4.11. The resolution for the standalone muon reconstruction ranges from 8% in the barrel to 40% in the endcap, matching the design performance of the muon system [34]. The resolution degrades in the endcap regions due to the more complex environment in which the endcaps are embedded; the integral of the magnetic field decreases, the magnetic field has large inhomogeneities, and it is no longer solenoidal.

The two curves between tracker track and global muon reconstruction do not differ much for low-p_T; the main differences are at high η. The benefit of including the hits reconstructed in the muon chambers becomes evident for momenta greater than 200 GeV (figure 4.11). The main reason of this behavior is that the path length is much longer when adding muon hits; this effect dominates over multiple scattering when the muon momentum is large.

The charge identification probability has been evaluated for the different stages of the reconstruction. In figure 4.12, the probability to assign the correct charge is shown as a function of η.

The correct charge assignment probability in the muon spectrometer is above 75% for TeV-muons and reaches 99% for lower p_T muons. With the full tracking system the probability stays above 98%, even for TeV-muons. It is interesting to note that, contrary to the momentum estimation, the track reconstruction in the tracker alone has a higher probability to assign the correct sign of the charge than the full tracking system. This derives from the more complex assumptions used during the fit of the measurements collected in the whole tracking system. A better assignment can be achieved by either reviewing the assumption made at the fit level or by more heavily weighting the tracker track charge.

4.7.2 Performance of Cosmic Muon Reconstruction

In this section, the muon reconstruction performance is validated using the data taken from cosmic runs during CRAFT.

Data Selection and Event Simulation

Only events in a selected list of runs during CRAFT with stable magnetic field and good-quality data were used for the analyses described below.

In order to compare CRAFT data to the predictions obtained from simulations, a large sample of cosmic muons was generated using the CMSCGEN package [47]. To correctly reproduce angular and momentum distributions of cosmic rays in the CMS cavern, a detailed description of the CMS access shafts and other CMS surroundings (composition of material above the cavern, geometry of the service cavern, etc.) was implemented. The detector response to the cosmic muons was simulated with the standard CMS simulation software based on the GEANT4 package [48].

Measurements with Tracks in Opposite Detector Hemispheres

The efficiency of various muon reconstruction and identification algorithms was measured by selecting events with a good-quality global muon reconstructed in one hemisphere of the detector (top or bottom), and examining whether there is a corresponding track in the opposite hemisphere, in a region of $\Delta\phi < 0.3$ and $\Delta\eta < 0.3$ around the direction of the reference track. Since this method of measuring muon efficiency is sensitive to the efficiency of the inner tracking system, only runs with correct tracker synchronization are used. To ensure that the muon traversed the entire detector, the p_T of the reference global muon track was required to be larger than 7 GeV. Two-leg muons with a topology similar to that expected in p-p collisions are selected by requiring that the distance between the PCA of the reference track to the

nominal position of p-p interactions and the position itself does not exceed 10 cm in r and 20 cm in z.

Figure 4.13 shows the efficiencies to reconstruct 2-leg global cosmic muons and their constituents as a function of pseudorapidity of reference muons.

Measurements with Tracker Tracks

In addition to the efficiency studies described above, the efficiency of the standalone muon reconstruction was measured relative to the number of tracks in the tracker and compared to that expected from the Monte Carlo simulation. Events triggered by the DT or barrel RPC detectors and containing at least one tracker track were first selected. Tracker tracks including more than 10 hits and with $|\eta| < 0.8$ and $p > 10$ GeV were defined as tags. Trajectories of these tracks were then propagated to the outer surface of the CMS detector, and a standalone muon track reconstructed by the 1-leg cosmic standalone algorithm was searched for in the nearby region.

Efficiency in the data was compared to that in the Monte Carlo simulation, calculated in two ways: a) relative to the number of reconstructed tracker tracks, as for the data; b) relative to the number of generated standalone muons. Figure 4.14 shows reconstruction efficiencies for standalone muons as a function of the tracker track η, p_T, polar angle ϕ, and the z coordinate of the muon entry point into the detector. One can see that the standalone muon efficiency in the data is about 98-99%, except for small regions at the boundaries between the barrel wheels ($z \sim \pm$ 200 cm and $\eta \sim \pm$ 0.2). The efficiency remains high at the largest p_T values studied, of the order of 1 TeV. As expected, no dependence on ϕ is observed. Good agreement with the Monte Carlo efficiency calculated relative to the generated number of muons confirms the validity of the method used.

Momentum Resolution

The data-driven muon momentum resolution using 2-leg muons was studied as follows. A pure sample of events with exactly one pair of tracks on top and bottom hemispheres are selected. Each of the muon tracks should have at least one hit in the pixel detector and at least eight hits in the strip tracker. For each pair of muons in selected events, $\sigma(q/p_T)$ is defined as

$$\sigma(q/p_T) = \frac{(q/p_T)^{\text{upper}} - (q/p_T)^{\text{lower}}}{\sqrt{2}(q/p_T)^{\text{lower}}}, \tag{4.12}$$

where $(q/p_T)^{\text{upper}}$ and $(q/p_T)^{\text{lower}}$ are the ratios of the charge sign to the transverse momentum for the upper and the lower tracks, respectively.

The q/p_T resolutions obtained with various muon reconstruction algorithms in various bins of p_T are shown in figure 4.15. In the high-p_T region, the resolution obtained with TPFMS exceeds that of the global muons and of the tracker-only tracks, as expected.

Similar as in the efficiency study, the data-driven muon momentum resolution using 1-leg standalone muons was measured by comparing the p_T of 1-leg standalone muons and tracker tracks. The q/p_T resolution is defined as

$$\sigma(q/p_T) = \frac{(q/p_T)^{\text{sta}} - (q/p_T)^{\text{tk}}}{(q/p_T)^{\text{sta}}}. \tag{4.13}$$

The q/p_T resolutions obtained using CRAFT data and MC samples in various bins of p_T is shown in figure 4.16. The resolutions measured using CRAFT data and MC samples agree very well and the resolution is slightly better with data than with MC.

Charge Assignment

The rate of charge misassignment is measured by checking the number of times the two measurements of the charge of the same muon, in the top and bottom hemispheres, disagree.

Strict quality selections are applied as discussed in the charge ratio analysis in Chapter 6. The charge misassignment ratios in bins of transverse momentum of the

tracker track reconstructed in the top hemisphere for different muon reconstruction algorithms are shown in figure 4.17. As expected, the measurement of the charge provided by the standalone muon reconstruction is less accurate than that in the tracker in the whole p_T range. At high-p_T values, the most accurate charge assignment is given by the dedicated high-p_T muon reconstruction algorithms.

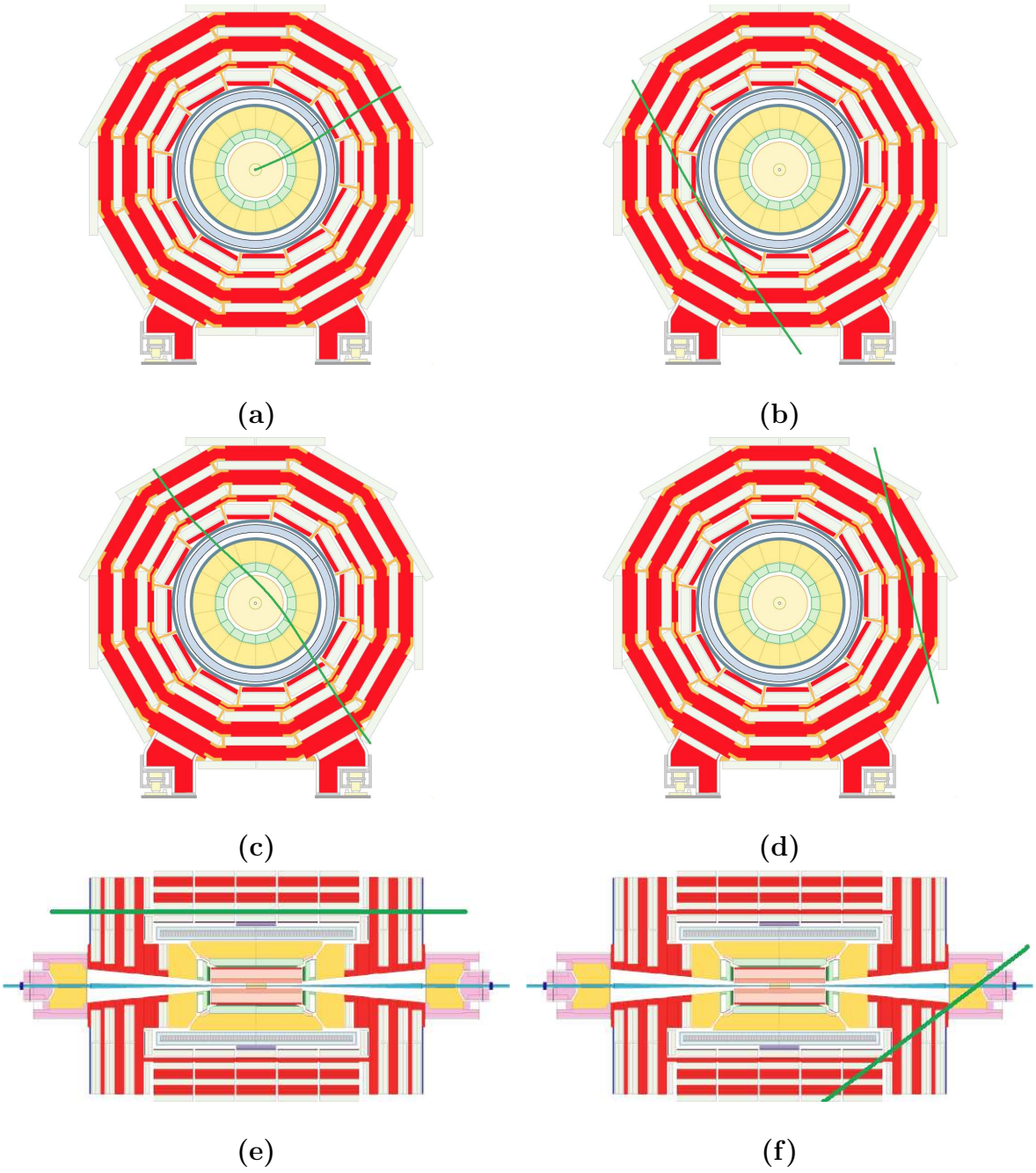

Figure 4.3. Illustration of the differences among muons from *p*-*p* collisions, different types of cosmic muons, and beam-halo muons. (a) Muons from collisions always propagate from the center to the outside; (b) Cosmic muons penetrate the detector and leave signals in opposite hemispheres; (c) Cosmic muons leave signals in the tracker system and both hemispheres of the muon system; (d) Cosmic muons leave signals in only a few muon detector layers; (e) beam-halo muons penetrate the detector and leave signals in both endcap regions; (f) Cosmic muons enter the endcap region and leave from the barrel region of the detector (or vice versa, in the upper part of the detector).

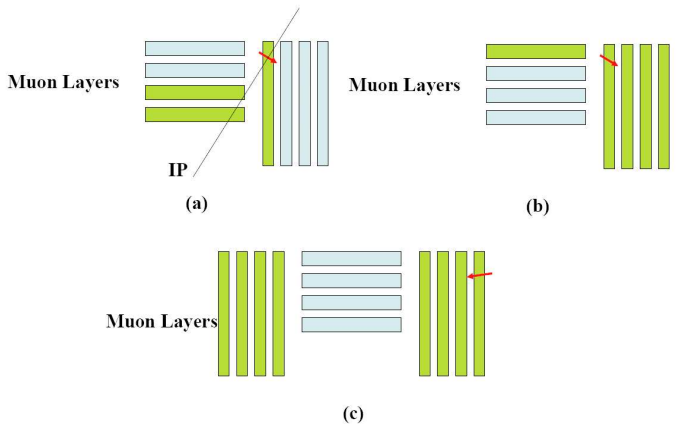

Figure 4.4. Illustration of the differences between the two navigation methods using a simplified geometry: (a) Standard Navigation, (b) Direct Navigation, (c) Direction Navigation for beam-halo muons. The muon layers marked as green (or dark shadow) are the chosen compatible layers for a given trajectory state marked as an arrow.

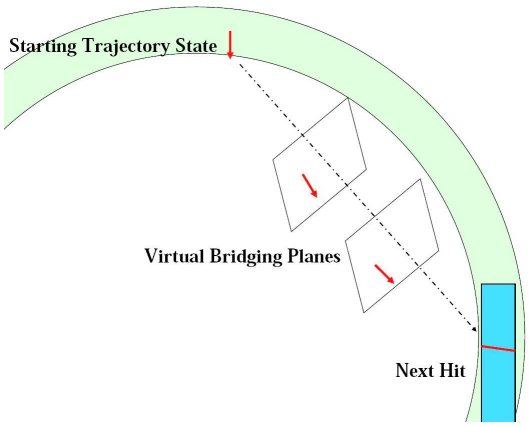

Figure 4.5. Illustration of propagation inside the magnetic coil.

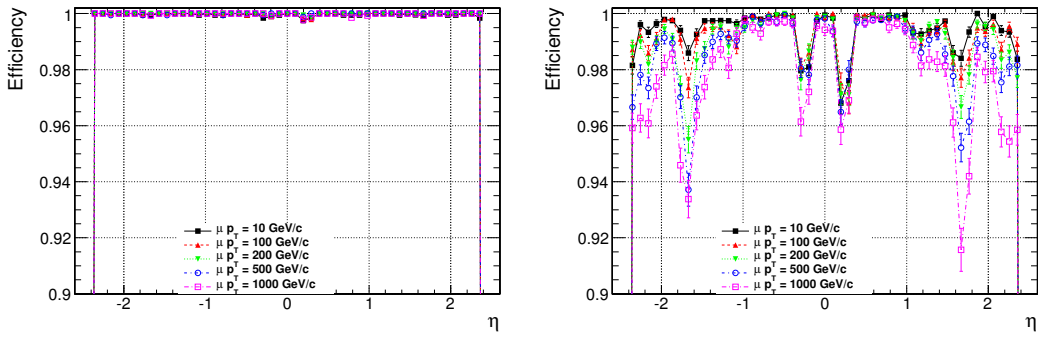

(a) ε_{seed} **vs.** η **(b)** $\varepsilon_{sta,seed}$ **vs.** η

Figure 4.6. (a) Efficiency of the muon seed reconstruction in the muon spectrometer as a function of η, for single muon samples with different p_T. (b) Algorithmic efficiency of the standalone muon reconstruction in the muon spectrometer as a function of η and ϕ, for single muon samples with different p_T.

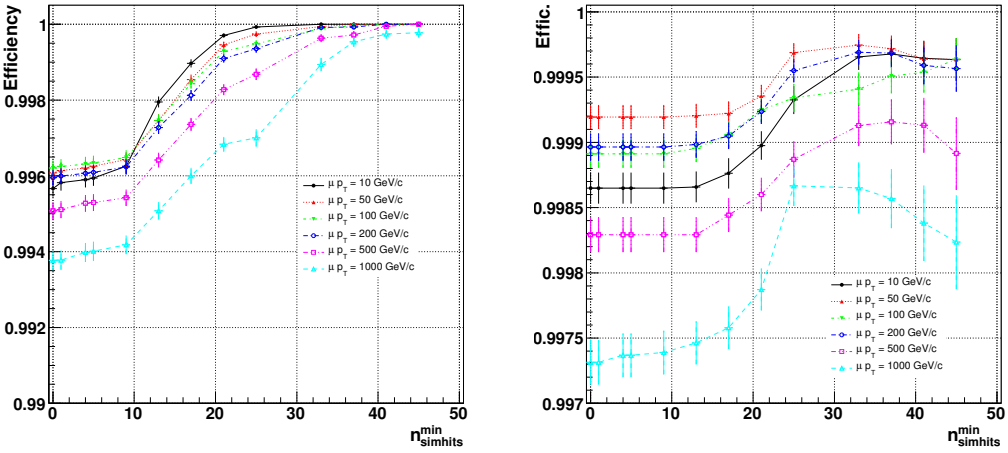

(a) ε_{seed} **vs** $n^{min}_{simhits}$ **(b)** $\varepsilon_{sa,seed}$ **vs** $n^{min}_{simhits}$

Figure 4.7. Efficiency as a function of the minimum required number of simulated hits in the muon spectrometer for seeding (a) and standalone muon reconstruction (b), for single muon samples with different p_T.

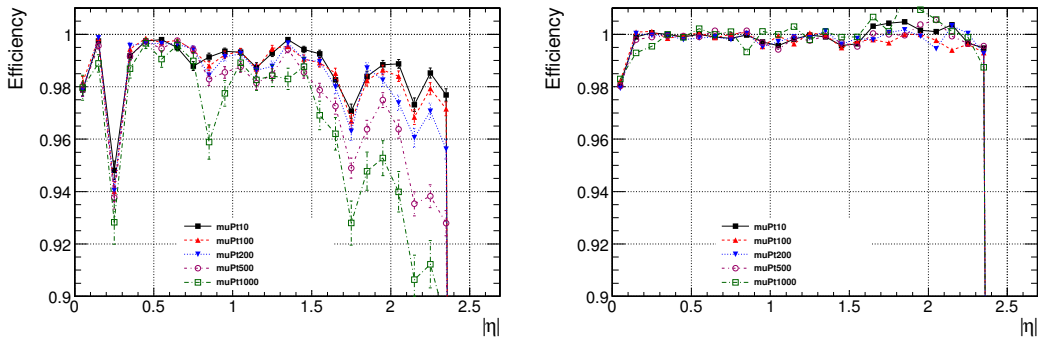

(a) $\varepsilon_{glb,sim}$ **vs** η **(b)** $\varepsilon_{glb,sta}$ **vs** η

Figure 4.8. Algorithmic efficiency of the global muon reconstruction over simulated track (a) and standalone muon reconstruction (b) as a function of η for single muon samples with different p_T.

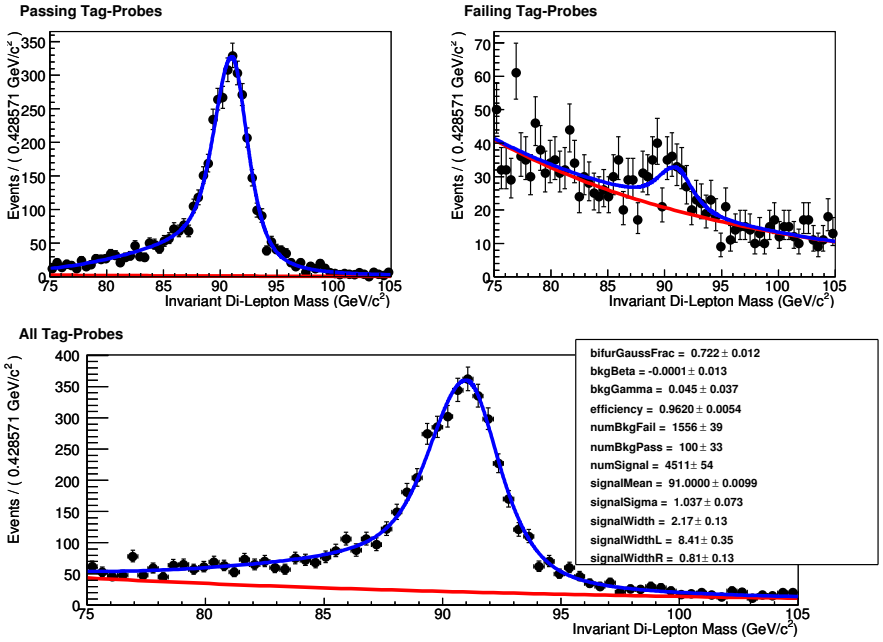

Figure 4.9. Tag-and-probe Z reconstruction efficiency: Multiple bin fit $30.0 < p_T < 40.0$ GeV, $-2.4 < \eta < 2.4$.

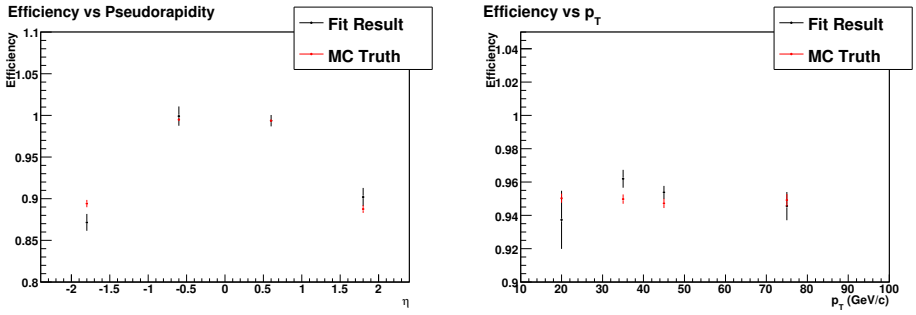

(a) (b)

Figure 4.10. Comparison of the results of the efficiency measurements from the tag-and-probe method with the same efficiencies from MC truth. The examples are from one piece of the overall efficiency measurement, namely the standalone muon reconstruction efficiency.

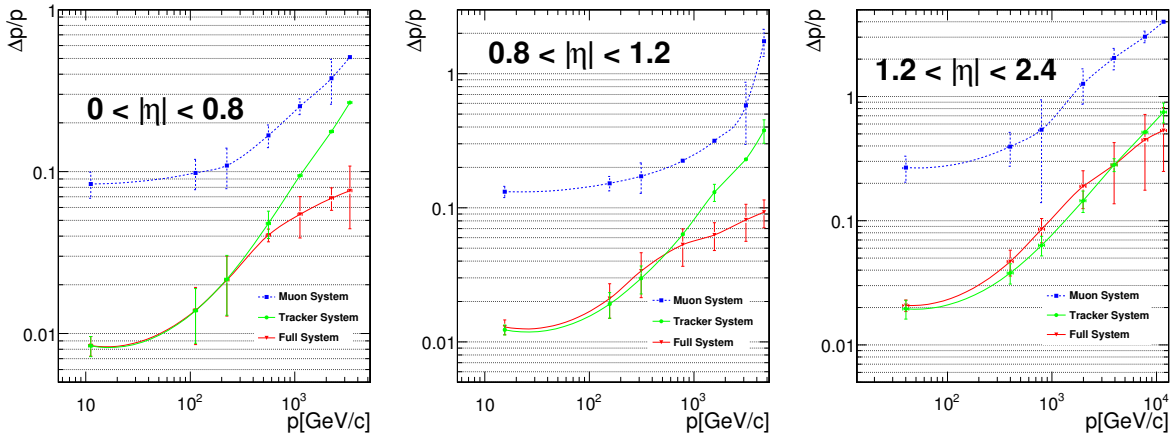

(a) (b) (c)

Figure 4.11. Resolution on q/p with the tracker alone, with the muon spectrometer alone and with the full CMS tracking system, as a function of p.

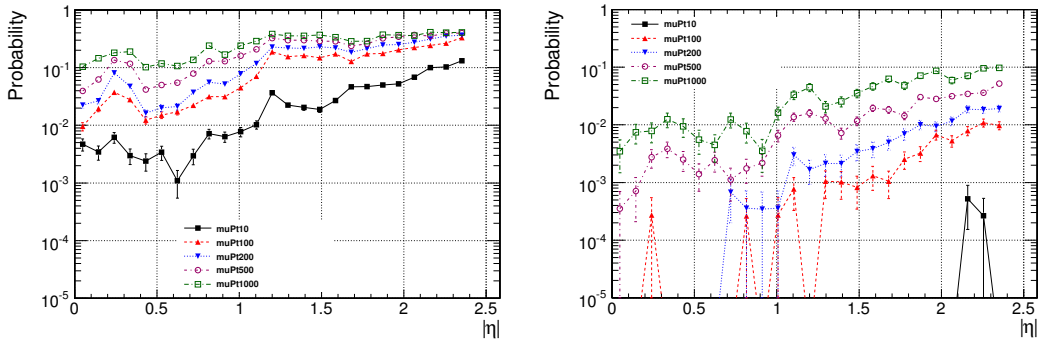

Figure 4.12. Charge mis-assignment probability for standalone muons (a) and global muons (b) as a function of η, for single muon samples with different p_T.

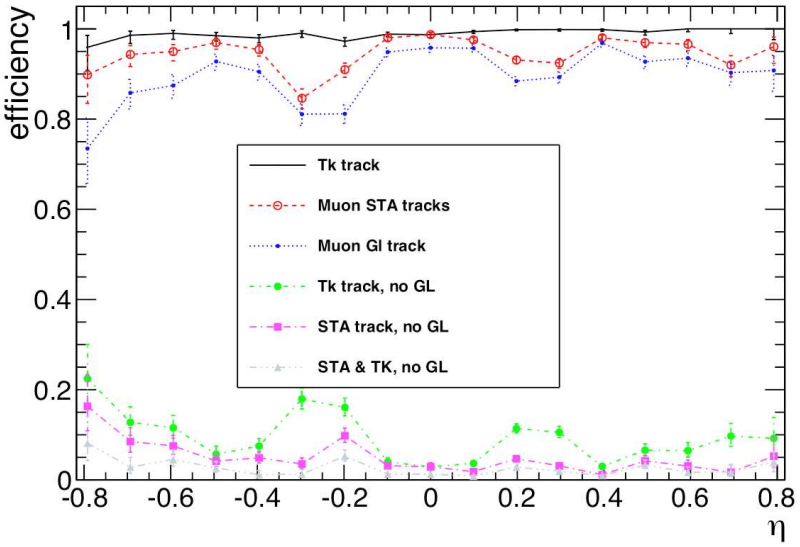

Figure 4.13. Muon reconstruction efficiencies as a function of reference-track η, for cosmic-muon algorithms. Three curves at the top, from top to bottom: 2-leg tracker track efficiency (black line); cosmic standalone-muon efficiency (open circles); efficiency for 2-leg global muons (filled blue circles). Three curves at the bottom show efficiencies of finding various components of the global muon track when the track itself is not found (see the legend).

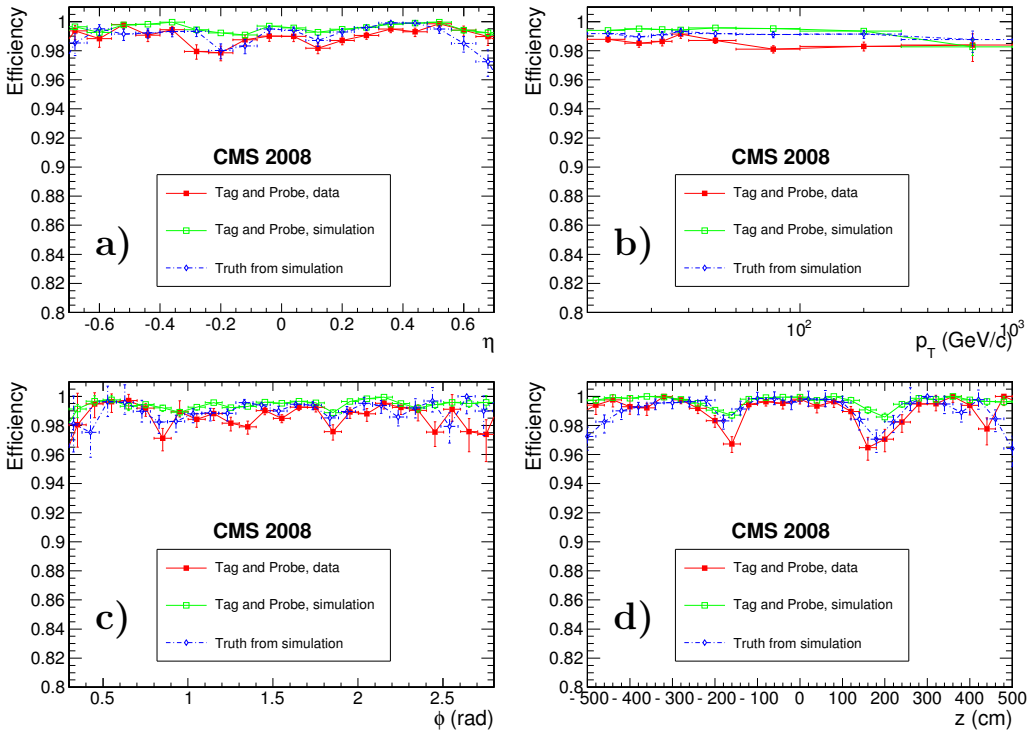

Figure 4.14. Reconstruction efficiency for 1-leg cosmic standalone muons in the data (filled squares) and in the Monte Carlo simulation (open squares) as a function of a) η, b) p_T, c) ϕ and d) the z coordinate of the muon entry point into the detector. Also shown is the Monte Carlo efficiency calculated relative to the number of simulated standalone muons (labeled "MC truth" and shown in open diamonds).

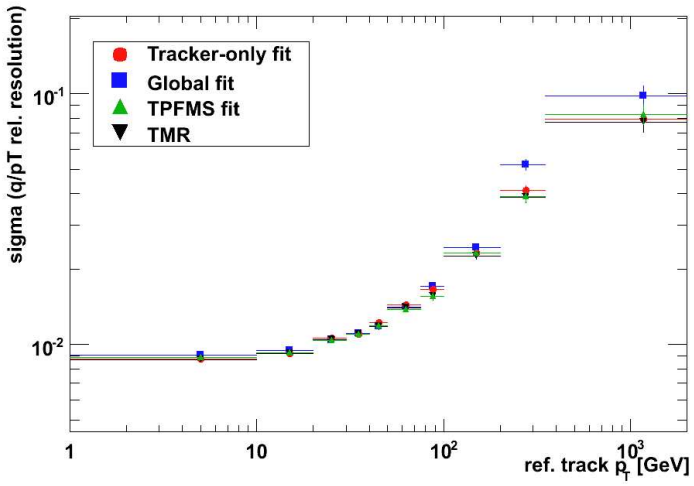

Figure 4.15. q/p_T resolutions for various muon reconstruction algorithms (see legend) as a function of p_T^{lower}.

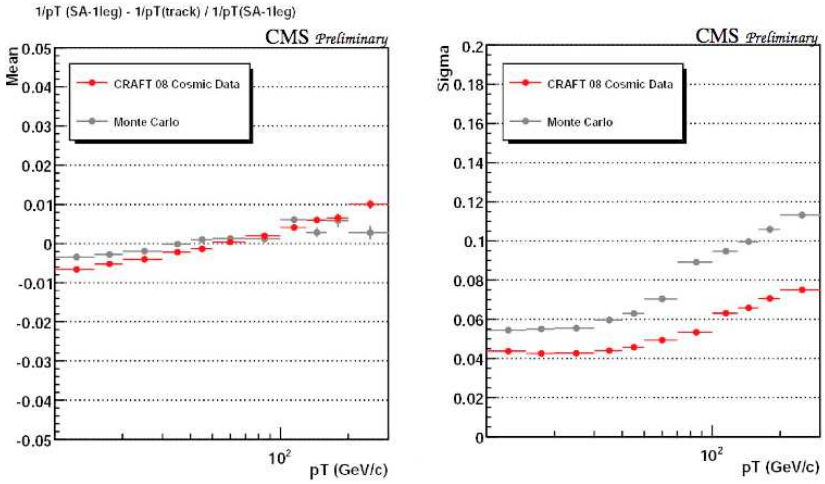

Figure 4.16. q/p_T resolutions for 1-leg standalone muons as a function of p_T^{sta} measured from data and MC sample.

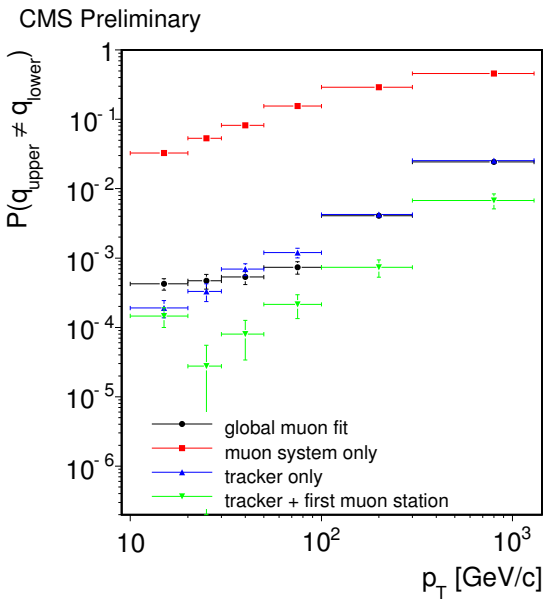

Figure 4.17. The charge misassignment ratio as a function of p_T of the tracker track reconstructed in the top hemisphere, for standalone muons (red squares), tracker tracks (blue triangles), global muons (black circles), and the TPFMS refit (green upside-down triangles).

5. MUON HIGH-LEVEL TRIGGER

The CMS muon reconstruction software has been designed using the concept of *regional reconstruction* in order to allow its use in both offline reconstruction and the High-Level Trigger system. Employing regional reconstruction results in very small parts of the detector actually needing to be reconstructed before a physics object is validated. As an example, the amount of information needed to reconstruct a muon track in the silicon tracker represents less than a few percent of the total tracker data volume. The software does not reconstruct the entire tracker, but only the part which can possibly be involved in a charged particle track that can be compatible with the hits in the muon chambers. This results in savings on the overall CPU power needed to process the events.

By employing this concept of regional reconstruction events are reconstructed in a piece-wise fashion in several HLT sub-levels, only after each selection step is passed. It can be seen that the reconstruction and selection in the HLT steps are closely related and are in fact interleaved. A major advantage of this approach is that CMS can aim to really have the same code running in the online and offline selections. This is a major advantage and should lead to a system that is much easier to run, maintain, and monitor.

The muon reconstruction algorithm used by the HLT is seeded by the muon candidates found by the L1 muon trigger. These seeds define a region of interest in the muon system, in which local reconstruction is performed. Once triggered by the L1 trigger, information from each sub-detector corresponding to one event is sent to computer processor farm where the HLT algorithms are executed. The CPU time of the HLT is optimized by regional reconstruction and by rejecting events as early as possible. The basic strategy is to reconstruct each physics object in different subsystems which can be used to make quick decisions first and then involve information

from more subsystems and to make decisions at a higher level. Reconstruction and selection of a muon at HLT includes the following steps: a step of reconstruction in the muon system called L2, a step of selection based on L2 muons, a step of isolation selection based on L2 muons and calorimeter information, a subsequent reconstruction step involving the tracker and muon system called L3, a selection step based on L3 muons, and another step of isolation selection based on L3 muons and tracker and calorimeter information. In each step, a set of selection criteria rejects a significant fraction of the events processed by the previous step. The rate of events that need to be processed through each step is decreased to reduce the CPU time. Reconstruction and selection are closely intertwined in the HLT. The HLT should reconstruct the minimum amount of detector information needed to apply a set of selection criteria that reject as many background events as possible while keeping as many of the desired physics events as possible for further processing.

5.1 L2 Muon Reconstruction

The L1 muon candidate with information of η, ϕ, p_T is the input to build L2 trajectory seeds, which makes the L2 reconstruction only work in a limited region of the whole muon detector. The HLT does not reconstruct muons not selected in L1.

The L2 trajectory seeds are created using the L1 parameters (η, ϕ, p_T) and their associated uncertainties. Starting from the L2 trajectory seeds, the same trajectory builder as in offline standalone muon reconstruction is used to estimate the track parameters at the PCA.

5.2 L2 Muon Isolation

The calorimeter isolation and filtering step is performed at L2 for the isolated muon trigger path. The isolation filter at L2 calculates a weighted sum of calorimeter energy deposits surrounding the L2 muon in an annular cone and provides a filter decision based on whether that sum is below a specified threshold.

The offline algorithm used for calculating the muon isolation in the offline reconstruction is used in the HLT. The calorimeter towers are used as input to the isolation algorithm. The tower energies above thresholds are summed with weights in a cone of $\Delta R < 0.24$ centered on the direction of the L2 muon track taken at the interaction region, with the update at vertex applied. The sum of energy in a veto cone is subtracted. The veto cone has a ΔR of 0.07 in ECAL (0.1 in HCAL) and is centered around the state of the L2 muon propagated to the inner ECAL surface (see figure 5.1).

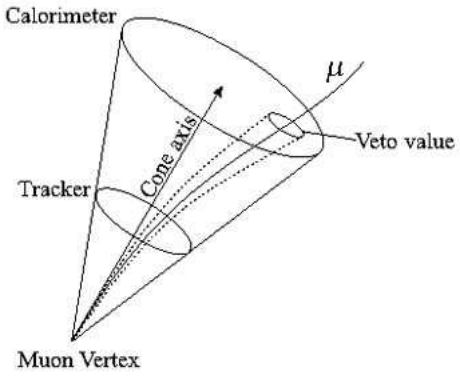

Figure 5.1. Sketch of the cones used to compute the calorimeter deposit. The main cone is centered on L2 at vertex and the veto cone around the L2 state propagated to the ECAL surface.

A L2 muon is tagged as isolated if the weighted sum is lower than a certain η-dependent threshold.

5.3 L3 Muon Reconstruction

In the L3 muon reconstruction, the muon trajectories are extrapolated from the muon system to the silicon tracker system to include silicon hits. Different from offline global muon reconstruction, there are no existing tracker tracks available in the HLT, so the tracker tracks need to be reconstructed in the L3.

The L3 muon reconstruction is composed of several steps. Starting from a L2 reconstructed muon, trajectory seeds in the tracker system are generated by information extrapolated from the muon trajectory. There are two categories of seeding algorithms available to build trajectory seeds in the tracker: *inside-out* algorithms which build trajectory seeds on the inner pixel layers and perform pattern recognition inside-out, and *outside-in* which build trajectory seeds on the outer silicon layers and perform pattern recognition outside-in.

In the *inside-out hit-based* approach, referred to as IOHit, a region of interest in the tracker is defined to perform a regional seed building algorithm. The determination of the region of interest is based on the track parameters and uncertainties of the extrapolated L2 muon trajectory with vertex constraint. Then the standard hit-pair and hit-triplet generators are used to form pair and triplet combinations of hits on adjacent tracker layers. The hit-pair and hit-triplet generators are restricted to consider only hits that are within the defined tracking region of interest, which is a rectangular η-ϕ region. The selected hits are parameterized to give an initial direction and trajectory state which are used to define a trajectory seed.

In the *outside-in hit-based* approach, referred to as OIHit, silicon layers compatible with the muon trajectory are chosen according to the compatibility of η coverage. The selected silicon strip tracker outer barrel (TOB) and tracker end cap (TEC) layers are ordered from outside-in. The L3 seeds are generated at the first compatible layer which contains compatible measurements. The states, after updating the compatible measurements, define the L3 seeds.

In the *outside-in state-based* approach, referred as OIState, a trajectory state propagated from each L2 muon to the outer silicon layer is used directly to build the L3 seed.

Starting from the trajectory seeds, the combinatorial track finder builds trajectories in the tracker system [34]. Initial trajectory candidates are created from each L3 trajectory seed, collecting the hits and using the track parameters estimated during the seeding stage.

Then the combinatorial track finder grows a tree of trajectory candidates from successive layers in the tracker. The track parameters obtained from the previous stage are used to search for compatible hits in the next reachable layers. Invalid hits are added if a layer is crossed but no compatible hits are found on the layer. The track parameters are then separately updated with each compatible hit, subsequently creating multiple trajectory candidates. The combinations arise from the many compatible hits which can be found on the successively crossed layers. The "tree" is grown by repeating the step until either there are no more layers on which to look for hits or there are no more trajectory matching requirements for continuing pattern recognition. The number of leaves at each step is limited to the five trajectories with the best χ^2, taking into account a penalty on missing hits.

The final set of reconstructed hits are refitted to avoid bias from the initial track parameters estimation at seeding stage and to obtain the best track parameter measurements along its path. Two independent Kalman fits of the hits are performed forward and backward. The track parameters measurement is obtained at each layer by averaging the result from the forward and the backward fit.

After the combinatorial track finder built trajectories in the tracker system, all the tracker track candidates are compared with the muon track to select those matched with the muon track.

The matching of tracker and muon tracks is performed by comparing the trajectory parameters with different strategies, as described in the previous chapter. After matching the tracker trajectories with the L2 muon trajectory, a subset of tracker trajectories is processed to the next step of the global refit. A global refit is applied to fit a track using the hits from both the tracker track and the L2 muon track. The global refit algorithm performs a track fit for each tracker track - L2 muon pair. After all the refits, the L3 muon track with the most hits and the best χ^2 is chosen. Thus, for each L2 muon there is a maximum of one L3 muon that will be reconstructed. The final track parameters are then calculated at the PCA by extrapolating the innermost measurement of the global track.

5.4 L3 Muon Isolation

In addition to the calorimeter isolation performed after L2 and before L3 tracking, some additional isolation calculation is made based on the tracker information. To save HLT CPU time, only pixel track isolation is performed. Contrary to the L3 track reconstruction, the pixel tracks are reconstructed globally (i.e. with no regional restriction). The pixel track reconstruction starts with combinations of pixel hits in a pair of pixel layers. All outermost hits are considered. The inner layer is searched for compatible hits with a circle trajectory estimation between the outer hit and the interaction region. The compatibility of the second hit is estimated assuming the uncertainties on the interaction region to be 15.9 cm and 2 mm in the longitudinal and transverse directions respectively. The interaction region is set from the configuration to be at the origin. These above assumptions can not affect the final pixel track parameters and do not affect the pixel triplet finding efficiency because the assumed uncertainty covers the estimated uncertainty on the beam spot position and displacement. Each compatible triplet of pixel hits forms a pixel track. The track parameters are extracted from an helix projection through the three pixel hits; the estimation of the interaction region position is not used. Pixel tracks with a global χ^2 greater than 1000 or an estimated p_T less than 0.1 GeV are rejected.

5.5 Muon Trigger Rates and Timing

The single muon inclusive trigger rate was studied in a realistic scenario. The study focused on the scenario at the early phase of data taking at the LHC, and thus all trigger rates were normalized to an instantaneous luminosity of $10^{32}\text{cm}^{-2}\ \text{s}^{-1}$ and possible selection cuts were suggested based on this luminosity.

The samples used for the study were simulated with a center-of-mass energy at 10 TeV. The generator rates of different physics processes are listed in table 5.1. The generator-level rates of muons with different sources are drawn in figure 5.2.

Sample	No. of Events	Cross Section	Effective Cross Section
Inclusive $pp \rightarrow \mu + X$	5126260	51.56 mb	118845.8 nb
$W \rightarrow \mu\nu$	1098386	11865 pb	8.1987 nb
$W \rightarrow \tau\nu$	1100000	11960 pb	11.96 nb
$Z \rightarrow \mu\mu$	1M	1.232 nb	0.627 nb
$Z \rightarrow \tau\tau$	1M	11.84 nb	11.84 nb
Drell-Yan$\rightarrow \mu\mu$	0.1M	12.9 nb	3.986 nb

Table 5.1
Samples used for the trigger rate study.

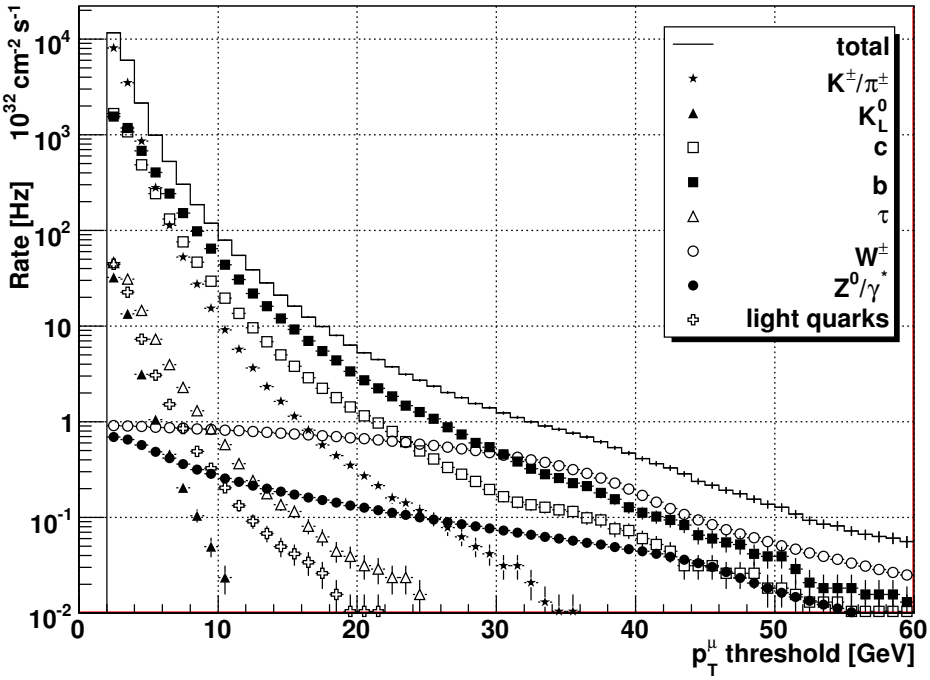

Figure 5.2. Muon rates of various physics contributions at generator level.

Figure 5.3 shows the L1 muon trigger rate, which is the input for the processing later on. A large fraction of the L1 muon trigger rate is due to low-p_T muons which are reconstructed with a high p_T. Most of them are decays-in-flight from pions and

kaons, and decays from b/c. The L1 rate is not sensitive to the p_T threshold for p_T threshold above 20 GeV.

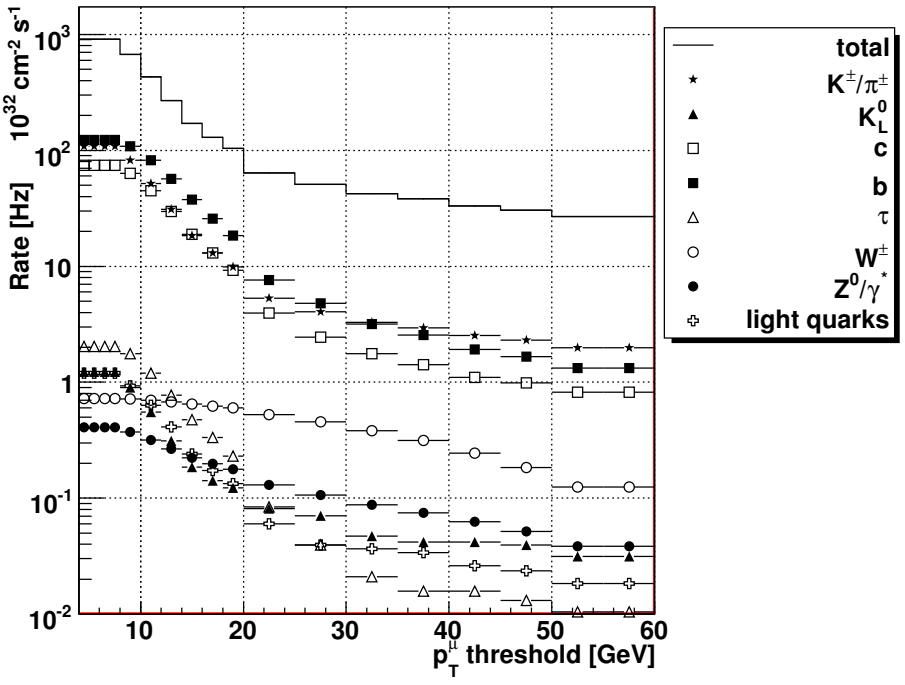

Figure 5.3. Muon rates of various physics contributions at L1.

The composition of the trigger rates passing L2 muon reconstruction and selection is presented in figure 5.4. At this level, muons decaying from pions and kaons are greatly reduced, and muons decaying from b/c dominate in all the ranges. The rate of muons coming from b/c decays becomes close to the rate of W contributions after the L2 muon selection and isolation, as presented in figure 5.5. The composition of the trigger rates passing L3 muon reconstruction is presented in figure 5.6. The contribution from b/c still dominates with p_T threshold up to 30 GeV. However, if requiring L3 isolation and a p_T threshold in the range of 15 to 20 GeV, the W and Z processes become the leading contribution to the single muon trigger rate, as shown in figure 5.7. To select events with isolated muons in the final state, like $W \to \mu\nu$ and $Z \to \mu\mu$, L3 isolation is a powerful tool to reject muons from b/c and K/π while still

keeping high efficiencies for physics processes of interest. The overall reconstruction and selection efficiency for $W \to \mu\nu$ is illustrated in figure 5.8.

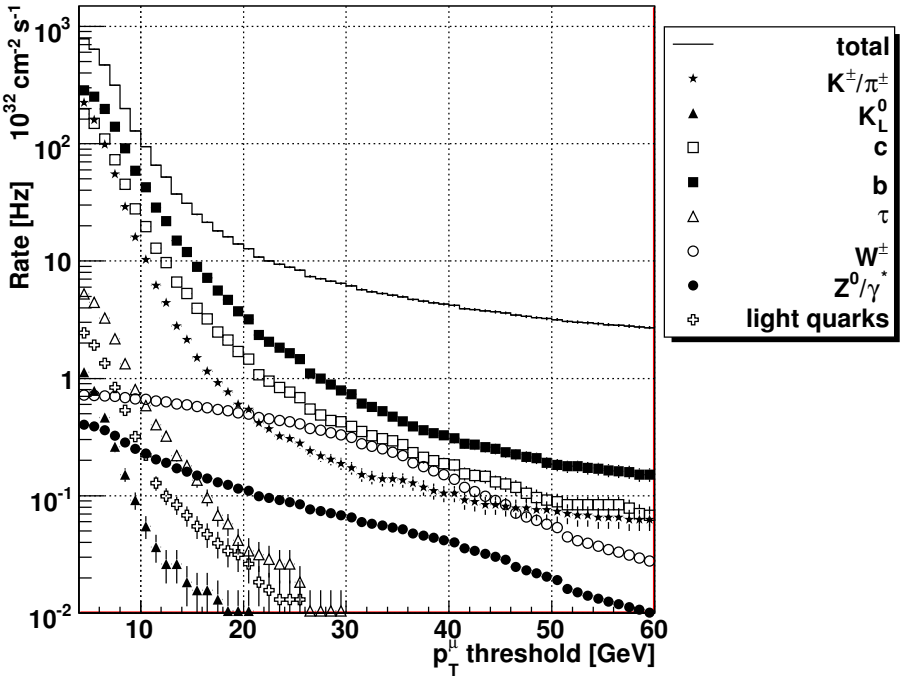

Figure 5.4. Muon rates of various physics contributions at L2.

As described in Chapter 3, the total CPU time used in the HLT depends on all the software components as well as the rejection factors, which depends on the input sample. Since the dominant source of muons is minimum bias events, the total execution time for the Muon HLT is thus estimated by the inclusive $pp \to \mu + X$ sample, as shown in figure 5.9. The multi-peak structure is due to multiple muons in the event. Generally different seeding algorithms have similar CPU time, outside-in algorithms are faster than the inside-out algorithm because there are less L3 trajectory seeds found.

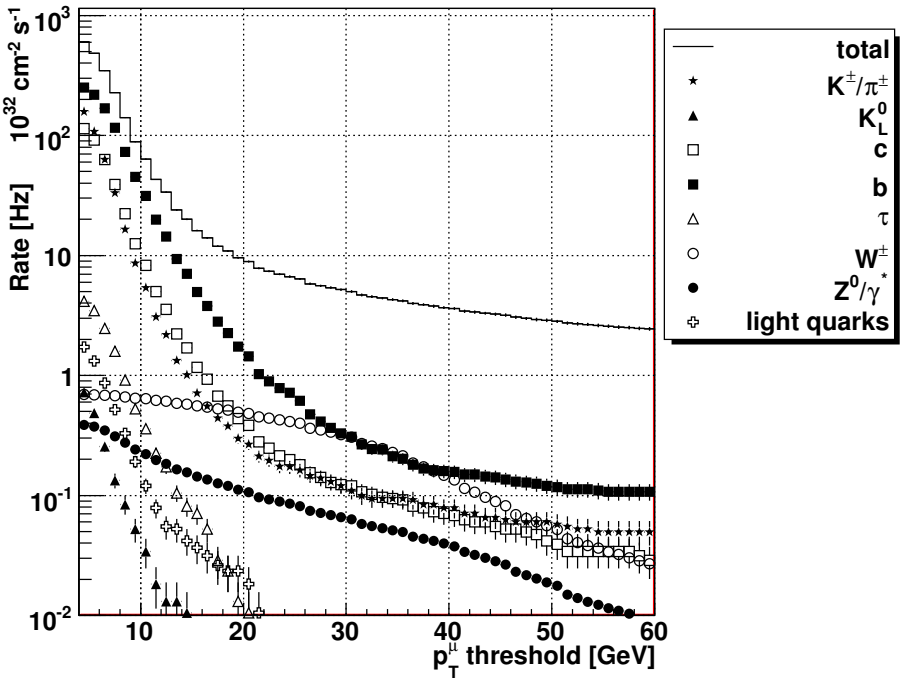

Figure 5.5. Muon rates of various physics contributions at L2 after isolation.

5.6 Performance

5.6.1 Validation of the HLT Algorithms Using Monte Carlo Samples

The performance of the muon reconstruction algorithms was evaluated using the full detector simulation under different alignment scenarios.

The efficiency of L3 muon reconstruction is estimated by dividing the number of simulated muon tracks that can be associated with a reconstructed L3 muon by the number of simulated muon tracks. The association is defined by requiring $\sqrt{\Delta\phi^2 + \Delta\eta^2}$ be less than 0.1 between a simulated track and a reconstructed track. The L3 muon reconstruction performance using different L3 seeding algorithms with single muon 10, 100, and 1000 GeV samples under two misalignment scenarios are shown in figure 5.10, 5.11, 5.12 respectively. The two outside-in algorithms have similar performance, while both of them have higher efficiency than the inside-out algorithm. All the algorithms are robust under different alignment scenarios.

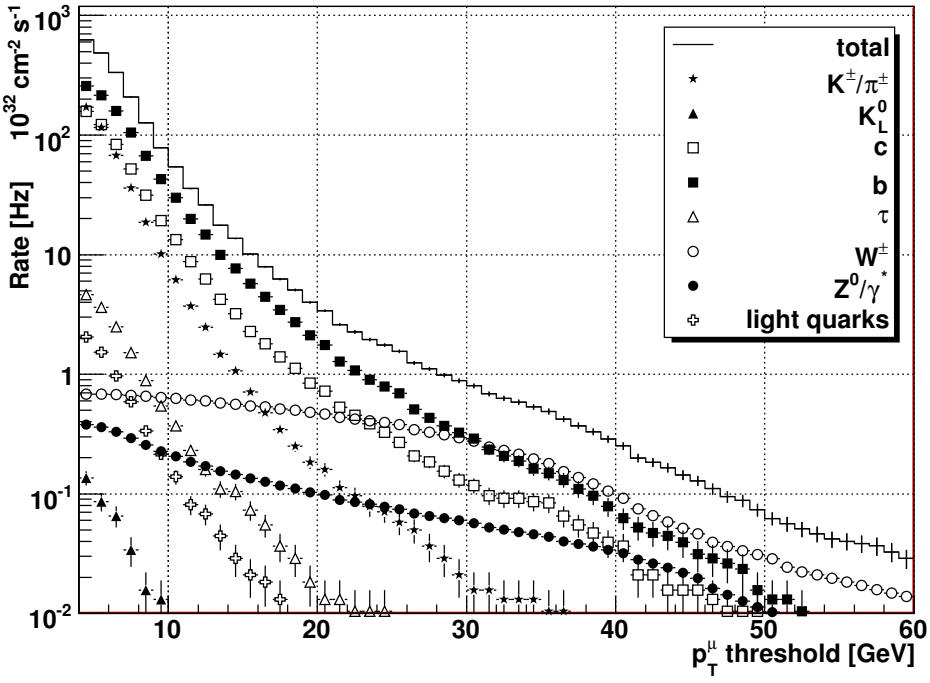

Figure 5.6. Muon rates of various physics contributions at L3.

5.6.2 Validation of the HLT Algorithms Using Cosmic Data

Since neither L2 nor L3 selections were applied during the CRAFT data taking, the expected performance of the HLT algorithms could be studied offline in an unbiased way.

L2 muon reconstruction

The efficiency of the L2 muon reconstruction algorithm was studied by selecting events with a good-quality tracker track and checking whether a corresponding L2 muon track was reconstructed. In order to ensure that the parameters of the reference track were well measured, the tracker track was required to have at least 10 hits in the strip tracker and at least one hit in the pixel detector. Muons with a topology similar to that expected in *p*-*p* collisions were selected by requiring that the PCA

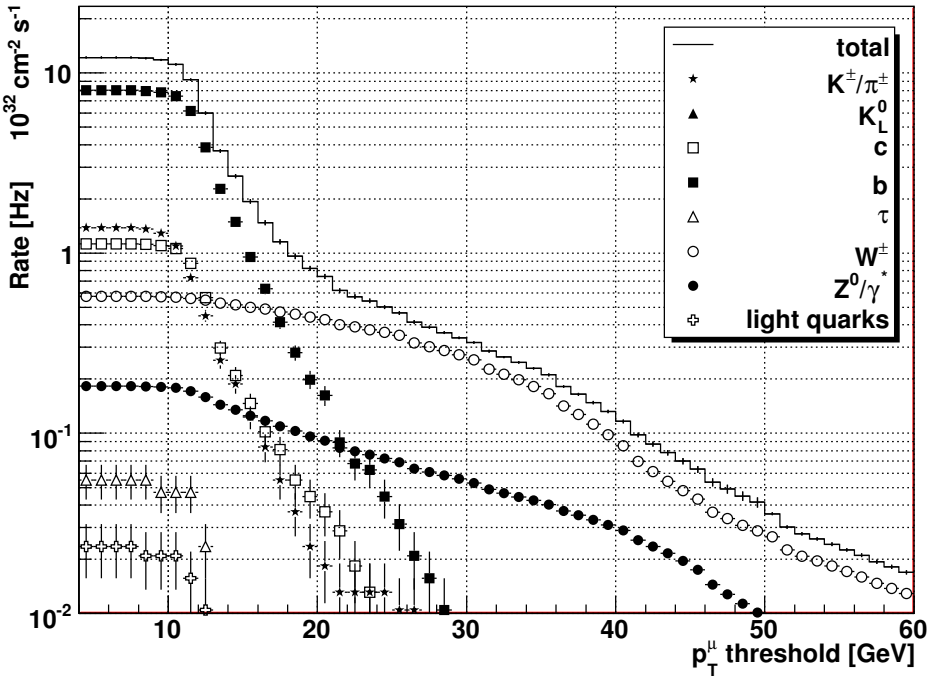

Figure 5.7. Muon rates of various physics contributions at L3 after isolation.

lies in the cylinder of $|d_{xy}| < 10$ cm and $|d_z| < 30$ cm with respect to the nominal interaction point.

The only modification to the standard L2 reconstruction algorithm made for this study was the removal of the vertex constraint in the final track fit. Figure 5.13 shows the efficiencies of the seeding step of the L2 reconstruction (left panel) and of the full L2 reconstruction algorithm (right panel) as a function of p_T of the reference track. For comparison, the corresponding efficiencies of the default offline standalone muon reconstruction, also with the vertex constraint removed, are shown superimposed. Both the seeding and the overall L2 efficiencies are close to 100% for muons with p_T above 5 GeV as expected. The overall L2 efficiency is ∼1% lower than the offline efficiency, due to a slightly less accurate seeding.

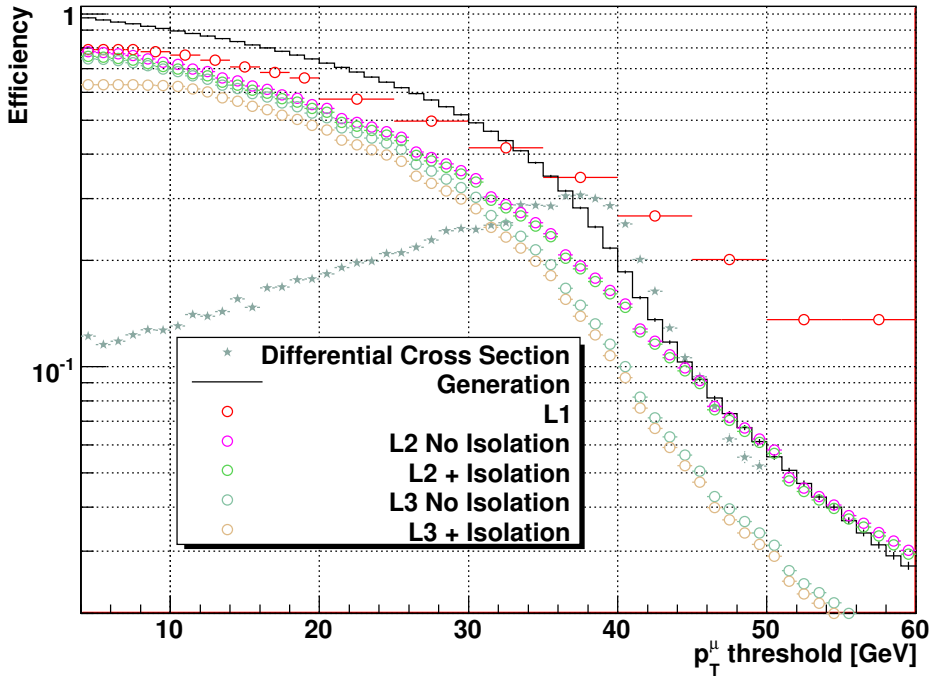

Figure 5.8. Selection efficiency of W to muons.

L3 muon reconstruction

The performance of the three L3 seeding algorithms were studied using a subset of the data collected in CRAFT with muons resembling those produced in p-p collisions.

Since the L3 muon algorithms are designed to reconstruct muons originating from the nominal beam-interaction point, a sample of collision-like muons is needed to evaluate their performance. Event selection started by requiring that there be exactly one track reconstructed in the tracker, which also travels through the pixel volume. Presence of at least two pixel hits in different pixel layers in the same hemisphere of the detector is also required. Furthermore, a "virtual" beam-spot is constructed by the tracker track and used by the L3 algorithms. Contamination from events with several muons simultaneously crossing the detector was suppressed by requiring that there be exactly one 1-leg cosmic standalone muon. Good-quality collision-like L2 muons

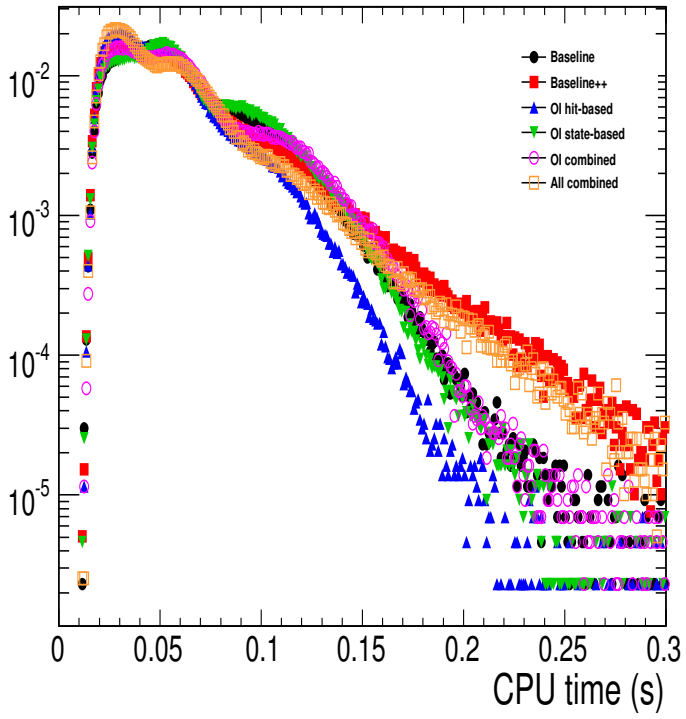

Figure 5.9. The total execution time for the Muon HLT in $pp \to \mu + X$ events for different seeding algorithms.

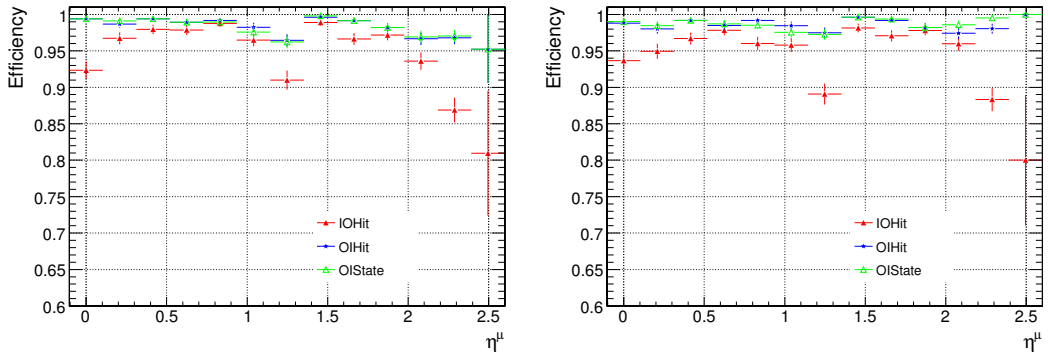

(a) **(b)**

Figure 5.10. L3 efficiency vs η for a single muon sample with $p_T = 10$ GeV under misalignment scenarios of ideal (left) and start-up (right).

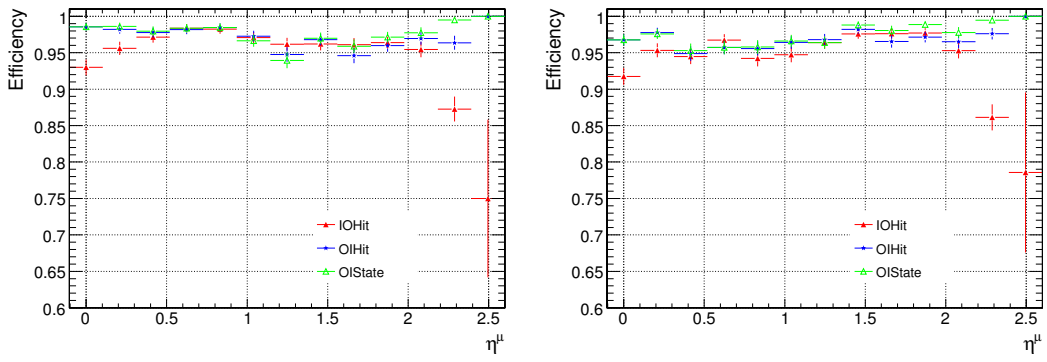

(a) **(b)**

Figure 5.11. L3 efficiency vs η for a single muon sample with $p_T = 100$ GeV under misalignment scenarios of ideal (left) and start-up (right).

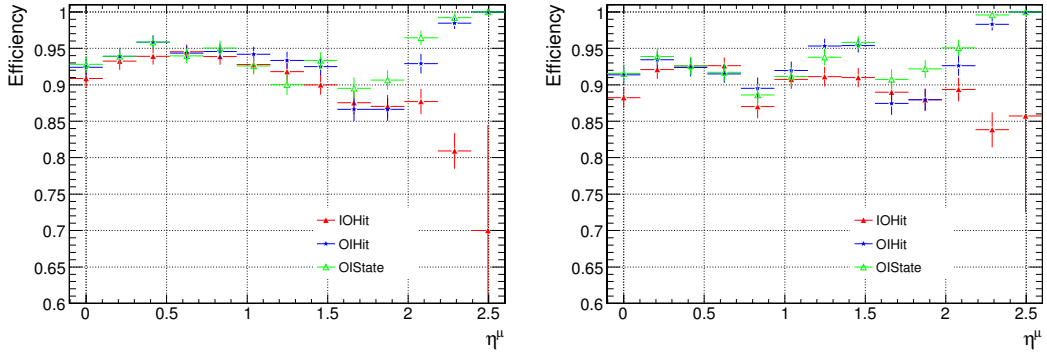

(a) **(b)**

Figure 5.12. L3 efficiency vs η for a single muon sample with $p_T = 1000$ GeV under misalignment scenarios of ideal (left) and start-up (right).

were selected by demanding that the L2 muon has $|d_{xy}| < 20$ cm, $|d_z| < 30$ cm, and more than 20 muon hits.

L3 muon reconstruction was performed individually with each algorithm (IOHit, OIHit, and OIState), and the reconstruction efficiency was calculated as a function of L2 muon track parameters. The three algorithms show similar performances with

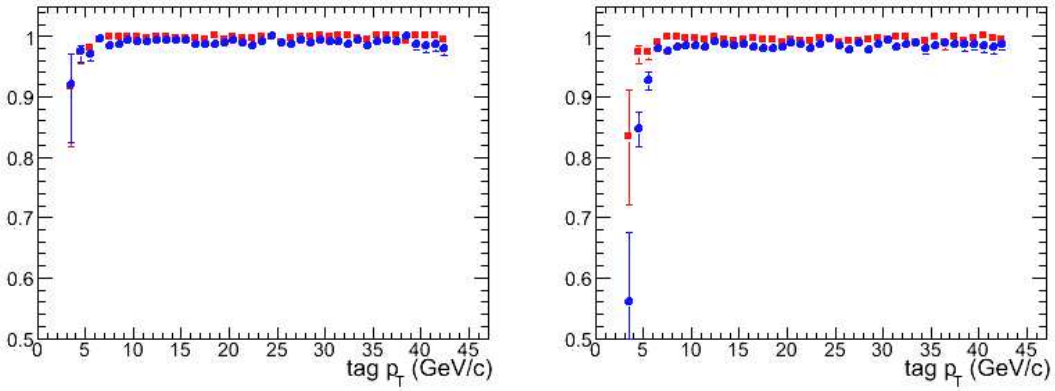

Figure 5.13. Seeding (left) and overall (right) reconstruction efficiencies for L2 (blue circles) and ppSTA (red squares) algorithms as a function of tracker-track p_T, for muons in the region $|\eta| < 0.8$ and $-2.2 < \phi < -0.9$.

a high efficiency, and no significant dependence on track parameters is observed. The result is consistent with the expectation based on MC studies.

The efficiency of L3 muon reconstruction in the upper hemisphere is about 4% lower than in lower hemisphere, which is due to a readout problem of the upper hemisphere during the first half of the CRAFT. It is not a feature of the L3 algorithms, and it has been fixed.

The L3 efficiencies as a function of the L2 muon quality cut are shown in figure 5.14. There are three criteria for L2 muon selection: d_{xy}, d_z, and number of hits per L2 muon. Three plots are made as a function of d_{xy}, d_z, and number of hits individually, while not altering the other cuts.

L2 muons that satisfy the quality cuts, $|d_{xy}| < 20$ cm, $|d_z| < 30$ cm, $n_{hits} > 20$, were used. An optimized rescaling of the L2 covariant matrix was applied, which turned out to be important for outside-in algorithms. Figure 5.15 and 5.16 show the L3 muon reconstruction efficiencies as a function of track parameters: η, p_T, d_{xy}, and d_z. As shown in the figures, there are no significant dependencies on track parameters for L3 efficiency. Both OIHit and OIState show almost the same performances, and IOHit has a slightly lower efficiency, as expected.

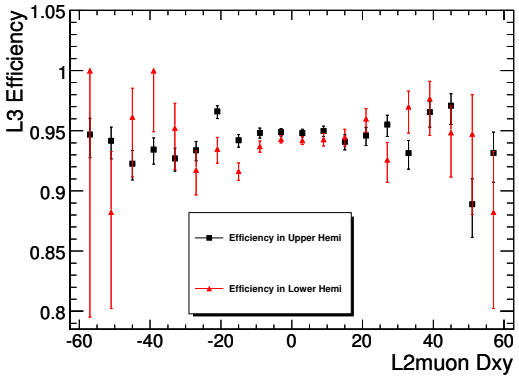

(a) IOHit eff. vs. $d_{xy}^{L2\ \mu}$

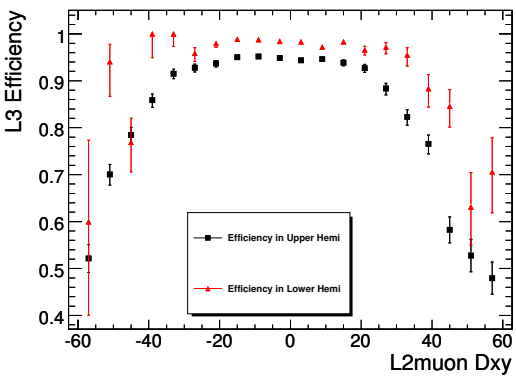

(b) OIHit eff. vs. $d_{xy}^{L2\ \mu}$

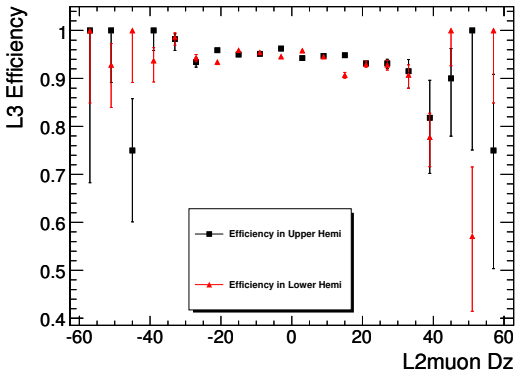

(c) IOHit eff. vs. $d_{z}^{L2\ \mu}$

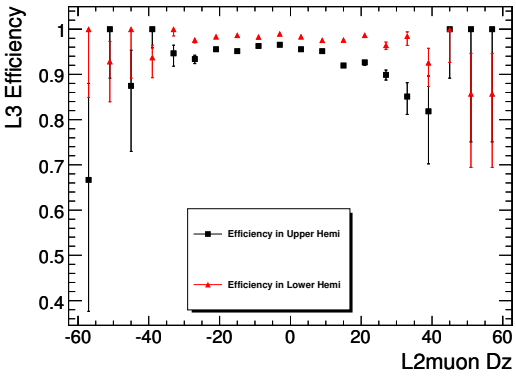

(e) OIHit eff. vs. $d_{z}^{L2\ \mu}$

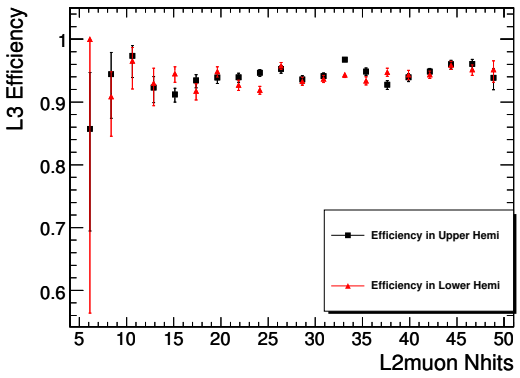

(e) IOHit eff. vs. $N_{hits}^{L2\ \mu}$

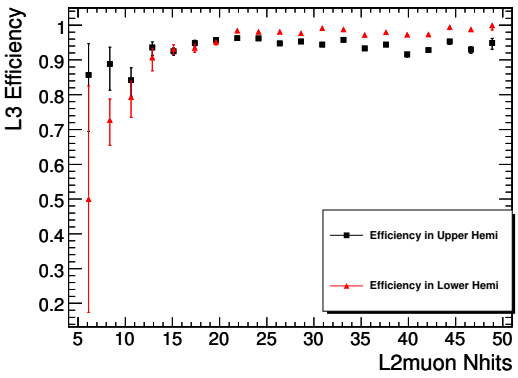

(f) OIHit eff. vs. $N_{hits}^{L2\ \mu}$

Figure 5.14. L3 muon reconstruction efficiencies in upper and lower hemispheres as a function of L2 muon d_{xy}, d_z, and n_{hits} for different L3 seeding algorithms. In efficiency vs. $d_{xy}^{L2\ \mu}$ plots, only $|d_z| < 30$ cm and $n_{hits} > 20$ are applied. In efficiency vs. $d_{z}^{L2\ \mu}$ plots, only $|d_{xy}| < 20$ cm and $n_{hits} > 20$ are applied. In efficiency vs. $N_{hits}^{L2\ \mu}$ plots, only $|d_{xy}| < 20$ cm and $|d_z| < 30$ cm are applied.

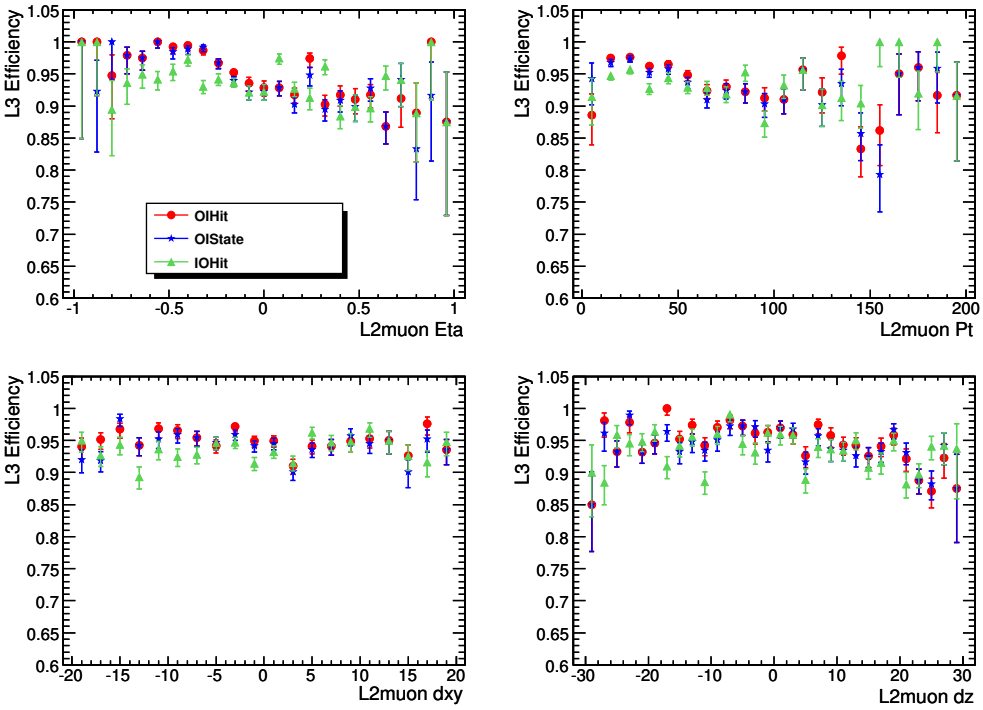

Figure 5.15. L3 muon reconstruction efficiencies as a function of track parameters. Red solid dots denote OIHit result, blue stars denote OIState result, and purple triangles denote IOHit result. In top, from left to right, x-axis is η, ϕ, and p_{T} of L2 muon, respectively. In bottom, from left to right, x-axis is d_{xy} and d_z of L2 muon, respectively. This is the result for muons in the upper hemisphere.

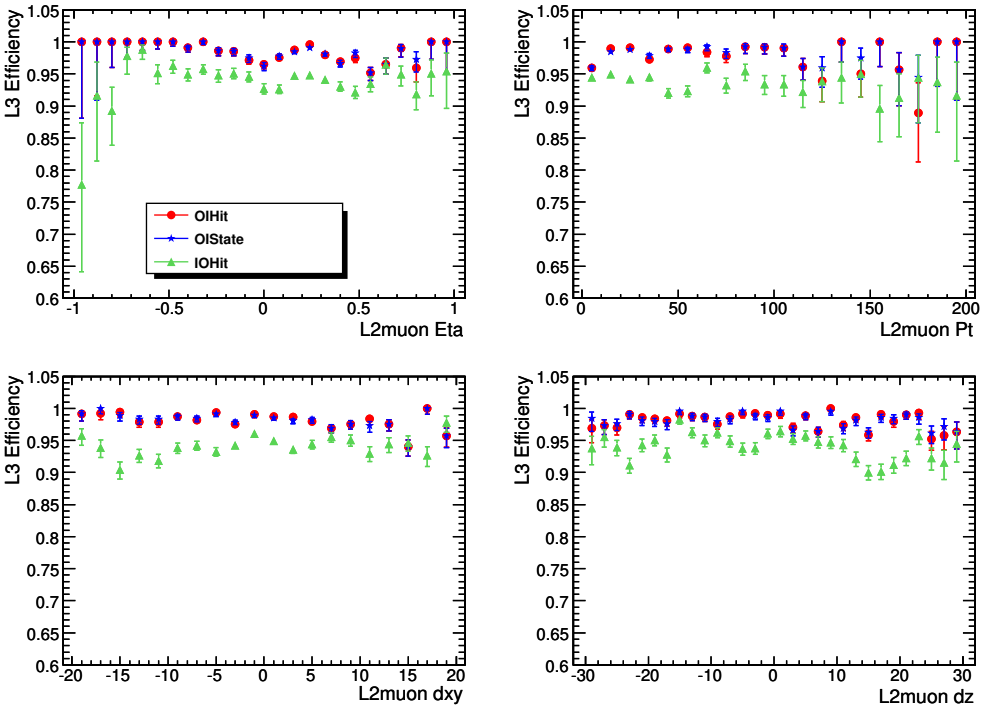

Figure 5.16. L3 muon reconstruction efficiencies as a function of track parameters. Red solid dots denote OIHit result, blue stars denote OIState result, and purple triangles denote IOHit result. In top, from left to right, x-axis is η, ϕ, and p_{T} of L2 muon, respectively. In bottom, from left to right, x-axis is d_{xy} and d_z of L2 muon, respectively. This is the result for muons in the lower hemisphere.

6. COSMIC MUON ANALYSIS

6.1 Motivation

The earth is exposed to a continuous bombardment of high energetic charged particles, usually referred to as cosmic rays. Cosmic rays are produced by extremely high-energy particles coming from astronomical objects. From the point of view of a high energy physicist, the high-energy particles serve as the beam of a giant 'fixed target experiment', as illustrated in figure 6.1. The particle beam interacts with the atmosphere of the earth (the target), and their secondary particles, e.g., muons, are detected by earth-based experiments, e.g., the CMS detector. Originally the CMS collaboration only intended to take cosmic ray data for commissioning the detector before the LHC start-up scheduled for Winter 2008. The detector, the software and the computing components were ready for the LHC start-up. But due to a severe incident in September 2008, the LHC schedule was delayed by a year. Therefore the CMS collaboration took advantage of the fully commissioned detector and turned its physics focus to the physics of cosmic rays.

Cosmic rays have a close connection with particle physics. Many particles commonly known in particle physics, e.g., positron, muon, pion and kaon, were first discovered in cosmic ray experiments. The ultra-high energy cosmic rays observed in air shower experiments can have energies of over 100 EeV, corresponding to center-of-mass energies of above 400 TeV, much higher than what the LHC can provide. Even at lower energies, the measurements are complementary to that investigated by accelerator experiments. This is because the small-angle forward energy flow (high-η) is lost in the beam pipe, whereas those forward particles dominate in cosmic ray experiments because of the fixed target geometry.

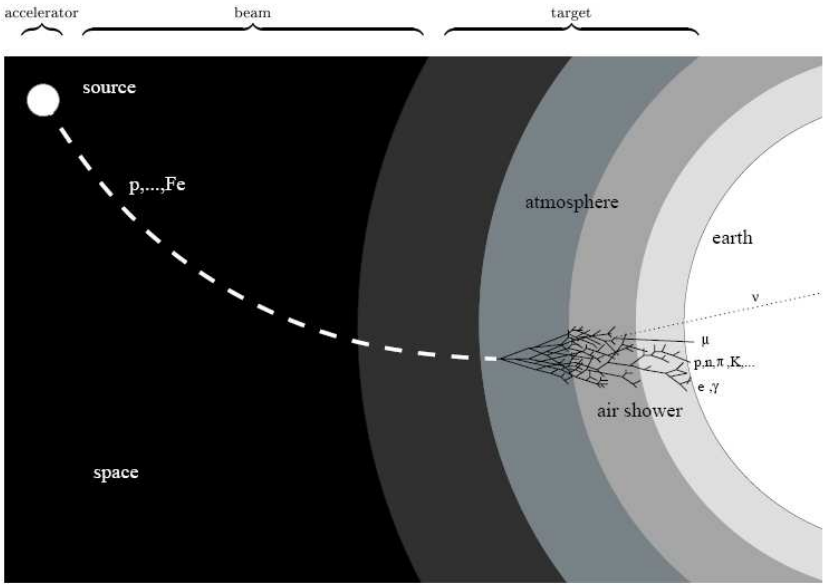

Figure 6.1. Schematic view of the cosmic 'fixed target experiment'.

6.2 Cosmic Runs in CMS

The CMS detector is not short for, and is not designed as, a cosmic muon spectrometer. Cosmic rays are only used as a source of charged particles for commissioning and calibration, and are treated as a source of background in LHC physics analyses. The CMS detector is placed about 90 meters underground and the amount of material shielding the CMS detector changes across the detector volume, thus complicating the connection between the detector and physics measurements on the earth's surface. The design of the CMS detector was optimized for measuring particles produced at the center of the detector rather than coming from outside. The timing of the trigger and the readout electronics of the detector assumes particles to be synchronized with the LHC beam. Without deliberate modification of the timing windows and synchronization of the trigger and readout electronic, most of the cosmic rays would only be partially recoded and reconstructed, as opposed to being tracked through the entire detector.

Therefore, the analysis of cosmic rays in the CMS collaboration is an activity which was only foreseen as a real data exercise in the time without LHC collisions. In July and August 2006, the CMS global data acquisition system was commissioned using cosmic rays at the earth's surface. This period of data taking is called the Magnetic Test and Cosmic Challenge (MTCC). The purpose of MTCC was to test and commission the magnet and map the magnetic field before lowering all the parts underground. It was also the first time that several detector subsystems, although only a small part of each, worked together and data were collected by the global data acquisition system.

In 2007 and 2008, all components of the CMS detector were lowered down and installed at their final position underground. In October and November 2008, the CMS detector collected roughly 376 million cosmic muon events with the full detector, in an effort called Cosmic Run At Four Tesla (CRAFT). The CRAFT data became a priceless source of data that greatly enhance the detector and software quality. The understanding of many aspects of the apparatus was achieved to a level which was estimated to be reachable only after accumulation of about 20 to 50 pb^{-1} of collision data at the LHC.

Among the 376 million cosmic muon events, there are roughly 3.7 million events with muons traversing the tracker volume, those are selected as tracking pointing (TP) skim. Because of the high precision provided by the tracker system, most analyses were conducted with this skimmed data. There are roughly 120 million events collected with stable conditions of the barrel DT muon system and the magnetic field, which are used for analyses that utilize standalone muons. The endcap muon system is not optimized to detect cosmic muons because of its position and acceptance. The description of the magnetic field and the detector alignment of the detector during CRAFT data taking has been greatly improved several times. A main challenge and effort of the cosmic analyses is to promptly incorporate those updates as well as to develop ad hoc tools for cosmic-specific features.

In this chapter, three cosmic muon analyses performed using CRAFT data are described. The first analysis deals with the *properties of high-energy muons* and their interactions with matter. Cosmic rays provide a natural source of high-energy muons and the results were used to validate various models implemented in the detector simulation software. Details of this study are followed in Section 6.3. The second analysis is the measurement of the ratio of positive and negative muons in cosmic rays (*muon charge ratio*) [49]. This ratio is determined by the meson production cross section in high-energy hadronic interactions involving air nuclei and hadrons like $\pi^{\pm}$ and $K^{\pm}$. The charge ratio is approximately constant, but at energies greater than a few hundred GeV, a growing influence of kaons is predicted and therefore an increase of the charge ratio is expected. Details of this muon charge ratio study are followed in Section 6.4. The third topic is the measurement of the rate of the absolute *cosmic muon flux* [50]. The rate of the muon flux is determined by the primary particles as well as the properties of the air nuclei, theoretical and experiment uncertainty both exist, and further measurements are desired to constraint the uncertainty. Details of the cosmic muon flux study are followed in Section 6.5.

6.3 Properties of High-Energy Muons

The precise measurement of high-energy muons in the TeV region is important for the study of a wide variety of physics processes at the LHC that have muons in the final state, e.g., W/Z, Higgs boson and high-mass bosons predicted by various theories. It is therefore important to precisely check the theoretical predictions and simulation of muon energy losses in the detector material in order to correctly reconstruct these high-energy muons. Muons lose energy in material due to two types of processes: ionization and radiation [42]. Radiative processes dominate in the high-energy range starting from a few hundred GeV. Radiative processes are characterized by small cross sections, hard spectra, large energy fluctuations and associated electromagnetic showers. A variety of theoretical calculations has been done for the radiative

processes [42]. However, there are still a few uncertainties in the estimation of the radiative energy losses of muons, which are due to the different theoretical predictions of the nuclear size correction [51].

The energy loss of high-energy muons up to 10 TeV has been measured in dedicated cosmic ray experiments [52, 53]. Reasonable agreement between data and theoretical predictions was reported. Energy losses of muons with pre-set energies up to 300 GeV were measured using various accelerator experiments [54, 55] and reasonable agreement was observed. However, preliminary results of the measurements of energy loss using 300 GeV muons suggested a few percent disagreement compared to Monte Carlo predictions [55]. Therefore improved measurements are desired to measure the nuclear form factor [51, 56, 57]. On the another hand, a good knowledge of the muon energy loss mechanisms is essential for the design of the detector and the reconstruction software. Muon detection and reconstruction relies on active tracking elements to pick up the correct muon measurements, which can be obscured by the presence of cascades of secondary particles. The understanding of the frequency of such interactions is crucial for the design of the detector and the reconstruction algorithms.

In this study, the energy loss of muon in the HCAL, the ECAL and the probability of generating electromagnetic showers in the DT system were tested against theoretical predictions and simulation models in order to improve understanding of the detector response.

6.3.1 Theory and Simulation of the Interaction of Muons with Matter

When muons pass through matter, they interact with the nucleus and the electrons via the Coulomb field of the molecules or ions of the material and transfer part of their energy to the material. When muons are decelerated or deflected, secondary photons may also be emitted via the bremsstrahlung mechanism.

The numerous ionization collisions with small energy transfers produce a localized trail of ionization that is used by the detector to track muons. These small energy transferring collisions correspond to energy losses about the most probable value of the Landau distribution of the energy loss spectrum. While the high-energy tail of the Landau distribution corresponds to stochastic collisions with large energy transfers.

The energy loss for muons can be parametrized as $-\frac{dE}{dx} = a(E) + b(E) \cdot E$, where $a(E)$ is the mean rate of energy loss by ionization described by the Bethe-Bloch equation [42]:

$$-\frac{dE}{dx} = Kz^2\frac{Z}{A}\frac{1}{\beta^2}[\frac{1}{2}\ln\frac{2m_ec^2\beta^2\gamma^2T_{max}}{I^2} - \beta^2 - \frac{\delta(\beta\gamma)}{2}], \tag{6.1}$$

where $T_{max} = \frac{2m_ec^2\beta^2\gamma^2}{1+2\gamma m_e/M+(m_e/M)^2}$ for particles with mass M and momentum $M\beta\gamma c$, $z = 1$ for muons, A is atomic mass of the absorber, K is $4\pi N_A r_e^2 m_e c^2$, I is the mean excitation energy, $b(E)$ is the sum of all contributions from direct e^+e^- pair production, bremsstrahlung, and nuclear interactions. At high energy, $b(E)$ is nearly constant.

The GEANT4 Simulation Toolkit [48] is using various models and different mechanisms used to simulate muon-detector interactions. The energy loss processes are simulated by two types of methods: continuous and discrete processes. Below a certain energy threshold the energy loss is continuous and above the threshold the explicit production of secondary particles - photons, electrons and positrons is included.

6.3.2 Energy Loss Measurements

The energy loss of muons in the CMS detector can be measured in different ways. The calorimeters (ECAL and HCAL) can directly measure the energy deposited by muons. It is also possible to check the momentum of a track stub before a particle passes through a piece of material and another track stub from the same particle after the particle passes through a material. The momenta estimated by the two independent measurements should be different, and their energy difference corresponds to the energy loss in the piece of material. However the resolution of the momen-

tum measurement is proportional to $p_T \oplus b \cdot p_T^2$, as discussed in Chapter 4, which makes the momentum difference very inaccurate compared with the uncertainty in the calorimeter measurements which can be expressed as a function of the deposited energy in the calorimeter $\frac{\sigma(E)}{E} = \frac{a}{E} \oplus \frac{b}{\sqrt{E}} \oplus c$ as mentioned in Chapter 3. Therefore, the ECAL and HCAL are used for the energy loss study, while the muon system is used to study electromagnetic showers.

Energy Loss in the HCAL

The study of the energy loss in the HCAL starts from the TP skim since cosmic muons that go though the tracker system must also go though the hadron and electromagnetic calorimeters. The energy deposit in the calorimeters can thus be checked against the momentum of the muon tracks.

To measure the energy loss in the HCAL, the following selections were made:

- Only HCAL non-zero suppressed runs were selected to ensure that HCAL worked properly.
- The number of reconstructed hits in the HCAL barrel and endcap was greater than 5000.
- the tracker track was chosen to lie within the central part of a certain ϕ tower (80%) ($\Delta\phi/(\Delta\phi_{\text{tower}}/2) < 0.87266$).
- Muons pass through the HCAL tower labeled with `iphi` $= -64$ or ± 13, i.e., HCAL towers located in certain narrow ϕ region, were not used due to bad readout.

The positions of the states at the HCAL Barrel (HB) outer surface and inner surface must belong to the same ϕ-plane in the HCAL barrel since all cells in one ϕ HB plane are readout with a single hybrid photo-diode (HPD). The ID of the crossed HCAL tower must have η-id less or equal than 14 to avoid problems due to the HCAL barrel-

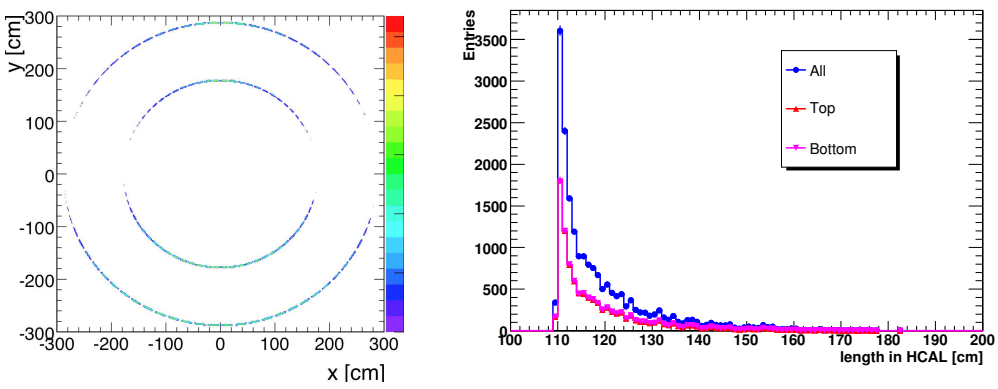

(a) (b)

Figure 6.2. (a) The x-y distribution of the propagated states on the inner and outer, top and bottom, HCAL surfaces. (b) The distance between the two propagated states on the inner and outer HCAL surfaces.

endcap overlap geometry. The measurement of values for dE/dx vs. p_μ are extracted as below.

- dE is the HCAL readout of the crossed HB tower as well as the ± 1 ϕ-tower and ± 2 η-towers. The muon energy is mainly deposited on the tower it goes through, but it is also possible that a small fraction of the energy is deposited in the nearby tower. The uncertainties with dE is from the intrinsic HCAL readout, which approximately is a function of E as $\frac{110\%}{E} + 10\%$.

- dx is extracted by the straight-line distance of the two propagated states, the difference between this direct distance and the real helix path is less than 1% even for low-energy muons. The difference between the cylinder and real HCAL surface is also small.

- p_μ is the energy of the propagated state at the entry position. The uncertainty of the p_μ can be extracted from the intrinsic uncertainty on $\sigma(\frac{1}{p})$ of the trajectory state which depends on the quality of the global track fitting.

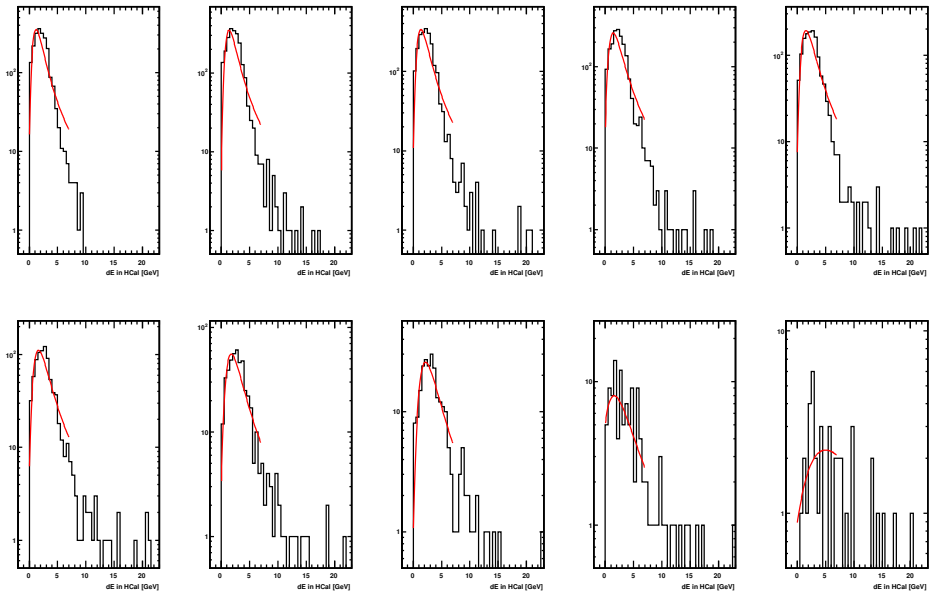

Figure 6.3. dE distribution in each p-bin for HCAL.

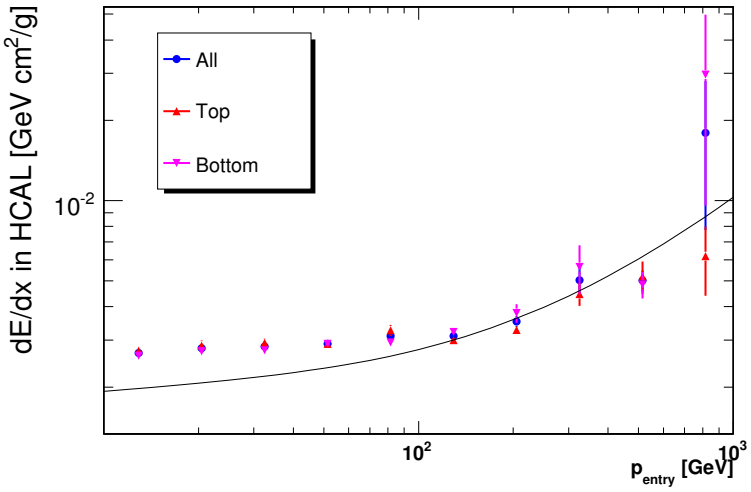

Figure 6.4. dE/dx vs. p_μ using top (upward triangles), bottom (downward triangles), and all (solid circles) parts of the HCAL compared with theoretical value. Only statistics error is presented.

The p-spectrum is divided into ten bins of about equal size on a logarithmic scale. For each p-bin, the distribution of the energy deposit can be described by a Landau distribution convoluted with Gaussian. The dE/dx is then converted to the stopping power by dividing it with the density of the zinc/copper mixture in HCAL.

As figure 6.4 shows, the measured stopping power is generally in agreement with the theoretical curve. The measurements in the low-p region are higher than the theoretical curve because of the read-out cut off in the HCAL. The measurements of the high-p region are lower than the theoretical curve because part of the energy loss for high energy muons could not be detected by the HCAL since muons are not absorbed within the HCAL volume. The HCAL was optimized to detect hadrons like pions, not for MIP signals. The agreement between the measurements and the theoretical curve is already pretty good given these facts.

Energy Loss in the ECAL

Similarly as in the HCAL, the energy loss in the ECAL can be measured by the ECAL readout. For the ECAL energy loss study, the following selections are applied:

- the tracker track must satisfy $|d_0| < 100$ cm, $d_z < 100$ cm,
- the angle between the muon track and the crystal must be less than 0.6 rad,

in order to require the muon to go through the ECAL volume.

The items entering the stopping power measurement are calculated as follows:

- dE is read out of the ECAL super clusters (with a correction factor 0.97 applied, which is estimated from MC). The ECAL super clusters within $\Delta R < 0.1$ region around the muon extrapolated position were picked.
- dx is extracted by the straight-line distance of the two propagated states, similar as for HCAL.
- p_μ is the momentum of the extrapolated state at the entry position.

As figure 6.5 and 6.6 show, the measured stopping power agrees with the theoretical prediction. The measurements at high-p region are lower than the theoretical curve because part of the energy loss for high energy muon could not be detected by the ECAL. Muons, unlike electrons, are not absorbed within the ECAL volume. Also the fitting has lower quality because of the low statistics.

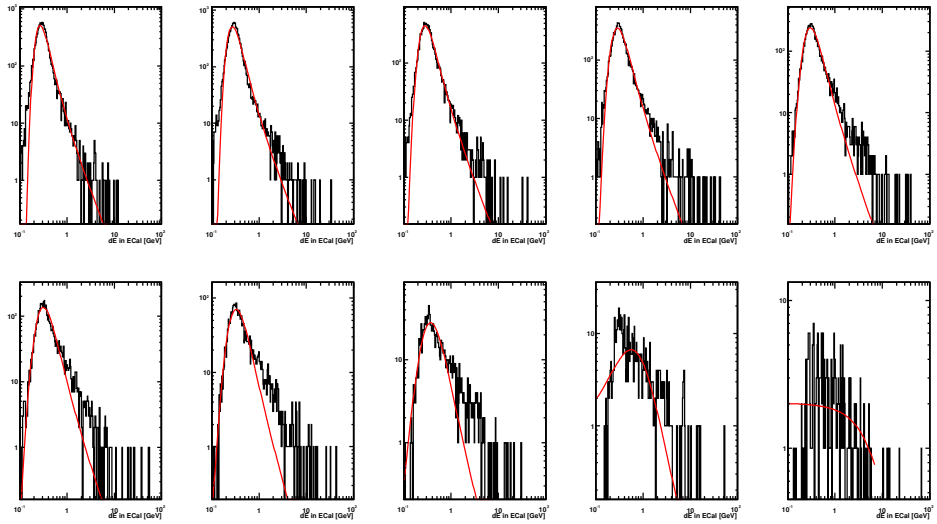

Figure 6.5. dE distribution in each p-bin for the ECAL.

6.3.3 Electromagnetic Showers in the Muon System

Electromagnetic showers in the muon chambers are signals of catastrophic energy loss of muons, which means a great fraction of the muon energy is lost in a small region. When catastrophic energy loss happens, many secondary particles are generated in a muon chamber, which makes it difficult to pick up the correct hits during muon reconstruction. Also, catastrophic energy loss makes the muon energy change significantly, and the energy loss model implemented in the muon reconstruction will no longer be suitable. Hence the understanding of how often electromagnetic showers happen is important to improve the performance of muon reconstruction. Moreover

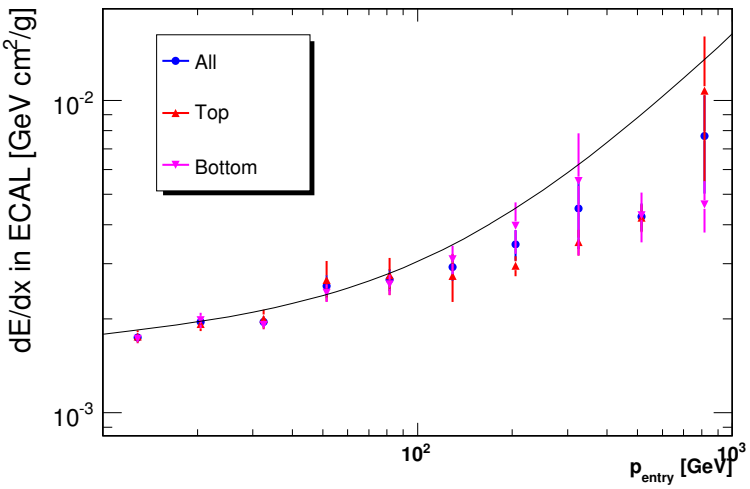

Figure 6.6. dE/dx vs. p_μ using top (upward triangles), bottom (downward triangles), and all (solid circles) parts of the ECAL compared with theoretical value.

it allows validation of the physics models implemented in the detector simulation by comparison with data.

Electromagnetic showers have the signature of high hit multiplicity in one layer or chamber of the muon system. There are also several processes which can mimic the signature in cosmic ray events. The first kind is extensive air showers, in which many cosmic muons are generated in the air and pass through the CMS in similar direction. The second kind is air showers of cosmic muons just outside the detector. In this case the layers in the upper hemisphere of the detector will have higher hit multiplicities. Therefore the probability of shower generation in this layer are not estimated. It is also possible that some parts of the detector have noise, therefore only the chambers that could be reached by a muon are checked.

In order to identify an electromagnetic shower in the muon chambers, the basic quantities to check are the number of hits and segments per layer. As shown in 6.7, the distributions of the number of hits and segments for data and MC agree very well. Two new quantities are introduced in order to better identify showers:

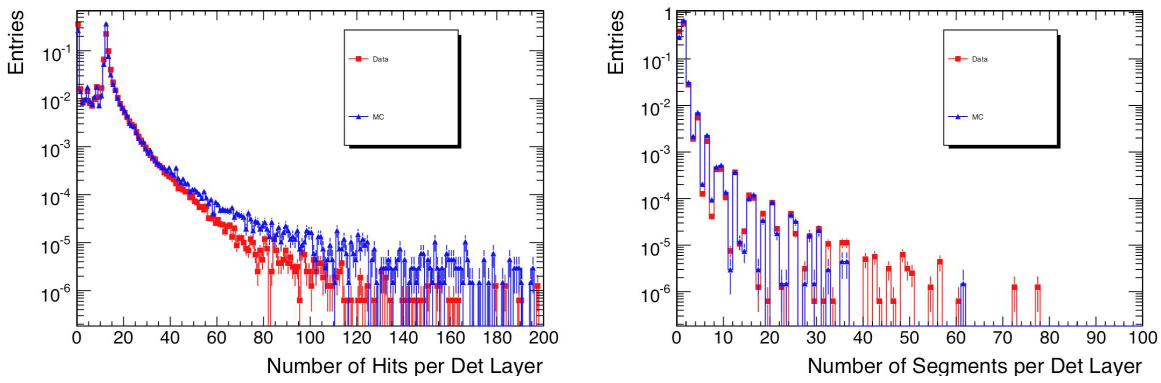

(a) (b)

Figure 6.7. (a) Distribution of number of hits per layer. (b) number of segments per layer. The squares present the distribution of data and the triangles present the distribution of MC.

- *shower size*: the maximum distance between two hits in a hit cluster,
- *number of uncorrelated hits*: the number of all hits minus the number of DT sublayers of the layer. This number was chosen instead of the number of segments because when there are too many hits in one chamber, it is likely that many unphysical segments are built.

Electromagnetic showers are identified in the DT system by the following procedure. Starting from reconstructed tracker tracks, which do not contain any muon information and are not 'spoiled' by the presence of electromagnetic showers, the tracks are extrapolated to the muon stations on both sides. From the eight intersection points, DT hits in the six or nine closest DT chambers are counted. A shower is determined if both the criteria are reached in a layer: there are at least 40 uncorrelated hits and the shower size is greater than 20 cm. The distribution of the two variables is shown in figure 6.8.

The probability of finding electromagnetic showers in the muon system as a function of the muon momentum is shown in figure 6.9. Good agreement up to about

200 GeV is found in all muon stations, while the showering probability for data declined in the high-momentum region. This could be due to the finite momentum resolution of muons resulting in a smearing between bins are different. Since the probability measured here is a very small quantity, it could be very sensitive to this smearing. Further investigation will be helpful when the detector response is better understood in future.

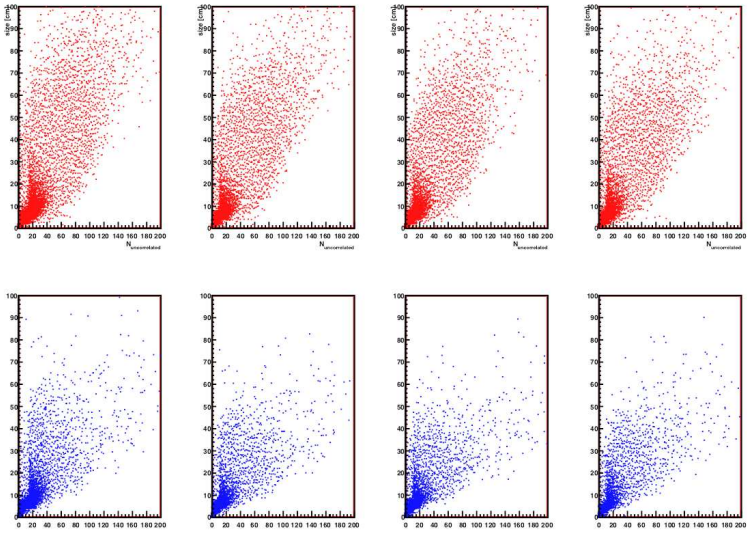

Figure 6.8. Number of uncorrelated hits vs. the shower size in the upper four layers for data (up plots) and MC (bottom) plots.

6.3.4 Summary

The energy loss of muons in the HCAL, ECAL, and the muon system are measured, and good agreement with existing models are found up to a few hundred GeV. However, there are still some results that can not be fully quantified. The precision is limited by the track resolution and our current understanding of the detector.

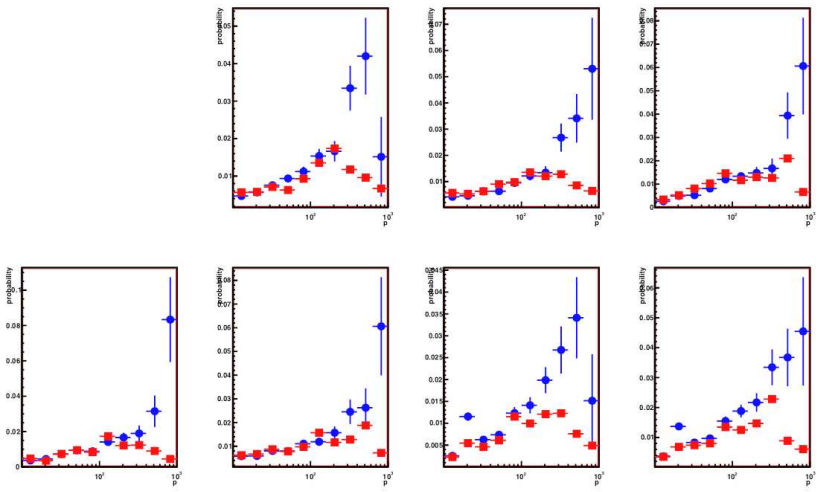

Figure 6.9. Showering probability for data/MC in three top and four bottom DT layers.

6.4 Charge Ratio

The primary cosmic rays are composed of heavy stable charged particles, mainly positively charged protons and helium nuclei. Therefore there are more positive than negative pions and kaons in the resulting hadronic showers at the top of the earth atmosphere. In a compilation of measurements, the charge ratio of cosmic muons at sea level was determined to be approximately constant at 1.27 up to a few hundred GeV [58].

As energy increases, the fraction of muons from kaon decays increases because the longer-lived pions have become more likely to interact before decaying than the shorter-lived kaons. Consequently, kaon decays begin to make a larger contribution to the muon charge ratio. Since the muon charge ratio from kaon decays is greater than that from pion decays, the overall charge ratio is expected to increase. Results from the MINOS experiment indicate a clear rise in the charge ratio in the energy range $0.3 - 1.0$ TeV which is consistent with the predictions [59]. With measurements of

the muon charge ratio using the CMS detector, models of the interactions of cosmic rays in the atmosphere can be further improved.

6.4.1 Measurement Components

The ultimate physics measurement is the ratio of positive muons to negative muons, as a function of the muon momentum at the surface of the earth. The initial measurement is performed at the center of the detector where the best measurements on the muon track parameters are available.

Inside the detector, the uncorrected (*raw*) charge ratio is measured. This is the ratio of the number of positive and negative muons, divided into momentum bins. Muons are reconstructed using the specialized cosmic reconstruction algorithms described in [60]. The standard LHC-style reconstruction is not optimal for this analysis because it assumes muons are emanating from the interaction point, as described in Chapter 4. For cosmic measurements the magnetic field breaks the symmetry of the detector. Any asymmetry about the vertical axis can induce a bias in the charge ratio measurement.

Data-driven methods were developed for the analysis, utilizing *split tracks*, which are cosmic muons for which the tracker trajectory is split into two (above and below the PCA). These cosmic muons are a valuable tool for two reasons. Firstly, they are objects with the largest similarity to LHC-like dimuons available. Secondly, at the point of closest approach (PCA), they provide two independent measurements of the same quantities. Since the vast majority of cosmic muons are moving downwards ($p_y < 0$) in the detector, the two muon legs are referred as the *top* and *bottom* muon legs in the following.

In this analysis, global muons are utilized and are required to have hits in the Tracker Outer Barrel (TOB) and central muon (DT) systems. The tracker and muon endcap systems were explicitly excluded. The amount of statistics gathered in the

endcap region would not be sufficient and the quality would not match that of the central detector.

The charge (q) and the transverse momentum (p_T) of the top and bottom legs are combined by averaging the curvature:

$$\frac{q_C}{p_{T,C}} = \frac{1}{2}\left(\frac{q_1}{p_{T,1}} + \frac{q_2}{p_{T,2}}\right) \tag{6.2}$$

where q_C and $p_{T,C}$ are the combined charge and transverse momentum at the point of closest approach, q_1 and q_2 are the charges of the top and bottom legs, respectively, and $p_{T,1}$ and $p_{T,2}$ are the transverse momenta of the top and bottom legs, respectively. The other track parameters - the azimuth angle ϕ_0, impact parameter d_0, cotangent of the polar angle $\cot\theta$ and z coordinate at the PCA (z_0) are combined in the same fashion.

Since the top and bottom legs are independent measures of the same quantity, the resolution distribution for the combination in equation 6.2 can be derived from the half-difference distribution of the two quantities:

$$d_C = \frac{1}{2}\left(\frac{q_1}{p_{T,1}} - \frac{q_2}{p_{T,2}}\right) \tag{6.3}$$

This provides a data-driven handle on the resolutions of the curvature and other track parameter measurements.

6.4.2 Event Selection

Pairs of independently reconstructed global muon tracks of the same muon are used in this study. With these split pairs, the dependencies of the momentum resolution – curvature, $\cot(\theta)$, and charge confusion – on selected quality variables are studied.

Muon Selection

This analysis relies on *pairs* of muons, so at least two independent global muons are required. At least one muon is required in the upper half of the CMS and at least one muon is required in the lower half of the CMS. If a pair of global muons share a tracker track (which may still happen even in track-splitting) the muon is removed from consideration because the momentum measurement is dominated by the tracker making the half-difference in curvature not representative of the detector resolution.

Also the average p_T of the pair of muons is required to be at least 10 GeV. This is because it takes at least 10 GeV for a muon to traverse the entire CMS volume.

Additional quality cuts on global muon pairs are needed to ensure the same muon quality for upper and lower legs. The following selection cuts are determined and optimized based on selection efficiency and resolution:

1. at least 20 DT hits and 5 TOB hits for each leg to ensure the quality of the global tracks. The first cut is roughly 80% efficient, and the second is almost 95% efficient.

2. at least 3 DT Super Layer (SL) 2 hits for each leg to ensure good measurement of $\cot(\theta)$ and thus the total muon momentum. This requirement is roughly 95% efficient.

3. both tracks should have a $\chi^2 < 1500$. The cut is roughly 99% efficient.

4. the difference of the track angle in the r-z plane $\Delta \cot \theta$ should be less than 0.2 to ensure the top and bottom trajectories originate from the same muon The $\Delta \cot \theta$ cut is over 99% efficient.

Trigger Selection

Events are required to be selected by the `L1_SingleMuonOpen` trigger path. Triggers stemming from the CSC trigger are not considered. In order to ensure that

the cosmic muon studied has generated the trigger, a topological match between the trigger object and the reconstructed muon are required. To determine whether or not a muon trigger has a match, the standalone muon track that is a constituent of the global muon is propagated to MB2 of the DT system, where the trigger reports muon track parameters. Since the muon must be propagated to a specific surface, the MB2 of the DTs is modeled as a cylinder with a 5 m radius from the center of the detector. $\mid \Delta\phi \mid < 0.2$ between the recorded position of the trigger and the position of the propagated standalone muon at MB2 is required to determine a match. The $\Delta\phi$ cut is placed around the core of the distribution. No topological bias (preference of top over bottom or positive over negative) in the trigger matching requirement is found.

Multi-Muon Events

The only real background to the measurement are multi-muon events. Multiple muons can be present inside the CMS detector during a single trigger, as part of a muon shower. If these events were included, top and bottom track fits from different muons could be paired together under the assumption that they are the same muon. The measured trajectory parameters will be practically random and will dilute the power of the data-driven method.

In order to exercise a complete clean-up of multi muon events, it is required that there should be exactly two standalone muons reconstructed in the event with one of them being in the upper half of the CMS detector and the other in the lower half. The rejection of multi-muon events by requiring no additional pairs or standalone muons are reconstructed is 100% efficient in the muons collection after all previous requirements are applied.

Shaft Model

For unfolding the charge ratio to the earth's surface, the CMS shafts create a non-trivial oddity. The materials penetrated by cosmic muons are modeled according to the molasse map of the CERN Point 5. The map includes one main shaft and two small access shafts. The rest are modeled as rock and earth molasse. The energy losses differ largely depending on whether the muons go through the CMS shafts. The energy loss for muons that traveled through the shafts is usually less than 10 GeV, but for muons that did not travel through the shaft, the energy loss is about 30 GeV or more. It is also observed that there are more muons with entry point at $z^{8m} \sim 300$ cm and $\phi^{8m} \sim \pi/2$ in data than in MC. This is because the plug cover on top of the CMS shaft was not at its position during some CRAFT runs, and this situation is not modeled in the MC. The model also assumes that all shafts are empty, while there are some stairways and equipment inside. Therefore, muons that entered the CMS cavern through the access shafts are deselected in order to avoid systematic effects at low energies due to the different total energy loss of this set of muons. They are removed as follows. Once muon pairs have been selected, the combined trajectory is propagated to a cylinder drawn around the CMS detector with a radius of 8 m. For each propagated muon, the entry point on the earth's surface, which is assumed to be on a flat plane $y^{Earth} = 91.12$ m above the CMS center, was estimated from the position and direction when entering the CMS detector:

$$\begin{aligned} x^{Earth} &= x^{8m} + \frac{p_x^{8m}}{p_y^{8m}} \left(y^{Earth} - y^{8m} \right), \\ z^{Earth} &= z^{8m} + \frac{p_z^{8m}}{p_y^{8m}} \left(y^{Earth} - y^{8m} \right). \end{aligned} \tag{6.4}$$

Muon tracks in the circles given in equation 6.5 are categorized as shaft muons and are not used in this analysis. The efficiency of this definition is shown in figure 6.10, as a function of momentum. While this selection drops roughly 50% of the low

momentum muons, the region of interest for this measurement is around or above 100 GeV, where the efficiency is quite high (80% or better).

$$\sqrt{\left(x^{Earth}\right)^2 + \left(z^{Earth} + 30\right)^2} < 30 \text{ m},$$
$$\sqrt{\left(x^{Earth} - 32\right)^2 + \left(z^{Earth} - 20\right)^2} < 5 \text{ m}. \tag{6.5}$$

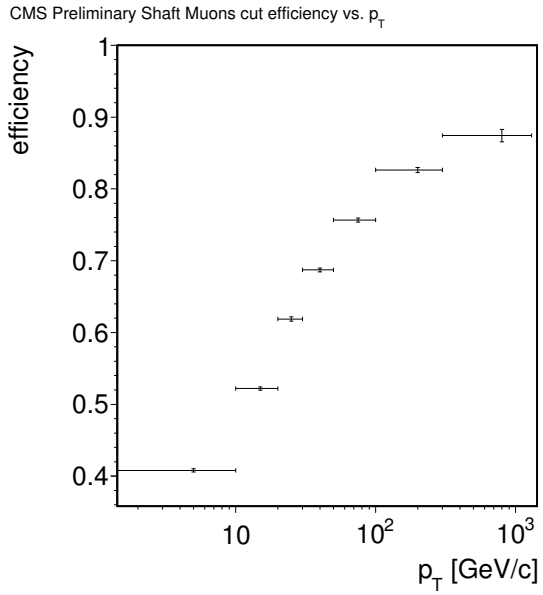

Figure 6.10. Efficiency for removing shaft muons as a function of p_T .

Summary of Event Selections

An unbiased selection of events were developed for the charge ratio analysis.

Event counts after sequential application of selection requirements are summarized in table 6.1. There are roughly 3.7 million events with muons that travel through the tracker volume. Good run selection roughly halves the number of available events. Requiring that there are no endcap hits used in the muon fit removed one third of

the remaining events. Another significant reduction (lose 3/4 of the events) happens when requiring that the global muons used in the analysis are not matched to the same tracker track. The tracker muons are not always split top vs bottom in the LHC mode of navigation in the fit. The final significant reduction (lose 1/3 events) happens when removing shaft muons. As discussed in the previous section, this mostly affects the low-p_T region of the measurement. The systematic effects due to selection requirements on the charge ratio are studied separately and are reported in Section 6.4.4.

6.4.3 Unfolding

The desired measurement on the surface of the earth is linked to the observables at the center of the detector as follows.

The first step is the transfer of muons from the earth's surface to the surface of the CMS detector. This is considered as an independent transfer because the material that muons have to traverse before reaching the CMS detector completely differs from that within the CMS detector. The second step is then the transfer of muons from the CMS surface to the PCA. Denoting the vector of true charge-dependent momenta at the surface as p_i^{Earth}, the vector of true momenta at the CMS surface as p_i^{8m} and the vector of true momenta at the center of the detector as p_i^{PCA}, the transformation from the surface of the earth to the surface of the detector can be performed with a transfer matrix T_{ij}:

$$p_i^{8m} = \sum_j T_{ij} p_j^{Earth}. \tag{6.6}$$

The same procedure happens when moving from the CMS surface to the CMS PCA, via a different transfer matrix D_{ij}:

$$p_i^{PCA} = \sum_j D_{ij} p_j^{8m} \tag{6.7}$$

The detector measures two key components of the momentum, the charge dependent curvature $\mathcal{C} = q/p_T$ and the cotangent of the polar angle $\cot\theta$. The correlation

Cut	Number of Events	Efficiency (%)	MC Efficiency (%)
candidate events in all runs	3696897	N/A	N/A
good runs	1674437	45.29	N/A
exactly 2 standalone	1580248	94.37	N/A
initial pairs	1580248	100.00	100.00
cut CSC	1436781	83.02	90.92
cut TEC	1097474	72.05	76.38
number of DT hits$\geq$ 20	835501	79.37	76.13
number of DT segments ≥ 3	773982	96.23	92.64
number of TOB hits ≥ 5	698821	91.83	90.29
deltaCotTheta < 0.2	697686	99.80	99.84
max $\chi^2 < 1500$	669450	96.85	95.95
not same track	160582	26.77	23.99
cut multi pairs / event	160582	100.0	100.0
remove shaft	111013	69.13	58.08
require matched trigger	109861	98.96	99.25

Table 6.1
Event counts after sequential application of selection requirements. The requirement that there are exactly two standalone muons in the event removes events where there are multiple pairs at the end of all selection, hence the event count equals the pair count thereafter.

between these variables is very small, when compared to correlations between transverse variables ($\mathcal{C}, \phi_0$, impact parameter) or between rz variables ($\cot\theta, z_0$). These two measurements can be taken as independent. This is relevant because the measurement of the curvature directly affects the determination of the charge (due to curvature mis-measurement the charge can be flipped), and the measurement of $\cot\theta$ is decoupled from it. Resolution effects leading to a curvature mis-measurement can flip the charge of a particle; resolution effects due to the measurement of $\cot\theta$ cannot. Furthermore, since curvature resolution effects depend on the true curvature, but not on $\cot\theta$, the unfolding of charge mis-assignment should be done as a function of curvature (or p_T), as opposed to full measured momentum p.

The measured $p_{T,i}$ and true $p_{T,i}^{PCA}$ charge dependent transverse momentum spectra are connected by the resolution matrix R_{ij}:

$$p_{T,i} = \sum_j R_{ij} p_{T,j}^{PCA} \tag{6.8}$$

The momentum and transverse momentum are connected by $\cot\theta$:

$$p_T = \frac{p}{\sqrt{1+\cot^2\theta}} \tag{6.9}$$

One can define a matrix C_{ij} which connects the true momentum p_i^{PCA} to the transverse momentum, but only taking into account the uncertainty on $\cot\theta$:

$$p_{T,i}^{PCA} = \sum_j C_{ij} p_j^{PCA} \tag{6.10}$$

Then the full transformation from the earth's surface to the measured transverse momentum in the center of the detector can be presented as:

$$p_{T,i} = \sum_{j,k,l,m} R_{ij} C_{jk} D_{kl} T_{lm} p_m^{Earth} \tag{6.11}$$

The four matrices need to be inverted in order to unfold (transfer) to the surface:

$$p_i^{Earth} = \sum_{j,k,l,m} T_{ij}^{-1} D_{jk}^{-1} C_{kl}^{-1} R_{lm}^{-1} p_{T,m} \tag{6.12}$$

This process can be simplified by replacing the three-step transfer $p_T \leftrightarrow p_T^{PCA} \leftrightarrow p^{PCA} \leftrightarrow p^{8m}$ by a single transfer of muons from the CMS surface to the measured transverse momentum $p_T \leftrightarrow p^{8m}$. This transformation is carried by the matrix H_{ij}:

$$p_{T,i} = \sum_j H_{ij} p_j^{8m} \tag{6.13}$$

and accordingly, the more correct transfer to the surface is given by the inversion of two matrices:

$$p_i^{Earth} = \sum_{j,k} T_{ij}^{-1} H_{jk}^{-1} p_{T,k} \tag{6.14}$$

It was concluded that the most robust method for this conversion is the matrix inversion method after a lengthy review of unfolding methods, as long as that the momentum bins are defined so that the spill-over from a single bin is small before inverting ($< 30\%$).

Matrix Inversion Unfolding Method

The matrix inversion method works as follows. If v_i is defined as the vector of event counts in a histogram based on the *true* observables in a dataset and u_i the vector of *measured* observables, and define the migration matrix M, then the bin content of the migration matrix M_{ij} corresponds to the number of times that a measured observable is observed in bin i, when the true observable belonged to bin j. By construction, the row-wise and column-wise sums of the migration matrix correspond to the true and measured vectors, respectively:

$$\sum_j M_{ij} = u_i \qquad \sum_i M_{ij} = v_j \tag{6.15}$$

Let R be the response matrix which describes the transfer from true to measured vectors:

$$u_i = \sum_j R_{ij} v_j \tag{6.16}$$

The response matrix can then be derived from the migration matrix:

$$u_i = \sum_j M_{ij} = \sum_j M_{ij} \frac{v_j}{\sum_k M_{kj}} = \sum_j \left[\frac{M_{ij}}{\sum_k M_{kj}} \right] v_j \equiv \sum_j R_{ij} v_j \tag{6.17}$$

$$R_{ij} = \frac{M_{ij}}{\sum_k M_{kj}} \tag{6.18}$$

Notice that the response matrix is the column-wise normalization of the migration matrix. Unfolding via matrix inversion is then the operation:

$$v_i = \sum_{j,k} R_{ik}^{-1} R_{kj} v_j \tag{6.19}$$

Finally, the uncertainties on the unfolded quantities are computed from [61]:

$$\sigma_i = \sqrt{\sum_j \left(R_{ij}^{-1}\right)^2 u_j} \tag{6.20}$$

Transfer with Losses

The transfers from the earth's surface ($Earth$) to the surface of CMS ($8m$) and from $8m$ to the center of CMS are with losses. The number of muons observed at the $8m$ is smaller than the the number of muons on the earth's surface N_{Earth}. Denoting u_i as the vector of $Earth$ muon counts in momentum bins, and v_i as the corresponding $8m$ vector at the CMS surface, for muons that survive the transfer, a transfer matrix that connects the two of them is

$$v_i = \sum_j T_{ij} u_j. \tag{6.21}$$

For this transfer matrix to be properly defined, the following quantities are needed:

- for every muon that survived the transfer, the $Earth$ and $8m$ momenta, p^{Earth} and p^{8m} ;
- the rate of muons per p^{8m} bin i, $R_{8m,i}$;
- the rate of muons per p^{Earth} bin j, $R_{Earth,j}$.

From the muons that made the transfer, the migration matrix M_{ij} can always be constructed, defined as the number of muons with p^{Earth} in bin j and p^{8m} in bin i.

The transfer matrix T_{ij} needs to simultaneously account for rate loss and momentum migration. This matrix is basically the probability that an event starting in bin j at $Earth$ will end in bin i at the CMS $8m$. In other words, T_{ij} is the rate at which events from true bin j survive and make it into bin i, where they contribute to the $R_{8m,i}$ rate by the amount $R_{8m,ij}$,

$$T_{ij} = \frac{R_{8m,ij}}{R_{Earth,j}} \tag{6.22}$$

The rate $R_{8m,ij}$ can be computed from the matrix element M_{ij}, the total number of events observed in bin i at $8m$, v_i, and the rate of events in the same bin i,

$$R_{8m,ij} = \frac{M_{ij}}{v_i}\ R_{8m,i} \tag{6.23}$$

In other words, $R_{8m,ij}$ is the differential contribution to $R_{8m,i}$ specifically coming from the $Earth$ bin j. Recalling that

$$v_i = \sum_j M_{ij}\ , \tag{6.24}$$

then the transfer matrix T_{ij} is

$$T_{ij} = \frac{M_{ij}}{\sum_k M_{ik}}\ \frac{R_{8m,i}}{R_{Earth,j}} \tag{6.25}$$

which is a row-normalized matrix with scale factors that account for rate losses.

From the CMS Detector to the Earth Surface

The differential spectrum on the CMS surface is transferred to the spectrum on the earth's surface by an independent migration matrix in order to be compared with theoretical predictions and previous results. The migration matrix presents the propagation through the material between the CMS detector and the earth's surface, taking the energy loss in molasse over the CMS detector into account. As described in Section 6.4.2 muons that enter the CMS shafts are deselected to help diagonalizing the migration matrix. This matrix, denoted as R, is calculated with dedicated simulation

samples using the cosmic muon generation package [47] integrated in CMSSW. A matrix element R_{ij} presents the probability of measuring a momentum p_i^{8m} at the CMS surface, given a momentum p_j^{Earth} at the earth's surface. The charge q is considered constant in the propagation between the two surfaces. To account for the differences between MC and data, each MC event is weighted depending on the parameters η_{dir}, ϕ_{dir}, z_{pos}, ϕ_{pos}. Comparing the η and ϕ distributions of the muon momentum at the CMS surface, and the z and ϕ coordinates of the entry point, as shown in figure 6.11, the weights are defined from these normalized distributions:

$$w_{event} = \frac{P(\eta_{dir}^{data})}{P(\eta_{dir}^{MC})} \frac{P(\phi_{dir}^{data})}{P(\phi_{dir}^{MC})} \frac{P(z_{pos}^{data})}{P(z_{pos}^{MC})} \frac{P(\phi_{pos}^{data})}{P(\phi_{pos}^{MC})} \tag{6.26}$$

Choice of Momentum Bins

The momentum bins should be chosen in such a way that the spill-over in any bin of the migration matrix is minimal, ideally below 30%. The starting points at the bin edges as defined at the PCA are the following:

$$p_T^{PCA} = (10, 20, 30, 50, 100, 300, \infty) \text{ GeV} \tag{6.27}$$

These values, together with the condition of minimal spill-over, constrain the values of the momentum bins at the CMS $8m$ surface, as following:

$$p^{8m} = (15, 25, 35, 55, 110, 310, \infty) \text{ GeV} \tag{6.28}$$

It results in a spill-over fraction of below 10% in all the momentum range, as can be seen in figure 6.12 (right). Figure 6.12 (left) shows the migration matrix that transforms p^{8m} to p_T^{PCA}. Notice that this matrix is mostly diagonal. The same procedure is followed to define the momentum bin edges at the earth's surface, as cosmic muons lose at least 30 GeV in the molasse before reaching CMS. In this case the optimal bin edges are:

$$p^{Earth} = (35, 60, 75, 100, 155, 360, \infty) \text{ GeV} \tag{6.29}$$

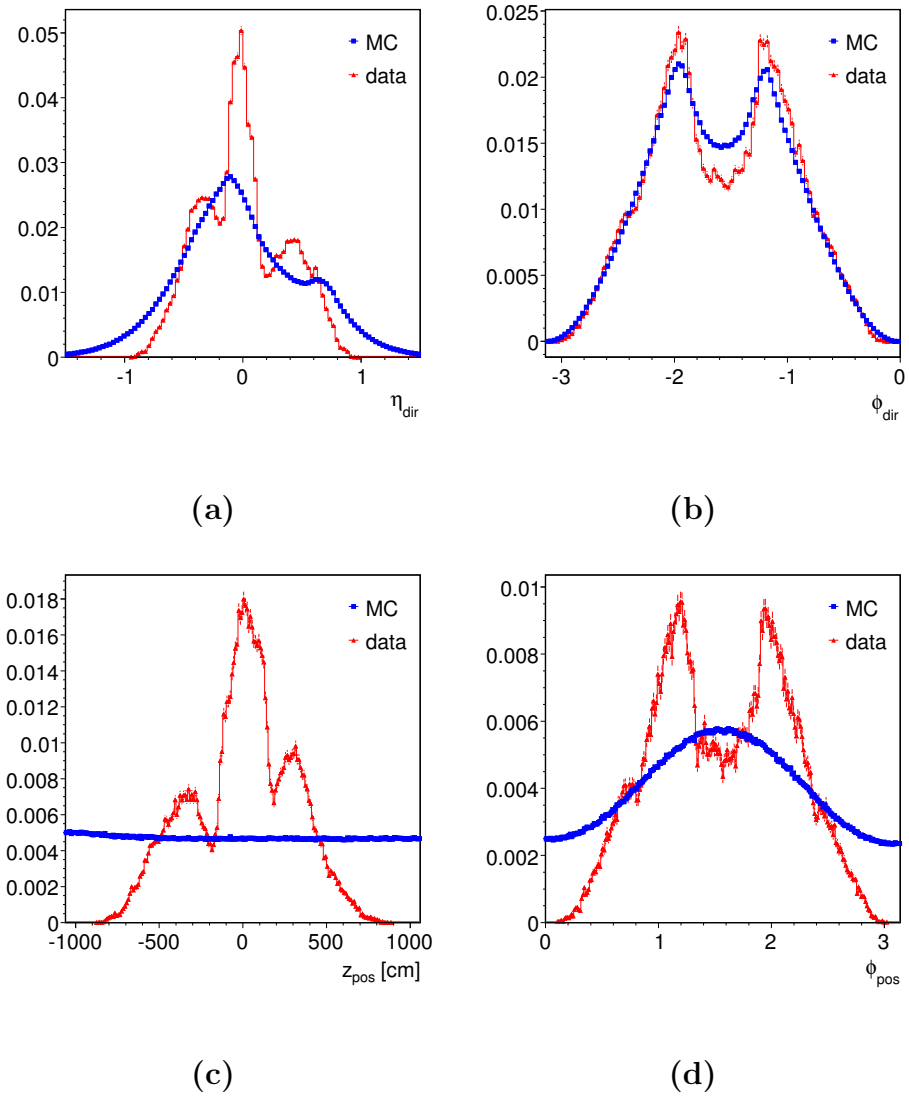

Figure 6.11. Data (solid red triangles) and MC (solid blue squares) comparison of the distributions of η_{dir} (a) and ϕ_{dir} (b) of the muon momentum,and z_{pos} (c) and ϕ_{pos} (d) of the muon position, at the CMS $8m$ surface.

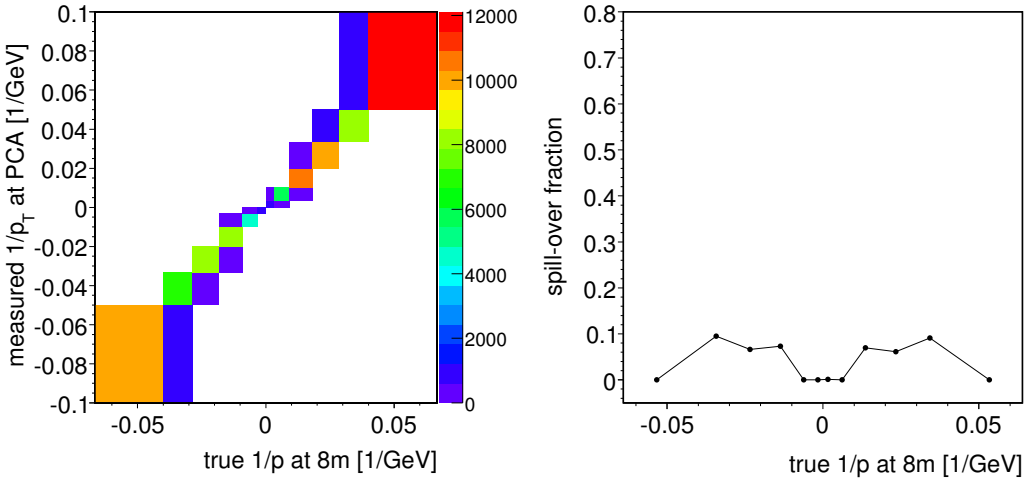

Figure 6.12. (Left) Migration matrix which transforms event counts in bins of true momentum at the CMS $8m$ surface to event counts in bins of measured transverse momentum at the CMS PCA. (Right) Off-diagonal spill-over by column.

With this binning most of the momentum spectrum has spill-over probability of below 30%, as shown in figure 6.13 (right). In figure 6.13 (left) one can see a clear linear correlation at high momentum (small curvature), while the energy loss fraction becomes noticeably larger for low momentum muons.

Muon Rates

Not all cosmic muons reaching the earth at CERN Point 5 make it all the way down to the center of the CMS detector. Energy losses in the molasse and inside the CMS detector, together with the limited cross section that the CMS is for cosmic muons, substantially reduce the number of muons that can be measured. The trigger and selection efficiencies further limit the sample. It is thus necessary to determine the muon rates at each step of the unfolding procedure:

- $R\left(p^{Earth}\right)$ is the muon rate at the earth's surface, in p^{Earth} bins;

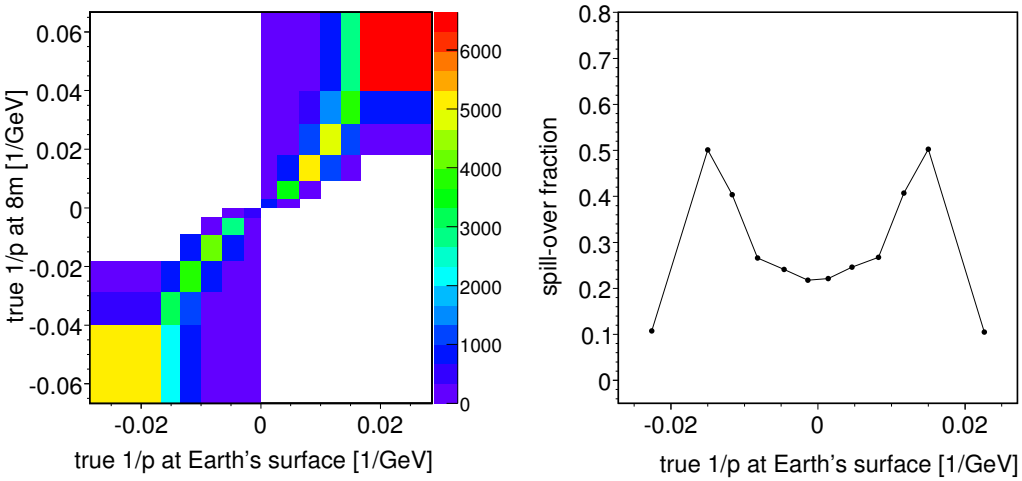

Figure 6.13. (Left) Migration matrix which transforms event counts in bins of true momentum at the earth's surface to event counts in bins of true momentum at the CMS $8m$ surface. (Right) Off-diagonal spill-over by column.

- $R\left(p^{8m}\right)$ is the muon rate at the CMS $8m$ surface, in p^{8m} bins;
- $R\left(p_T^{PCA}\right)$ is the muon rate at the CMS PCA, in p_T^{PCA} bins.

Calculating the rates is non-trivial because the ability of the CMS detector to capture cosmic muons must be estimated, which is possible with Monte Carlo samples only. In the first sample, cosmic muons are generated on a cylinder and two disks outside of the CMS at 8 m. The quantity of how many reconstructed muons (in events where there is a DT or RPC trigger) entering the TP skim is calculated by applying a filter requiring the `OR` of the following conditions: at least one tracker track reconstructed by three available tracker track reconstruction algorithms or at least one standalone muon that can propagate to the TP volume with radius 90 cm and width (z) of 130 cm. From there, selections are applied to MC in the same manner as in data. Based on the different numbers of muons $n(p)$ extracted from this Monte Carlo, the CRAFT data, and a dedicated Monte Carlo for the earth's surface, the muon rates are estimated in the following equations 6.30–6.32. The resulting rates are summarized in figure 6.14. The value $2.2 \cdot 10^8$ Hz in equation 6.30 is the rate used to generate cosmic muons at a circular plane on the earth's surface ($2.1 \cdot 10^6$ m^2)using numbers from [62]. The value $6.8 \cdot 10^4$ Hz in equation 6.31 is the rate obtained when cosmic muons are extrapolated to the CMS $8m$ surface [62].

$$R\left(p^{Earth}\right) = n^{MC}_{Earth \notin shaft}\left(p^{Earth}\right) \cdot \frac{N^{MC}_{Earth}}{N^{MC}_{Earth \notin shaft}} \cdot \frac{2.2 \cdot 10^8}{N^{MC}_{Earth}} \tag{6.30}$$

$$R\left(p^{8m}\right) = n^{MC}_{8m \notin shaft}\left(p^{8m}\right) \cdot \frac{N^{MC}_{8m}}{N^{MC}_{8m \notin shaft}} \cdot \frac{6.8 \cdot 10^4}{N^{MC}_{8m}} \tag{6.31}$$

$$R\left(p_T^{PCA}\right) = \frac{n^{data}_{selection}\left(p_T^{PCA}\right)}{n^{data}_{TP,reco}\left(p_T^{PCA}\right)} \cdot \frac{n^{MC}_{TP,reco}\left(p_T^{PCA}\right)}{n^{MC}_{8m \notin shaft}\left(p^{8m}\right)} \cdot R\left(p^{8m}\right) \tag{6.32}$$

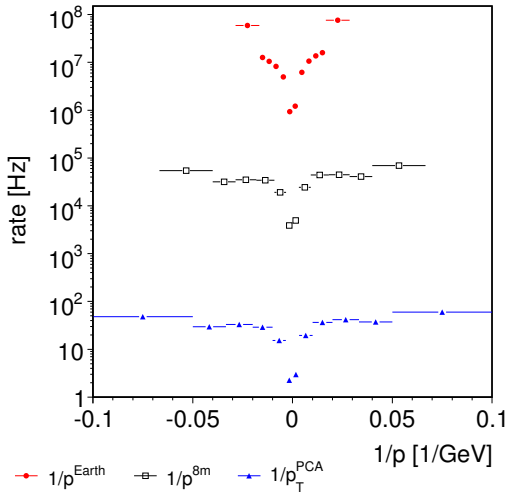

Figure 6.14. (Red solid circles) Muon rate at the earth's surface, normalized to $2.2 \cdot 10^8$ Hz, up to $\theta_{max} = 84^o$. (Black open squares) Muon rate at the CMS $8m$ surface, normalized to $6.8 \cdot 10^4$ Hz, up to $\theta_{max} = 84^o$. (Blue solid triangles) Muon rate at the CMS PCA.

6.4.4 Systematic Uncertainties

Systematic uncertainties for the charge ratio are evaluated in each p_T bin. The systematics are broken into *trigger*, *event selection*, *alignment*, *magnetic field* and *molasse model*.

In evaluating the systematics in a data-driven way, two samples stemming from two re-processings of the TP skim are used. For the selection and trigger systematics, "N-1" studies, as described in the selection section, are performed. This employs the best understanding of the magnetic field and alignment.

To evaluate the alignment and B-field systematics, an earlier re-processing of the data is also used as described in detail respectively.

The systematic uncertainty in the alignment is quite high in the high-p_T bin; this is because the compared alignment scenarios are very different from each other. The first alignment scenario was built without track-based alignment, but the second alignment scenario was the alignment scenario with updates on the tracker and DT Alignment Position Errors (APEs).

Trigger

To estimate the systematic bias induced by the trigger, a *tag-and-probe* technique is employed. There are four kinds of events when matching to the trigger: those where the upper leg matches to trigger, the lower leg matches, both legs match, and either leg matches. These are referred to as N(upper), N(lower), N(and) and N(or) respectively.

To minimize the bias, an "or"-type trigger is required. The charge bias is described in equation 6.33.

$$\xi_q = \frac{p(\text{or})_+}{p(\text{or})_-} \tag{6.33}$$

To find ξ_q in equation 6.33, the estimators are derived for the true probability that an event will fire the "or" trigger based on the observed N(upper), N(lower), N(and) and N(or). Since this is a tag-and-probe technique, the upper and lower

trigger probabilities are expected to be independent. An estimator is constructed for the probability of firing a trigger "A" given that another independent trigger "B" has fired; this is given in equation 6.34.

$$\tilde{p}(A) = \frac{n(A\&B)}{n(B)} = \frac{p(A\&B)\cdot N}{p(B)\cdot N} = \frac{p(A\&B)}{p(B)} = \frac{p(A)\cdot p(B)}{p(B)} = p(A) \tag{6.34}$$

Another ratio is R defied as:

$$R = \frac{n(A\&B)}{n(A \mid\mid B)} = \frac{p(A\&B)}{p(A \mid\mid B)} \tag{6.35}$$

By construction, the relation holds:

$$p(A \mid\mid B) = p(A) + p(B) - p(A\&B) \tag{6.36}$$

Combining equations 6.36 and 6.35:

$$\tilde{p}(A \mid\mid B) = \frac{\tilde{p}(A) + \tilde{p}(B)}{1+R} \tag{6.37}$$

Errors are all of binomial type and are given for $\tilde{p}(A \mid\mid B)$ in equation 6.38.

$$\sigma_{A||B} = \sqrt{\left(\frac{\sigma_A^2 + \sigma_B^2}{\left(\tilde{p}(A) + \tilde{p}(B)\right)^2} + \frac{\sigma_R^2}{(1+R)^2}\right)} \tag{6.38}$$

Event Selection

In estimating the systematic uncertainty introduced by the muon selection, an "N-1" type study with each of the muon quality cuts is performed. To do this study, the efficiency for cutting positive and negative muons for all cuts *except* the cut under studying (N-1 cuts), and the efficiency for accepting positive and negative muons after the studied (N^{th}) cut is applied, are compared. For a cut to be completely unbiased, the ratio of efficiencies will be 1; To estimate the systematic uncertainty, the bias in the rate is shown in equation 6.39 where $\eta^{\pm}$ is the efficiency at which charge is cut.

$$\xi_s = \eta^+/\eta^- \tag{6.39}$$

From equation 6.39, it is straight-forward to estimate the systematic as it is given in equation 6.40 where σ_{ξ_s} is the binomial error.

$$\sigma_s = \sqrt{(1-\xi_s)^2 + \sigma_{\xi_s}^2} \tag{6.40}$$

Alignment

The global alignment between the tracker and muon systems is key to reconstructing high-p_T muons in the context of global muon reconstruction. If the alignment is poor there will be poor resolution in q/p_T, leading to charge misidentification and p_T migration.

To estimate the systematic uncertainty due to detector mis-alignment, muon reconstruction on the same events for two different alignment scenarios are compared. The selections are applied to both samples, and the charge ratio is compared on an event-by-event basis. The systematic uncertainty is estimated by looking at the relative change in the charge ratio per p_T bin as given in equation 6.41. R_{V13} and R_{V12} refer to the alignment version that are used for the comparison.

$$\xi_{alignment} = \frac{R_{V13} - R_{V12}}{R_{V13}} \tag{6.41}$$

Magnetic Field

The magnetic field of the CMS detector has a quite complex shape, making it difficult to map it in an accurate way. Any uncertainty in the determination of the magnetic field will directly affect the determination of the curvature of the cosmic muons, thus their transverse momentum and charge might substantially change.

CRAFT08 data gave rise to the lack of understanding of the magnetic field in the muon system, so the knowledge of the magnetic field evolved in tandem with this analysis. To estimate the systematic uncertainty, an older tracking pointing reprocessing of the data is utilized. In the same style that the alignment systematic was estimated, the data is re-reconstructed with different field-map models. The

relative difference in the charge ratio between the two field-map models are shown in equation 6.42.

$$\xi_{bfield} = \frac{R_{new} - R_{old}}{R_{new}} \tag{6.42}$$

Molasse Model

The model of the molasse above the CMS detector has a quite complex structure and is relatively poorly understood. The uncertainty in the molasse model will affect the determination of the momentum of the cosmic muons on the earth's surface. The molasse above the CMS detector is composed of about 50 m moraine and about 22 m rock [62]. The uncertainty of each composition is on the order of a few meters. To estimate the molasse model systematic, an energy difference on the muon momenta on the earth's surface is applied. The energy difference is corresponding to muon energy loss in 3 m rock, which is equivalent to about 5 m moraines. The relative difference in the charge ratio between them are shown in equation 6.43. The relative systematic uncertainties are shown in table 6.2.

$$\xi_{rock} = \frac{R_{+3m\ rock} - R_{-3m\ rock}}{R} \tag{6.43}$$

Summary

All the relative systematic uncertainties have been summarized in figure 6.15. The main source of uncertainty in the low-p_T regime stems from the selection, but is less than 2%. In the high-p_T bin, the muon alignment is the highest uncertainty with a 12% relative uncertainty.

6.4.5 Results

In this section, the measurement outcomes are reported after combining the methods described so far. The final outcome is divided into two parts: the measurement

p^{Earth} range [GeV]	R	σ_{rock}/R [%]
35 - 60	1.26	0.87
60 - 75	1.20	0.42
75 - 100	1.36	1.45
100 - 155	1.28	0.55
155 - 360	1.31	0.14
360 - ∞	1.33	0.02

Table 6.2
Relative systematic uncertainties due to the molasse model as a function of p^{Earth} for the global fit.

result at the center of the detector, and the result as the surface of the earth propagated from the center of the detector.

Measurement of the charge ratio at the PCA

Before unfolding the charge asymmetry ratio to the surface of the earth, cross-checks on the charge ratio at the PCA are performed by comparing the performance of different reconstruction algorithms. Figure 6.16 shows the charge ratio as a function of p_T for three different fits: global, tracker and TPFMS.

Propagation of the Charge Ratio to the Earth's Surface

In this section the results of the two unfolding steps are presented, summarized in figure 6.17. The first unfolding, from measured transverse momentum at the PCA to true momentum at the CMS 8 m surface, returns a very stable result. This is achieved thanks to the chosen momentum bins, which provide small off-diagonal elements. The second unfolding, from true momentum at the CMS 8 m surface to true momentum at the earth's surface, has large off-diagonal elements at low momentum which induce

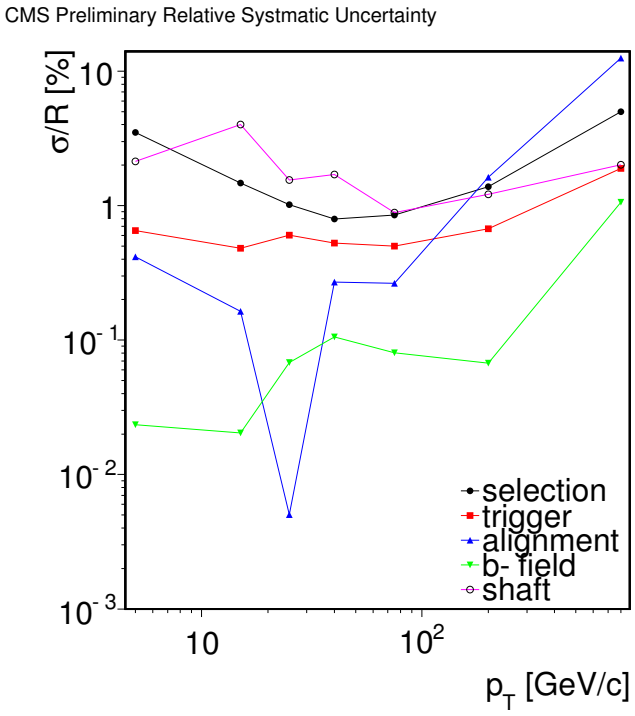

Figure 6.15. Relative systematic uncertainties. Event selection leads the selection with $< 2\%$ systematic uncertainty in the low-p_T regime. In the high-p_T bin, the alignment systematic dominates with a $\sim 12\%$ uncertainty.

instabilities in the unfolding process, as can be seen in figure 6.17 (c). The current unfolded ratio of positive to negative muons as a function of the muon momentum at the earth's surface is summarized, together with the statistical and systematic errors, in table 6.3. The result is comparable with results from previous experiments as shown in figure 6.18. This result together with results from the CMS MTCC [63] and other experiment can be compiled together to provide better parametrization for models on the interactions in the atmosphere.

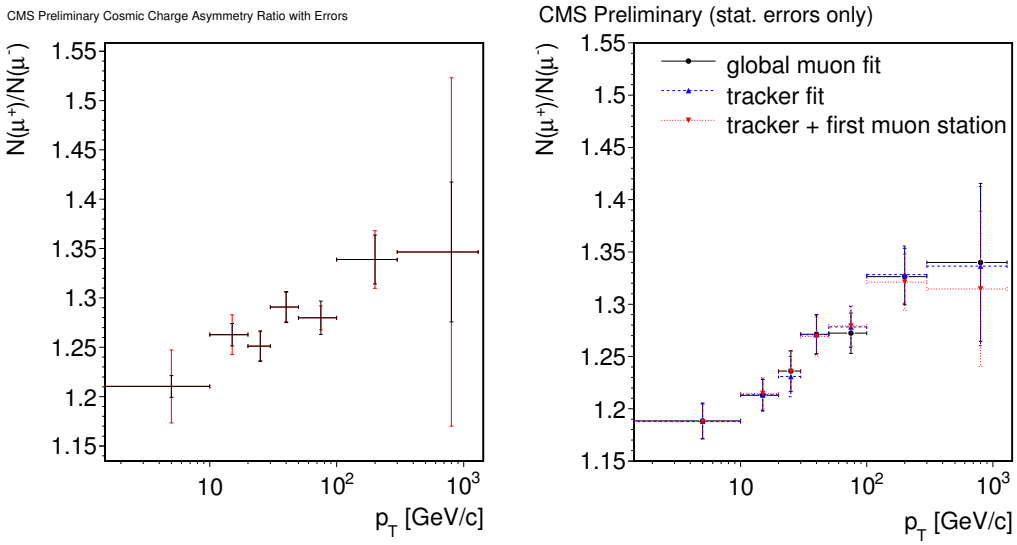

Figure 6.16. Uncorrected charge ratios comparison. Statistical (black lines) and systematic (red lines) errors for the global fit (left). Statistical errors only for the global, tracker and TPFMS fits (right).

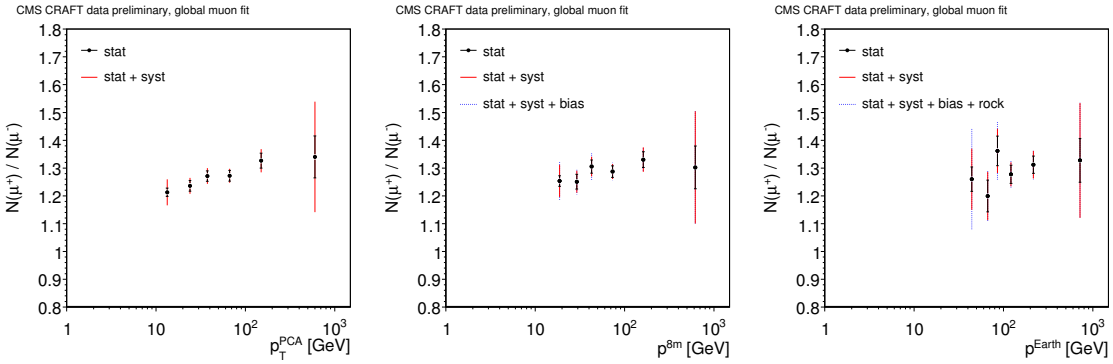

Figure 6.17. Ratio of positive to negative muons in the different unfolding steps: Uncorrected charge ratio vs. measured p_T at the PCA (left); Unfolded charge ratio vs. true p at the CMS 8 m surface (center); Unfolded charge ratio vs. true p at the earth's surface (right). The solid black lines correspond to the statistical uncertainty, the solid red lines correspond to the systematic uncertainty and the dotted blue lines correspond to the bias introduced by the unfolding technique, together with the molasse model for the transfer to the earth's surface.

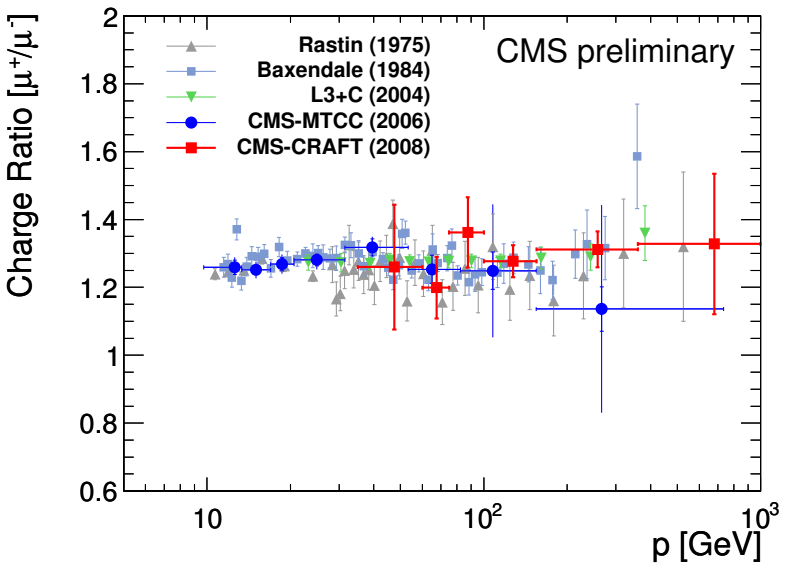

Figure 6.18. Momentum spectra of the ratio of positive to negative muons at the earth's surface measured by the CMS and previous experiments.

p^{Earth} range [GeV]	R	σ_{stat}	σ_{syst}	σ_{bias}	σ_{rock}
35 - 60	1.260 ± 0.184	0.044	0.101	0.148	0.011
60 - 75	1.199 ± 0.091	0.057	0.065	0.028	0.005
75 - 100	1.362 ± 0.104	0.053	0.059	0.064	0.020
100 - 155	1.277 ± 0.047	0.033	0.028	0.017	0.007
155 - 360	1.312 ± 0.053	0.031	0.039	0.018	0.002
360 - ∞	1.328 ± 0.207	0.079	0.191	0.013	0.000

Table 6.3
Unfolded charge ratio as a function of p^{Earth} for the global fit.

6.5 Flux Measurement

The absolute muon flux and its momentum dependence are mainly determined by the flux of nucleons entering the atmosphere and the inclusive meson production

cross sections in high-energy hadronic interactions. Large uncertainties still exist in the understanding of the energy spectrum above 0.1 TeV of primary cosmic rays. The details of high-energy hadronic interactions still lack theoretical understanding and there is little experimental data in the relevant energy and phase space regions [64]. Therefore the ground-level muon flux is widely used to tune or verify the parameters of atmospheric cascade calculations [65].

6.5.1 Overview

The goal of the flux analysis is to measure the momentum dependence of the cosmic muon flux at the CMS detector and the earth's surface.

The cosmic flux measurement consists of counting the number of observed muons passing through a defined surface of the CMS detector and dividing it by the amount of time elapsed during the experiment after all corrections.

Runs were selected which have stable condition of magnetic field, RPC, DT, L1 trigger, silicon and pixel tracker in the global Data Quality Monitoring (DQM). The details of each run are listed in table 6.4. The raw muon rate without any correction is shown in figure 6.19, the raw muon rate stayed stable for the selected runs at about 92 Hz.

6.5.2 Measurement Surface

The fact that cosmic muons arrive and be reconstructed anywhere within the bulk of the CMS detector makes it necessary to propagate measured tracks to a common reference surface at which the flux measurement is to be made. A cylinder encircling the outermost extent of the barrel detectors ($R = 8$ m) is used in order to have direct comparison with MC. It is also able to provide a uniform positional resolution after extrapolation to the measurement surface.

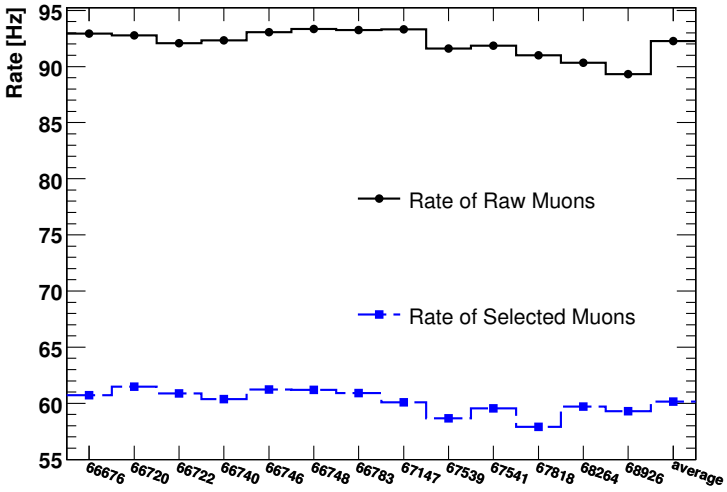

Figure 6.19. Raw and selected muon rates as a function of the run number.

6.5.3 Efficiencies

Since an unbiased estimation of both trigger and reconstruction efficiencies using only collected data is impossible, MC samples are used for estimating the detector efficiencies.

The efficiency of the standalone muon reconstruction was measured by the tag-and-probe method using good-quality tracker tracks as presented in Chapter 4. Good agreement was observed between the results using the tag-and-probe method with data and using MC truth method with MC samples, therefore the reconstruction efficiency measured with the MC samples is applied to the result. The efficiency measured using the tag-and-probe method with data was used to estimate the uncertainty.

Measuring the trigger efficiency using data is inherently difficult, therefore the software trigger emulation was used as the baseline indicator for trigger efficiency, while tag-and-probe tests are performed to estimate differences between the simulation and what is observed in the data.

The trigger efficiencies in emulation are measured in terms of the incident position of the generated cosmic muons, and integrated over the angular spectrum of the simulated events. The average efficiency for cosmic muons with at least 15 GeV as a function of the incident Z and ϕ position is shown in figure 6.20.

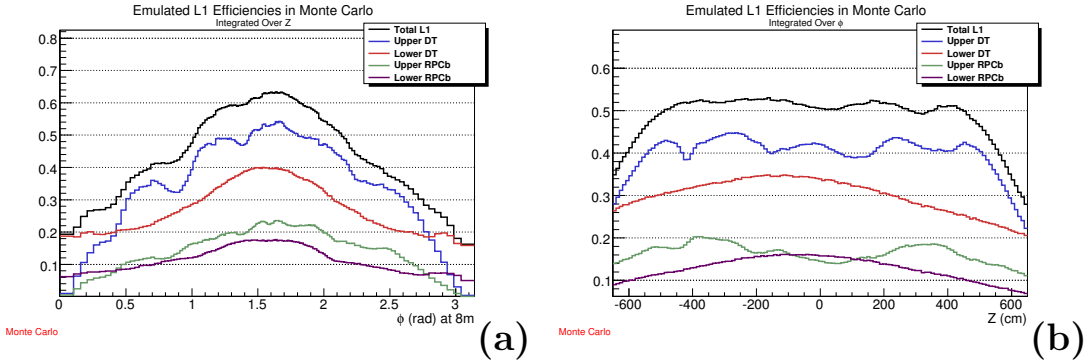

Figure 6.20. L1 efficiencies for P $>$ 15 GeV (a) vs. ϕ (b) vs. Z

The efficiency is highest in the vertical region of the detector ($\phi \approx \pi/2$), and is lower near the ends of the barrel (Z $\rightarrow \pm$650 cm) as the phase space of triggerable incident angles shrinks.

The precise behavior of the trigger efficiency is momentum dependent. The angle of incidence of the muon is the most critical factor for the trigger efficiency. Because muons with higher momenta are able to penetrate more material, the shape of the cosmic muon spectrum increasingly favors non-vertical angles of incidence with increasing momentum. This effect leads to a slight dip in the total trigger efficiency at higher momenta, as shown in figure 6.21.

6.5.4 Event Selection

All the events used in the analysis are required to have at least one L1 trigger candidate originated within the Drift Tube (DT) or Resistive Plate Chamber (RPC) barrel subdetectors.

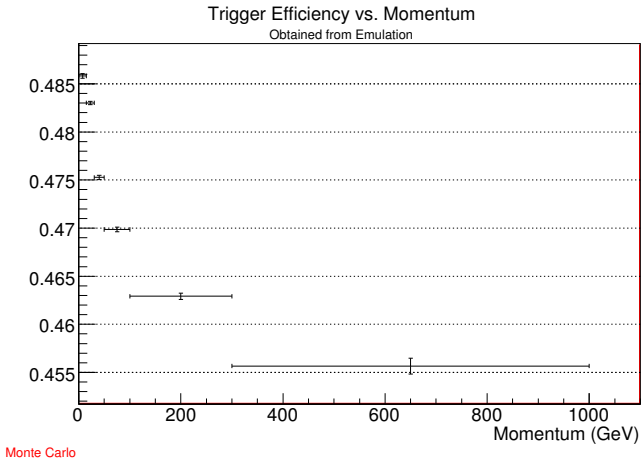

Figure 6.21. L1 efficiency momentum dependence.

The quality of a reconstructed standalone muon track is highly correlated with the number of hits contributing to the track. Tracks with hits from more chambers usually have better quality. In this analysis tracks with hits from five or more chambers and at least four hits in each chamber are required. This provides very good quality cut as well as suppressing almost all fake muon tracks. This cut implicitly requires that the used 1-leg standalone muons must travel through both hemispheres of the CMS detector, thus giving better resolution due to the longer lever arm.

Another quality cut used to deselect mis-reconstructed tracks is to require $p_y < 0$, i.e., the reconstructed momentum must be pointing down. This selection has efficiency over 99.9%. Since the measurement surface was chosen to be the CMS barrel region, the positions are required to be within z from -650 cm to 650 cm, and ϕ from $\pi/4$ to $3\pi/4$ at the CMS 8 m outer enveloping surface. The extrapolated position for a standalone muon track must be in the region. The efficiencies are shown in table 6.5.

Removing Fake Tracks The $N_{\text{DT Chambers with 4+ hits}} > 4$ cut successfully eliminated all events that contained fake tracks, and kept a selection efficiency of about 57%. The $p_y < 0$ cut has marginal effect as expected. After these selections about

10% of the remaining events are lost because their entry points are out of the chosen region. Multi-track events happened occasionally during the cosmic runs, and are irreducible, as shown in the figure 6.22 (b). The Monte Carlo sample only produces single muons and, therefore, does not exhibit the higher multiplicities

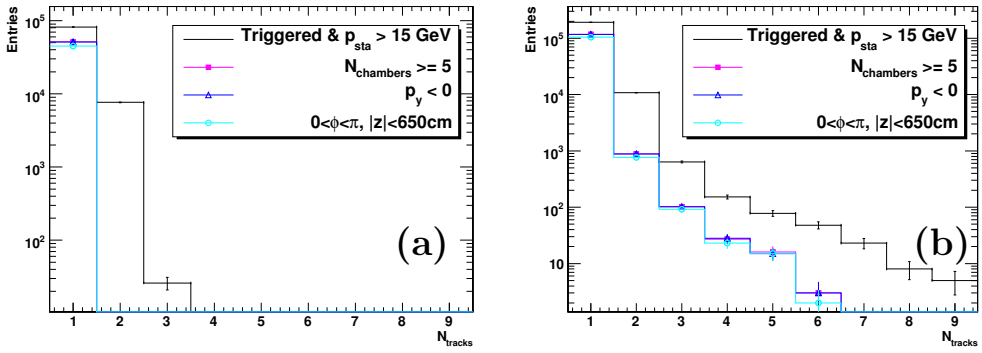

Figure 6.22. The number of standalone muon tracks per event for MC samples (a) and data (b).

Removing Duplicate Tracks Because cosmic muons come at random times, and there is a finite time for the detector readout, it is possible for the same physics event to cause more than one trigger; potentially leading to the miscounting of a single muon as two or more if detector readout also occurs. This problem is seen to exist even with the application of a trigger rule which prevents two events to be triggered within a span of three bunch crossing (BX)s of each other. To correct for the rare case in which a cosmic muon causes not only multiple triggers, but is also reconstructed as more than one track passing selection; cuts are applied which veto tracks having z, ϕ, and angles of incidence very close to a track in the immediately proceeding event.

The number of reconstructed standalone muon tracks per event for MC samples and data is shown in figure 6.22. The numbers of entries on y with an arbitrary scale demonstrates the relative influence of each selection cut. The MC samples do not contain multi-track events since each event has only one simulated track.

6.5.5 Time Measurement

The time base used for measurements of the flux is the LHC orbit number. An orbit counter, corresponding to the length of time it would take for a bunch of protons to circulate around the LHC ring, $\frac{26.7\text{km}}{3\times10^5\text{km/s}} = 8.9 \times 10^{-5}$ s, is recorded at the CMS detector. For each successful barrel muon trigger, the number of elapsed orbits since the previous trigger is computed and summed as either effective live-time or dead-time.

Since cosmic muons arrive at the CMS detector randomly in time, the distribution of the length of time between cosmic muon events is expected to be exponential. The exponential parameters are determined by the real detector trigger efficiency. The deviations from the probability distribution in the tails are likely to be an effect of the imperfect detector. In order to determine the amount of dead-time for a given sample of data, the distribution of missed orbits within the entire trigger path was converted into a probability distribution, and cut on the maximum realistic amount of time elapsed between live triggers.

As stated above the number of "missed orbits" (using the LHC orbit index) between triggers within the sample of events is used as the time metric for this analysis. Dead-time was determined by observing the length of time between adjacent triggers, as illustrated in figure 6.23.

The probability for random fluctuations above 1000 missed orbits is very small. To avoid all ambiguity, a loose threshold cut of 2000 orbits was applied to define dead-time. The corresponding probability obtained is:

$$\begin{aligned} P(n_{orbits} > 2000) &= \int_{2000}^{\infty} dn \cdot s e^{s \cdot n_{orbits}} \\ &= e^{2000 \cdot s} \\ &= 1.455(10) \cdot 10^{-19} \end{aligned} \tag{6.44}$$

The uncertainty was estimated by the total number of events which do not fit the probability distribution. The integral of the histogram minus the integral of the

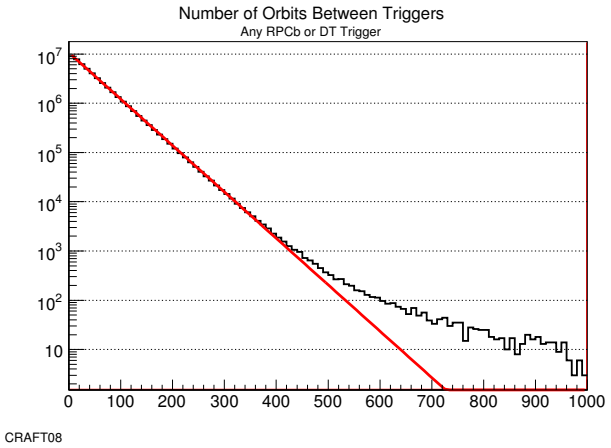

Figure 6.23. Number of orbits between any trigger in the trigger path.

exponential fit, is used to estimate the number of times the data have a possible long delay between triggers.

6.5.6 Unfolding

It is critical to be able to estimate all efficiencies as a function of incident momentum, as well as the measurement biases due to imperfect reconstruction for all ranges of momenta. For the differential flux measurement, the measurement biases due to imperfect reconstruction for all ranges of momenta are corrected by the same unfolding method used in the charge ratio study. Momentum smearing matrices for each zenith angle bin were built from momenta on the earth's surface extrapolated from the corresponding reconstructed and simulated momenta on the CMS surface, as presented in figure 6.24. The matrices were then applied to the raw extrapolated momentum differential spectrum.

Acceptance

The acceptance is especially important for the flux measurement, but can only rely on the relatively poor understanding of the molasse above the detector. The

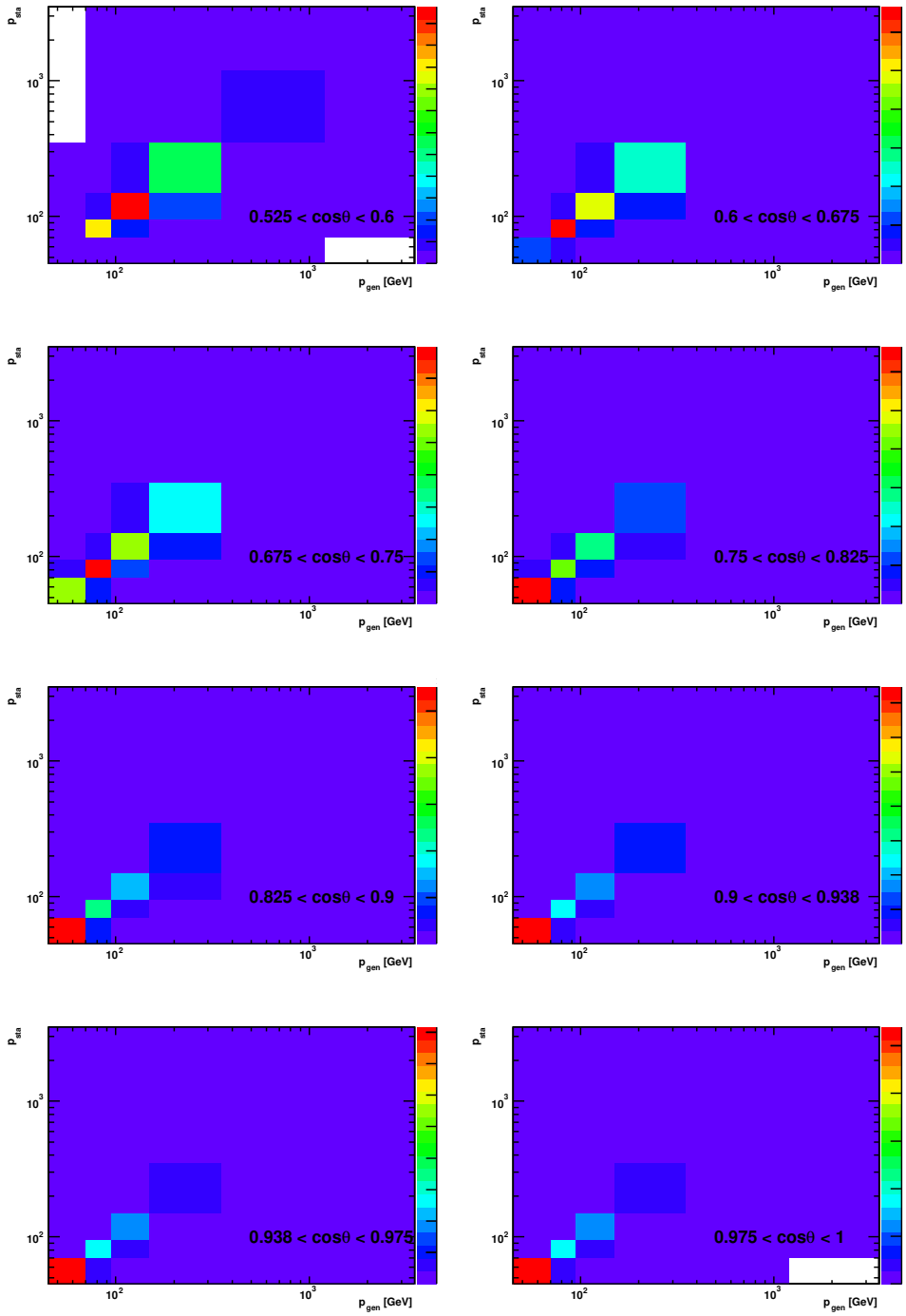

Figure 6.24. Momentum resolution matrices for each zenith angle bin.

acceptance was estimated by generating a great amount of events on the earth surface (one billion events for the first four p-bins, and one billion events each for the last two p-bins). The number of events with muons reaching the CMS detector divided by the total number of events is defined as the acceptance for each momentum and zenith angle bin.

6.5.7 Results

The raw spectrum were extracted by the number of selected muons normalized by the corrected time elapse as a function of momentum p. After corrections of trigger, reconstruction and selection efficiencies, and unfolding the p-resolution, the differential rate on the surface of the CMS as a function of momentum p is shown in figure 6.25.

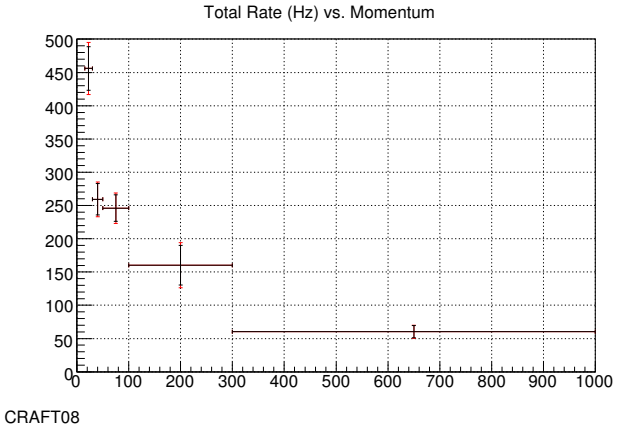

Figure 6.25. Corrected rate vs. p on the CMS 8 m surface.

After the migration and the acceptance estimation, the final spectrum presented as $\Phi p^3 dp$ with comparison with the result from L3C experiment is shown in 6.26.

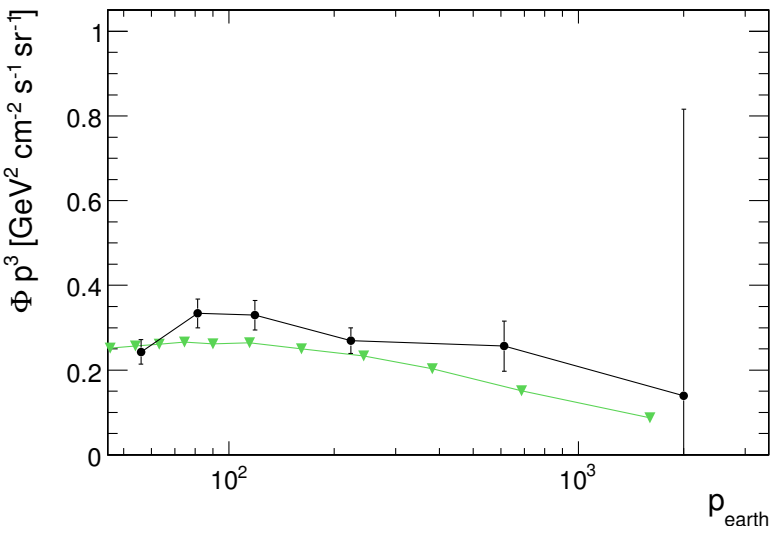

Figure 6.26. The measured muon spectrum for zenith angles from 0° to 12.8° ($0.975 < cos\theta < 1.0$) (solid dots) with comparison with previous L3C experiment [65] (triangles).

6.6 Summary

Different measurements with different systems of the detector using cosmic muons are described in this chapter. Various selections are optimized for different dedicated purposes. Detector efficiencies and resolutions with cosmic muons were extensively studied. It is demonstrated that the CMS detector can provide physics measurements which are able to improve the world average values. The systematic uncertainty for cosmic physics is only dominated by the modeling of the molasse above the CMS detector.

Run Number	Events	Time[s]	Num L1/DT	Num L1/RPC	Raw Muons	Selected Muons
66676	4721726	11077	3770204	2545160	1029282	672469
66720	4342986	6568	2231401	1488339	609282	403888
66722	15924465	26383	8857988	5827348	2429498	1606084
66740	9179116	14539	4898499	3204491	1342506	877555
66746	9659998	16066	5464505	3513080	1495259	983666
66748	13733204	21219	7253899	4821558	1980610	1298470
66783	9839168	20630	6989261	5351264	1923914	1256443
67147	9296499	14136	4962203	1972871	1319017	849478
67539	8182322	12522	4314682	1529691	1146930	734650
67541	3044738	4949	1701273	599544	454646	294673
67818	20303938	27024	9391729	5691200	2459500	1564267
68264	5358751	11449	4002798	0	1034226	683492
68926	2845757	4703	1633587	0	420075	278925
TOTAL	**116432668**	**191265**	**65472029**	**36544546**	**17644745**	**11504060**

Table 6.4
Run list.

	Data		MC	
Cuts	efficiency [%]	relative [%]	efficiency [%]	relative [%]
Triggered, $p_{sta} > 15$ GeV	100.0	-	100.00	-
$N_{\text{DT Chambers w/ 4+ hits}} > 4$	56.67	56.67	57.17	57.17
$p_y < 0$	56.65	99.97	57.16	99.99
$0 < \phi < \pi$, $\lvert z \rvert < 650$ cm	51.11	90.23	50.18	87.79

Table 6.5
Selection cuts and efficiencies.

7. DRELL-YAN ANALYSIS

As described in Chapter 2, the Drell-Yan process provides a very clean signature and can be regarded as a 'standard candle' at the LHC. The precise measurement of its cross section is a prerequisite for any discovery of new physics at the LHC. In this chapter, an exercise towards the first measurement of the cross section and mass spectrum of the Drell-Yan dimuon production with the CMS experiment is presented [66]. The analysis was performed in the scenario of LHC collisions at $\sqrt{s} = 10$ TeV and assuming an integrated luminosity of 100 pb^{-1}. The Drell-Yan process has been studied in the mass range, starting from the Υ peaks up to the kinematic limit. Events at the Z and Υ peaks are used to measure the trigger and reconstruction efficiencies from data. Methods for signal selection and background rejection in the different mass ranges, where the sources and magnitude of backgrounds change substantially, are discussed, as well as experimental and theoretical systematic uncertainties.

7.1 Signal

The signal characteristics have been studied using the generator level information as obtained from the PYTHIA 6.4 Monte Carlo generator package [67]. Higher order electroweak corrections have been studied separately using the HORACE event generator [68] within the context of the CMS experiment [69]. These corrections are expected to be important for the mass region beyond the Z-resonance. Figure 7.1 shows the mass reach at a center-of-mass energy 10 TeV with an integrated luminosity of 100 pb^{-1}. It is evident that, with the first physics data, one can probe dimuon masses up to several hundred GeV. The corresponding transverse momentum and rapidity distributions of the γ^*/Z are shown in figure 7.1 (center) and (right).

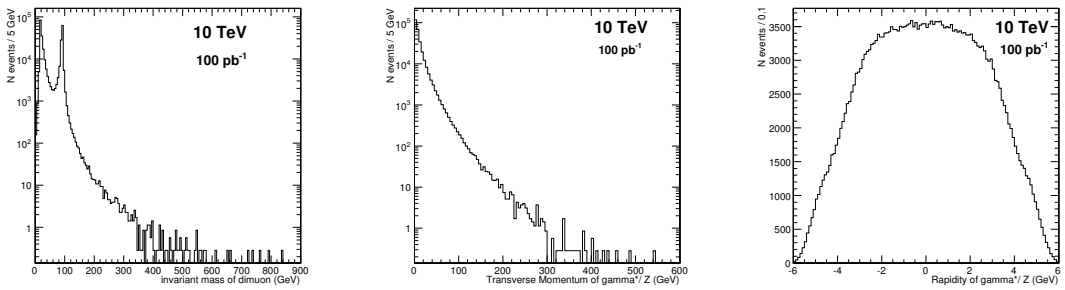

Figure 7.1. Dimuon mass reach (left), transverse momentum (center), and rapidity (right) distributions of γ^*/Z at the generator level for an integrated luminosity of 100 pb^{-1} at a center-of-mass energy of 10 TeV.

7.2 Datasets

The official Monte Carlo datasets produced in Summer 2009 were used in this exercise. The signal events, $Z/\gamma^* \rightarrow \mu\mu$, were generated with PYTHIA starting from an invariant mass of 20 GeV. Since the signal events contain two isolated muons, there are several processes that potentially can mimic the signal and which need to be considered as potential background. All data samples analyzed in this study are listed in table 7.1. For the low mass range ($M_{\mu\mu} \leq 40$ GeV), the contribution from QCD events to the background is maximal and various QCD samples were used to estimate this effect.

Though the probability of a jet faking a muon is low ($\approx 10^{-5}$), processes like W+jets and $t\bar{t}$+jets may produce two muons in the final state (where one muon can be fake) due to their high rates. Thus these processes need to be considered as potential background. In order to optimize the analysis work flow, only events passing an offline dimuon filter were considered for further analysis. The offline filter requires at least two reconstructed muons in the event and its efficiency for various datasets is presented in table 7.2.

Dataset	Events	Production cross section [pb]	Effective cross section [pb]
Z$\rightarrow \mu\mu$($M_{ll} > 20$)	1296192	1944.0	1944.0
DY ($6 < M_{ll} < 40$)	230582	12900	2339.8
DY ($M_{ll} > 200$)	10022	1.62	1.069
DY ($M_{ll} > 500$)	15342	0.0549	0.0455
DY ($M_{ll} > 1000$)	10296	0.00283	0.00256
DY ($M_{ll} > 2000$)	10091	5.86×10^{-5}	5.54×10^{-5}
W+Jets	9494588	40000.0	40000.0
$t\bar{t}$+Jets	927345	317.0	317.0
Z$\rightarrow \tau\tau$	1014480	1944.0	1944.0
inclusive $pp \rightarrow \mu + X$, $p_T^{\mu} > 15$	6246161	5.091×10^8	121675.0
inclusive $pp \rightarrow \mu + X$	5279540	5.156×10^7	11884.58
QCD20-30	11377053	4.97×10^8	2.0377×10^6
QCD30-50	11229012	9.177×10^7	5.6×10^5
QCD50-80	12905363	1.165×10^7	1.63×10^5
QCD80-120	840244	1.547×10^6	3.51×10^4
QCD120-170	328590	2.492×10^5	7.03×10^3
QCD170	464357	6.203×10^4	22.0×10^4
WW	204305	44.8	44.8
ZZ	199455	7.1	7.1
WZ	248236	32.4	32.4

Table 7.1
Number of generated events, production and effective cross sections for different MC samples.

7.3 Event Selection and Backgrounds

7.3.1 Online Selection

Events are selected with an OR of a single muon trigger (`HLT_Mu9`) and a dimuon trigger (`HLT_DoubleMu3`). The dimuon trigger has a larger geometrical acceptance

Dataset	Events passing offline selection	ϵ
Z$\rightarrow \mu^+\mu^-$ with mass > 20	627642	0.484
DY with $6 < M_{ll} < 40$	135445	0.587
W+Jets	404720	0.043
$t\bar{t}$+Jets	283465	0.306
Z$\rightarrow \tau\tau$	45781	0.045
QCD20-30	1224066	0.138
QCD30-50	3240014	0.30
QCD50-80	1116309	0.37
QCD80-120	371973	0.44
QCD120-170	166858	0.51
QCD170-up	271024	0.58
WW	22065	0.108
ZZ	30716	0.154
WZ	21968	0.123

Table 7.2
Offline selection efficiencies for various processes.

$|\eta| < 2.4$ and lower p_T thresholds than the single muon trigger. It is especially important to select events in the low-mass region. The definition of `HLT_Mu9` and `HLT_DoubleMu3` trigger paths are:

- Trigger path `HLT_Mu9` requires a muon, not necessarily isolated, with $p_T > 9$ GeV at L1 and HLT.
- Trigger path `HLT_DoubleMu3` requires at least two muons, not necessarily isolated, with $p_T > 3$ GeV at L1 and HLT.

7.3.2 Offline Selection

Events are selected if there are at least two reconstructed, opposite sign, global muons in the CMS detector within the pseudorapidity range of $|\eta| \leq 2.4$. The chain of selection criteria applied to the reconstructed events is as follows:

- Number of global muons ≥ 2. Figure 7.2 shows the invariant mass distribution of the dimuon system after requiring two global muons. It is evident that the QCD processes are dominant over the signal in the low mass region ($20 < M_{\mu\mu} < 70$ GeV).

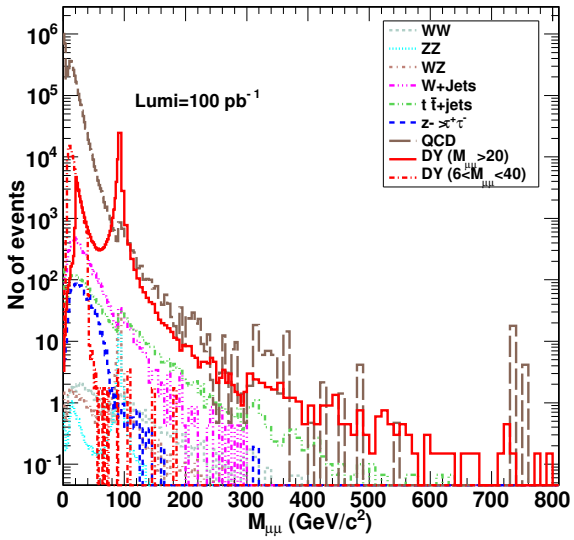

Figure 7.2. Dimuon invariant mass distribution for signal and backgrounds for events with at least two global muons.

- Since muons coming from heavy meson decays in QCD events will be relatively soft, both muons in the event are required to have p_T >10.0 GeV.

- The following reconstruction quality cuts on muon tracks have been applied:

1. The normalized χ^2 (χ^2/degree of freedom) (figure 7.3 (top)) of global muons is required to be < 10 in order to suppress muons from the decay of charged kaons and pions.

2. For each muon the number of hits is required to be larger than 11 to ensure the track is reconstructed properly. Figure 7.3 (bottom left) shows the distribution for the number of valid hits for the inner track of the global muons.

3. The sum of the d_0 variables $|d_0^{\mu 1} + d_0^{\mu 2}|$ is required to be < 0.1 mm in order to reduce the QCD background. Its distribution is shown in figure 7.3 (bottom right). This variable $d_0 = \frac{(v_x - x_{\rm BS})p_y - (v_y - y_{\rm BS})p_x}{p_T}$ is the closest distance between the track and the beam spot, where (v_x, v_y, v_z) is the point on the track satisfy so, and the beam spot is at $(x_{\rm BS}, y_{\rm BS}, z_{\rm BS})$.

- On average there is low activity around the muons in signal events, except for bremsstrahlung photons. Hence both muons are required to be isolated using one isolation criterion; an isolation cone of size $\Delta R = 0.4$ around the muon track is defined with a veto cone of size $\Delta R = 0.01$ to exclude the corresponding track. The relative isolation variable is defined as the sum of all additional tracks with transverse momentum above 1 GeV normalized to the transverse momentum of the candidate muon. The distribution of this isolation variable for signal and background is shown in figure 7.4. Based on the optimization as shown in the figure 7.4 (right), the fraction $\Sigma p_T^i (i \neq \mu)/p_T^\mu$ in isolation cone size of ΔR=0.4 is required to be < 0.1.

- The two muons with the highest momenta under consideration are required to have opposite electric charges.

- Since for a sizable fraction of the total number of events collected the two muons are produced from Z/γ^* at rest or boosted along the beam line, the muons are expected to be back-to-back. Figure 7.5 (left) shows the angle between the two

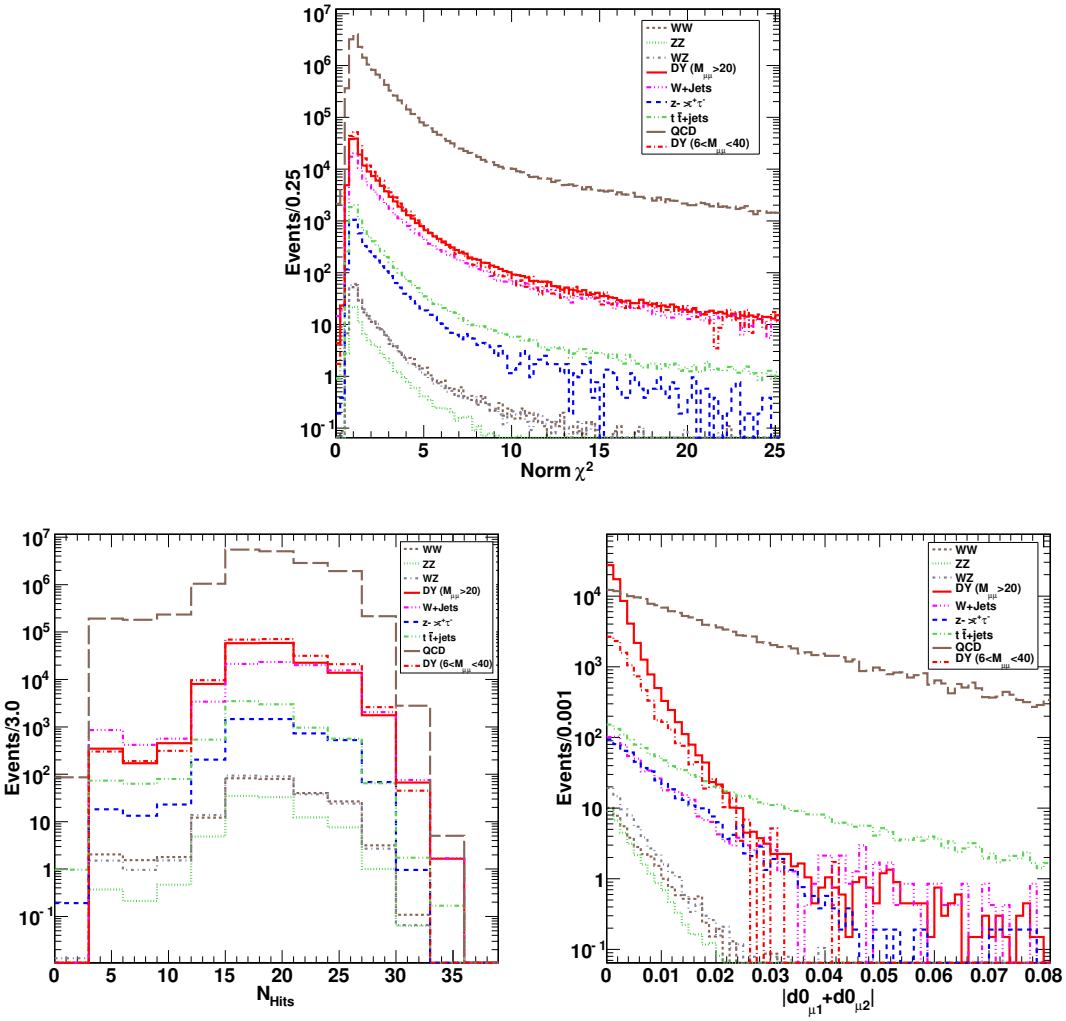

Figure 7.3. Normalized-χ^2 (top), number of valid hits for global muons (bottom left), and impact parameter of global muons (bottom right).

leading muons for the signal and various backgrounds. At the LHC a good fraction of the events will exhibit a significant transverse boost of the dimuon system, for example when it is balanced by a jet. In such a situation the muons will not be back-to-back, but are acoplanar. This can also happen due to final state radiation (FSR). The value for the angle between two muons has been optimized to be > 2.25 radian as shown in figure 7.5 (right).

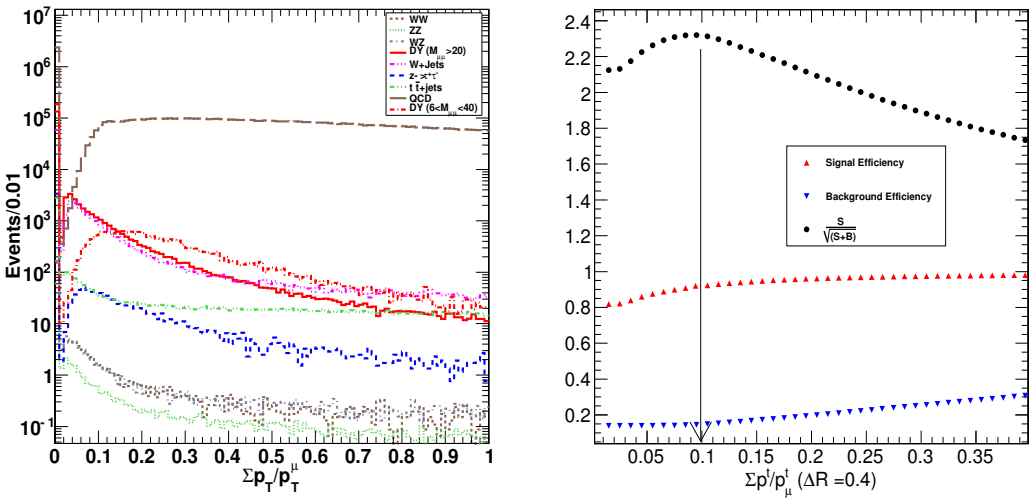

Figure 7.4. $\Sigma p_T^\mu / p_T^\mu$ of global muons in isolation cone ΔR=0.4 (left) and optimization plot for relative isolation variable (right).

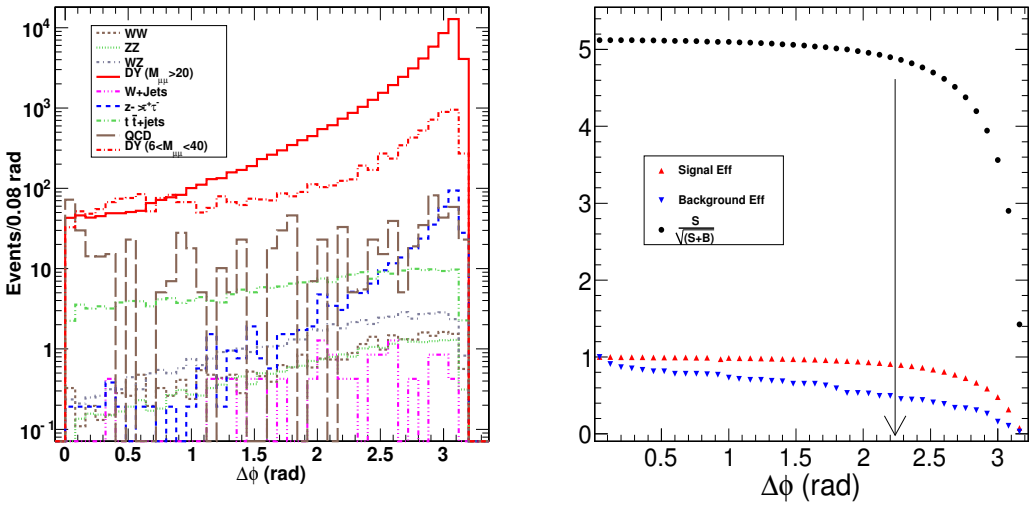

Figure 7.5. Angle between two leading muons (left)and optimization plot for angle between two leading muons (right)

Figure 7.6 shows the invariant mass distribution after all cuts have been applied.

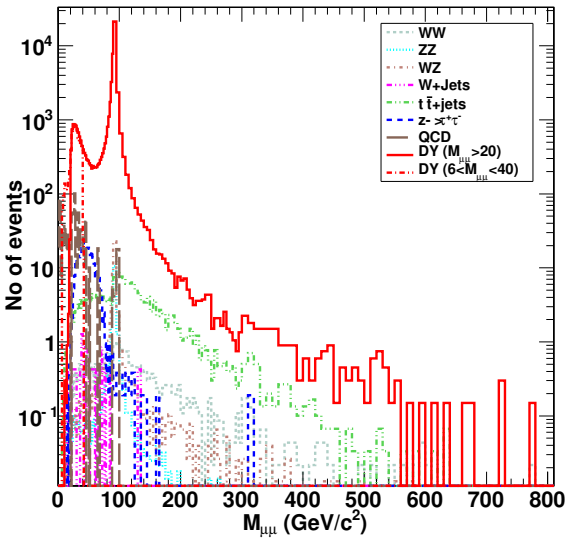

Figure 7.6. Invariant mass of two muons after tracker isolation.

7.4 Mass Resolution

To study the dimuon mass resolution the method described in Section 7.3 is used to match the MC truth to the reconstructed muons in preselected events. Drell-Yan MC samples with various mass cut-offs (6 GeV $< M_{\mu\mu} <$ 40 GeV, $M_{\mu\mu} >$ 20 GeV, $M_{\mu\mu} >$ 200 GeV, $M_{\mu\mu} >$ 500 GeV, $M_{\mu\mu} >$ 1000 GeV, and $M_{\mu\mu} >$ 2000 GeV) are used. For the preselected events of each sample, the generated and reconstructed dimuon invariant masses are compared to obtain the mass resolution distribution for each mass bin. The generated invariant mass is defined as the propagator mass of the hard interaction. The reconstructed mass is determined from the momentum information available for the two reconstructed muons. FSR photons are not used to compute the reconstructed mass. The distribution is then fitted to a linear combination of a Gaussian and a second order polynomial. Results of the fits are presented as a function of the dimuon invariant mass in figure 7.7. The left plot shows the mean value of the Gaussian, and the right plot shows the sigma of the Gaussian, obtained from the fit. As shown in the figure, the mass resolution has a dependency on the

dimuon invariant mass in both mean and sigma of the Gaussian. The mass resolution effect is about nine (seven) times larger in the high mass region than in the low mass region for the mean (sigma) value of the Gaussian.

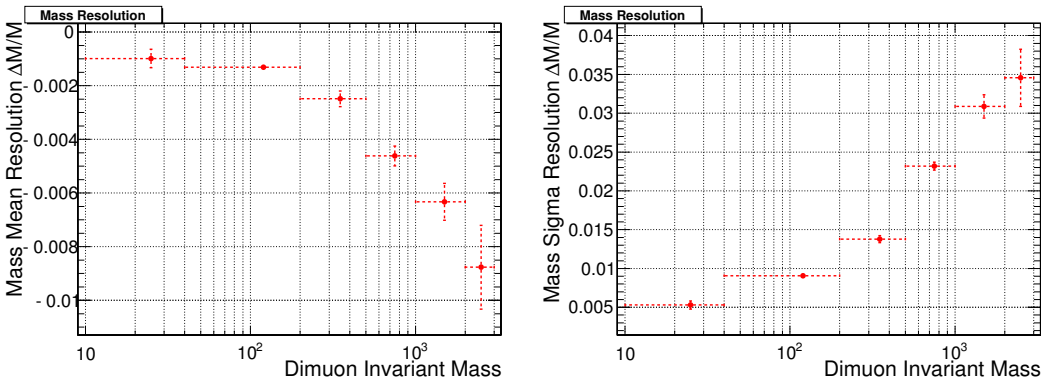

Figure 7.7. Mass resolution as a function of dimuon invariant mass. The left plot shows the mean value of the Gaussian, and the right plot shows the sigma value of the Gaussian, which is determined by the fit.

7.4.1 Unfolding

The measurement dimuon mass spectrum can be distorted because the reconstructed invariant mass may be migrated to an adjacent bin due to final state radiation, detector resolutions, and systematic biases. An unfolding procedure is needed to correct for this effect.

In the unfolding procedure, the measurement distributions are parametrized as a response function using MC samples, where the binned true distribution is mapped onto the measured distribution. In order to obtain the true distribution from real data the following matrix equation needs to be solved, e.g., using the singular value decomposition (SVD) method [70],

$$M_i = R_{ij} T_j, \qquad R_{ij} = \sum R_{ik}^{phy} \cdot R_{kj}^{det} \tag{7.1}$$

where M_i is the measured distribution from real data, T_j is the true value of the real data which is the solution of this equation and n is the number of bins. The matrix R_{ij} is the response function obtained from MC samples represented as a matrix. There are two different types of correction: physics effect correction for FSR and the detector resolution effect correction. R_{ik}^{phy} is the response function for physics effect correction, and R_{kj}^{det} is the response function for the detector resolution effect correction. In this analysis, the RooUnfold package [71] has been used to perform the unfolding.

Figure 7.8 shows the dimuon invariant mass distribution with the generator level MC truth (solid line), reconstruction (solid dots), and reconstruction with artificial smearing (open triangles). As shown in the plot, the reconstructed dimuon invariant mass distribution significantly deviates from the truth distribution, especially around the Z peak, as a result of the migration due to FSR. The artificial smearing is produced using the mass resolution studied in the previous section. The mean and sigma values of Gaussian in figure 7.7 are used to smear the invariant mass distribution. The artificial smearing takes into account possible larger smearing in the initial phase of data taking by multiplying mean and sigma values by a factor of ten. A Gaussian random distribution with these mean and sigma values is then generated for the smearing. Unfolding correction is applied to this distribution with artificial smearing to see how good the correction is. Figure 7.9 shows the two dimensional response function, which is created by using the nominal generated and reconstructed dimuon invariant masses. Off-diagonal entries in the response function result from migration due to FSR and the detector resolution.

The top plot in figure 7.10 shows the dimuon invariant mass distribution after unfolding correction. The reconstructed dimuon spectrum has almost the same distribution as MC truth (solid line) after unfolding. The bottom plot shows the relative difference of reconstructed dimuon invariant distribution from truth value. The difference is calculated as the difference between the truth value and the reconstructed value, divided by the truth value. Before applying unfolding corrections (filled points), the deviation is significant, especially in the Z peak region. After the unfolding correc-

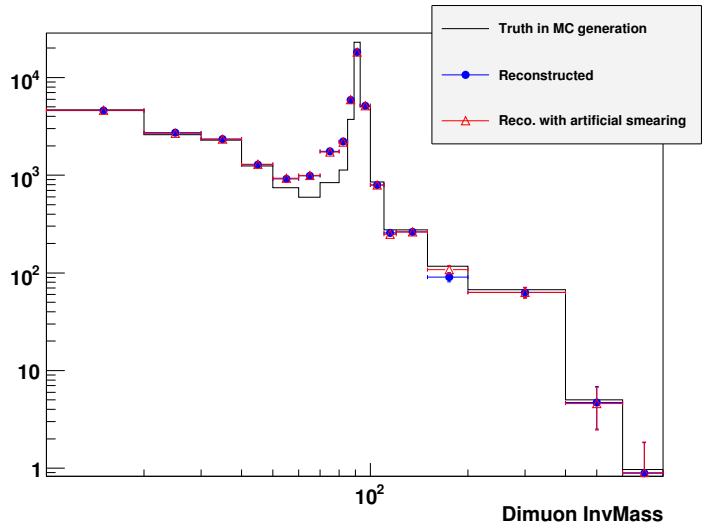

Figure 7.8. Dimuon invariant mass distribution with MC truth (solid line), reconstruction in CMS simulation (solid dots), and reconstruction in CMS simulation with artificial smearing (open triangles).

tion (open points), the deviation is almost negligible. The errors shown only include the statistical uncertainties.

7.5 Efficiencies

A measurement of the Drell-Yan cross section requires an estimation of the trigger, reconstruction, isolation, and selection efficiencies. These can be directly determined from data using the tag-and-probe method as described in Chapter 4.

Results for the trigger efficiency are presented as a function of dimuon invariant mass, and the muon reconstruction efficiency is determined with muon p_T and η dependencies.

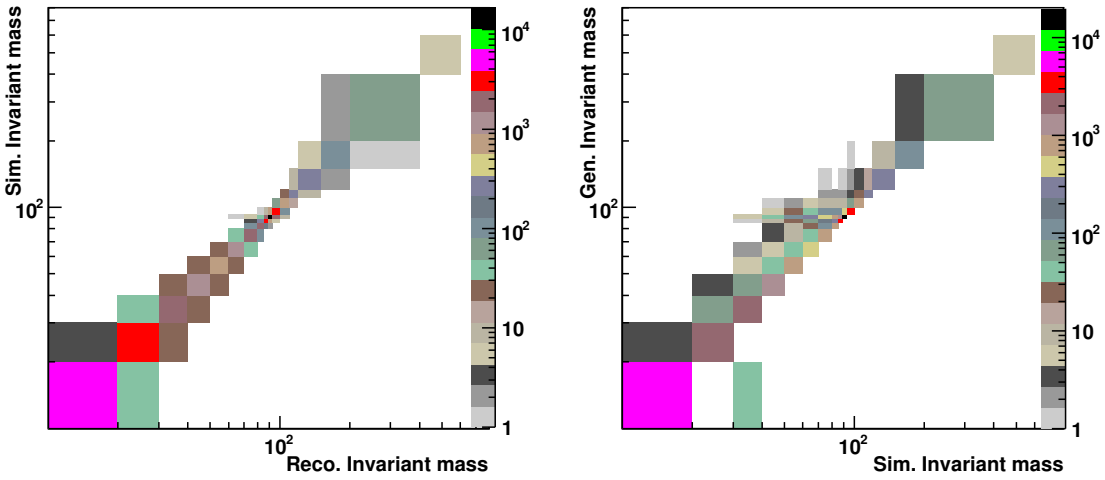

Figure 7.9. Two dimensional response function, which is created using generated and reconstructed dimuon invariant masses. The left plot is the response function for the detector resolution effect correction, and the right plot is the response function for the physics effect correction.

7.5.1 Trigger Efficiency

The trigger efficiency is estimated in two different ways: (a) using a MC based method and (b) using a data driven method. The MC based trigger efficiency is calculated using the following formula:

$$\varepsilon^{\mathrm{MC}}_{\mathrm{trigger}} = \frac{\text{number of events passing HLT\_Mu9 OR HLT\_DoubleMu3}}{\text{total number of events}}$$

In the data driven method the trigger efficiency is determined by using an independent trigger path, for example a jet trigger (`HLT_Jet30`). This jet trigger is independent of the muon trigger paths `HLT_Mu9` and `HLT_DoubleMu3` used in this analysis. The offline selection cuts are then applied to the independent dataset which results in eliminating a majority of the non-muon background contributions from the

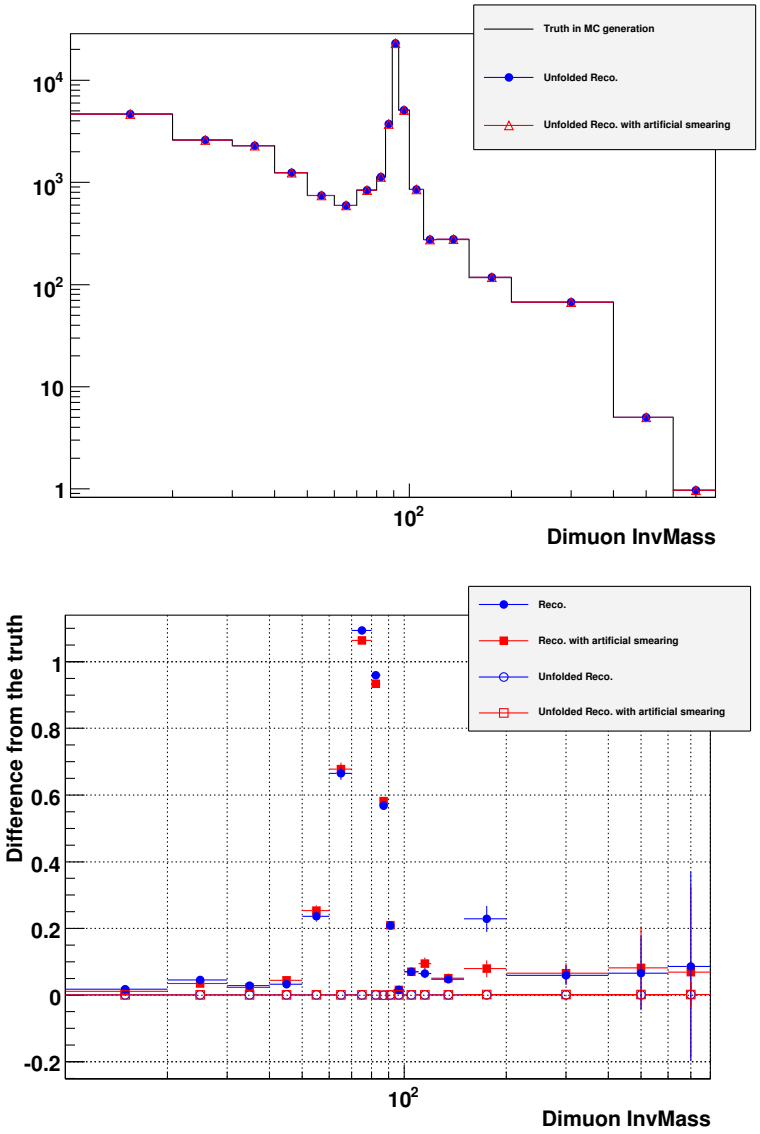

Figure 7.10. The top plot shows the dimuon invariant mass distribution after unfolding correction for reconstructed distribution and reconstructed distribution with artificial smearing. The bottom plot shows the relative difference from the truth value before unfolding (filled points) and after unfolding (open points).

jet triggered events. The resultant dataset is then examined to determine if the muon triggers fired, and the trigger efficiency can be calculated as follows:

$$\varepsilon_{\text{trigger}}^{\text{data}} = \frac{\text{number of events passing HLT\_Mu9 OR HLT\_DoubleMu3}}{\text{number of events passing HLT\_Jet30 AND Offline Cuts}}$$

Two different trigger menus are investigated, corresponding to different instantaneous luminosities (8E29 and 1E31). The luminosity 8E29 is designed for LHC start-up conditions and 1E31 is for low luminosity running conditions. Table 7.3 shows the expected trigger rates of some jet triggers for the two scenarios [72].

Triggers	8E29			1E31		
	L1 Prescale	HLT Prescale	Rate [Hz]	L1 Prescale	HLT Prescale	Rate [Hz]
Jet30	25	1	8.11 ± 0.22	1000	10	1.17 ± 0.31
Jet50	1	1	17.71 ± 0.33	100	2	1.84 ± 0.39
Jet80	1	1	3.01 ± 0.13	10	2	1.42 ± 0.34
Jet110	-	-	-	1	1	7.11 ± 0.77

Table 7.3
Summary for trigger rates from jet triggers.

The expected number of events passing the jet triggers are determined using the HLT trigger bits simulated in the MC samples. In this analysis, in lieu of a jet-triggered dataset, the offline event selection is applied as described in Section 7.3 (excluding the online requirement `HLT_Mu9` OR `HLT_DoubleMu3`) to both signal and background MC samples described in previous sections. The corresponding L1 and HLT prescale factors are used to estimate the trigger efficiencies and errors. Because all event selection requirements are applied except for the online requirements, most of the background contributions from jet triggered events are rejected. Thus only a small fraction of non-muon background events in the sample is used for the denominator of the trigger efficiency calculation.

Figure 7.11 shows the trigger efficiency as a function of the dimuon invariant mass. This trigger efficiency is obtained using events passing the `HLT_Jet50` trigger and the offline event selection. The solid dots denote the MC based result, and the open circles denote the data driven method. The left plot shows the `HLT_Mu9` trigger efficiency, and the right plot shows the `HLT_DoubleMu3` trigger efficiency. There are

no significant differences between the MC based and data driven results. All errors in the figure are statistical only.

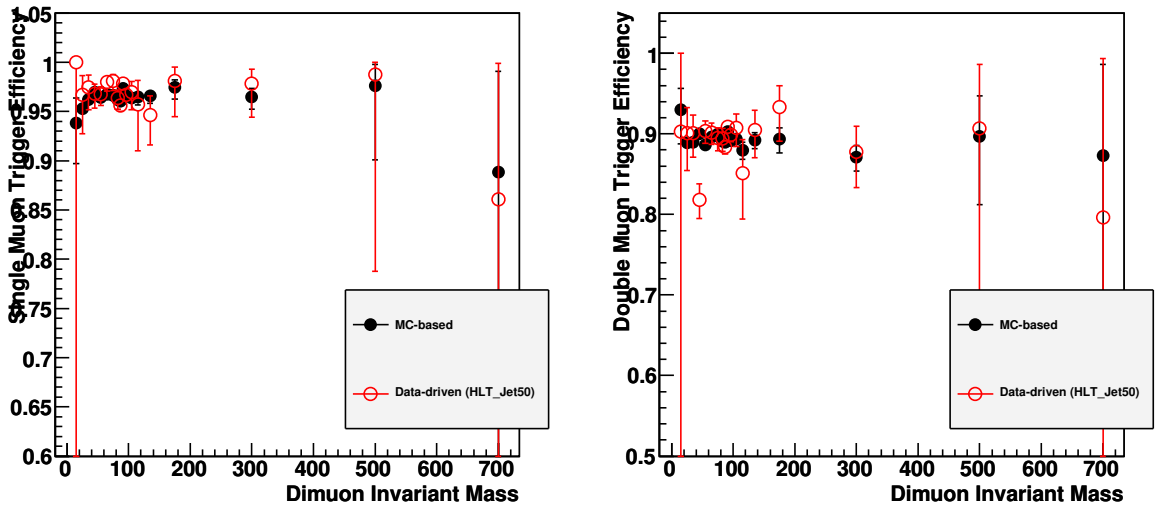

Figure 7.11. Trigger efficiency as a function of dimuon invariant mass. The left plot shows results for `HLT_Mu9` only, and right plot shows results for `HLT_DoubleMu3` only. Solid points denote the MC based result, and open circles denote the data driven method.

7.5.2 Reconstruction Efficiency

In the tag-and-probe method for this analysis, a tag muon for the $Z \rightarrow \mu\mu$ ($\Upsilon \rightarrow \mu\mu$) events is defined as a global muon in pre-selected events with $p_T > 10$ GeV (3.0 GeV). The probe muon can be either a standalone muon or a tracker track, which can be paired with the tag to render an invariant mass consistent with the mass of the resonances. For the $Z \rightarrow \mu\mu$ ($\Upsilon \rightarrow \mu\mu$) events, the mass window applied is 50 to 130 GeV (8.5 to 11.5 GeV). The standalone muon probe is used to calculate the tracker efficiency, while the tracker track probe is used to calculate the efficiency of the standalone muon reconstruction. A standalone muon or tracker track must

have $p_T > 10$ GeV (1.5 GeV) to be used as probe. A probe is defined as a passing probe if a track is found in the other subsystem of the detector within a region of $\Delta R(\eta, \phi) < 0.15$ around the probe.

For the Z-boson resonance, the fitting function is defined by the Voigtian function (Breit-Wigner convoluted with a Gaussian). For the Υ resonance, the fitting function is defined as three Gaussian peaks (one for each resonance). The efficiencies are evaluated by fitting each p_T and η bin separately. Since fitting needs significant statistics in each bin, the p_T bin boundaries are chosen to be 3.0, 4.5, 6.0, 10.0, 30.0, 40.0, 50.0, 100.0 GeV. The η bin boundaries are chosen to be -2.4, -2.1, -1.2, -0.7, 0.0, 0.7, 1.2, 2.1, 2.4. This binning is chosen in order to have approximately even statistics in each bin. With a combination of the Z and Υ fits, efficiencies are estimated over a large range of interest for the Drell-Yan cross section measurement. However with 100 pb^{-1} of data, Z resonance statistics is sufficient to measure the reconstruction efficiency using the tag-and-probe method as low as 10 GeV without the strict necessity of using the Υ resonances.

The efficiencies of global muon reconstruction as a function of p_T and η as calculated with the tag-and-probe method are shown in figure 7.12 to figure 7.13. The efficiencies obtained from the tag-and-probe method agree well with the efficiencies obtained from MC truth. The MC truth here denotes the value expected from tag-and-probe output if the fitter had calculated correctly the number of passing and failing signal events.

7.6 Systematic Uncertainties

7.6.1 Experimental

A major systematic effects in the cross section measurement result from the total muon efficiency and momentum resolution. The former can be controlled quite well with a large sample of Z events decaying to dimuons, and the effects for muons of different transverse momenta can be taken into account as corrections on top of this.

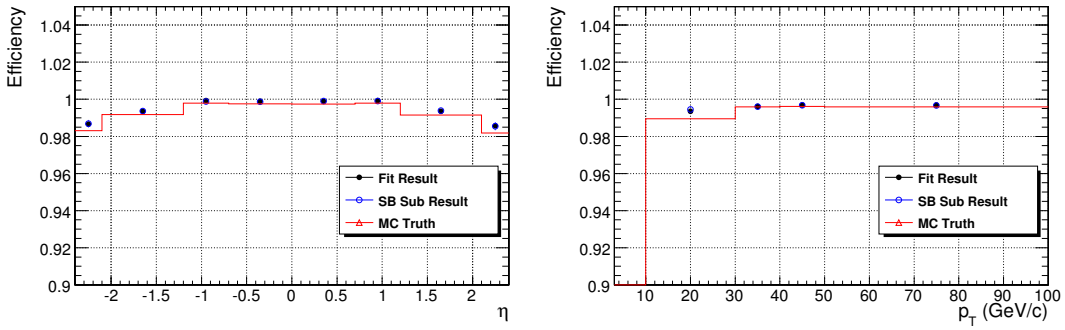

Matching and Refit Efficiency

Figure 7.12. Standalone to tracker track matching and global refit efficiency as a function of muon kinematic variables in the Drell-Yan sample. The left plots are for muon reconstruction efficiencies vs η integrated over all p_T, and the right plots are for the muon reconstruction efficiencies vs p_T integrated over all η. The solid points denote the tag-and-probe reconstruction efficiency using the Z-line fit, the histogram line denotes the MC truth reconstruction efficiency, and the open points denote the tag-and-probe reconstruction efficiency using the side-band subtraction method.

The latter is very important at high mass as smearing from lower masses from the steeply falling Drell-Yan spectrum can contaminate the high mass measurements, especially if the tails of the momentum resolution are not under control. The main source of systematic uncertainties on the momentum resolution comes from the alignment of the muon chambers and the central tracker. Since only ideal MC samples are used in the analysis, a detailed study of these effects are not performed.

7.6.2 PDF and Theory

The systematic uncertainties due to the Parton Distribution Functions (PDF) are calculated using the LHAGLUE interface to the parton distribution functions library LHAPDF [73,74]. Eighteen samples were generated with masses from 10 to 1000 GeV and apply the re-weighting technique with asymmetric errors as described in [75]. The

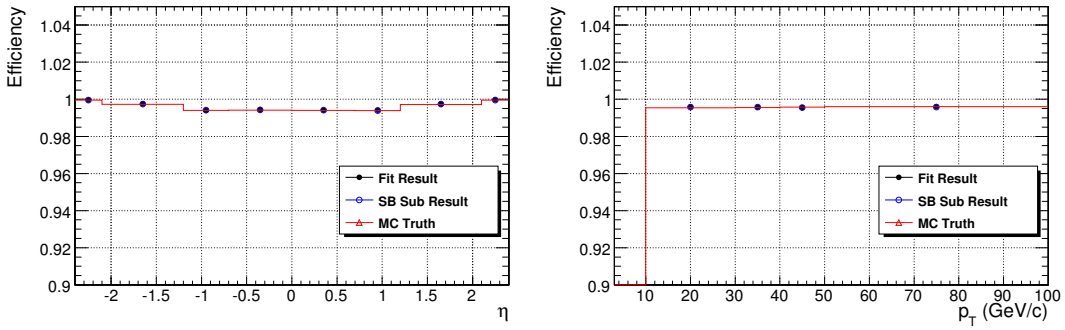

Tracker Muon Efficiency

Figure 7.13. Tracker muon identification efficiency as a function of muon kinematic variables in the Drell-Yan sample. Tracker muon identification efficiency is the efficiency for a global muon to be also identified as a tracker muon. The left plots are for single muon identification efficiencies vs η integrated over all p_T, and the right plots are for the single muon identification efficiencies vs p_T integrated over all η. The solid points denote the tag-and-probe efficiency using the Z-line fit, the histogram line denotes the MC truth efficiency, and the open points denote the tag-and-probe efficiency using the side-band subtraction method.

results using the PYTHIA event generator are shown in figure 7.14 (left), using the CTEQ6.1 PDF set [13].

In order to derive the PDF uncertainty on the Drell-Yan cross sections ratios to the Z peak, two approaches are possible:

- 'Naive' approach assuming no correlation between the points and just applying standard error propagation.
- 'Correlated' approach [76]: as a set of 40 PDFs for CTEQ6.1 is used, one could expect the upward or downward deviations from the central value for a given PDF to be preserved for adjacent mass bins, and thus have a *reduced* impact on the cross section ratios to the Z peak.

As a normalization point, events from the Z peak (80–100 GeV) are chosen. For an integrated luminosity of 100 pb^{-1}, ~32000 signal events are expected in the dimuon

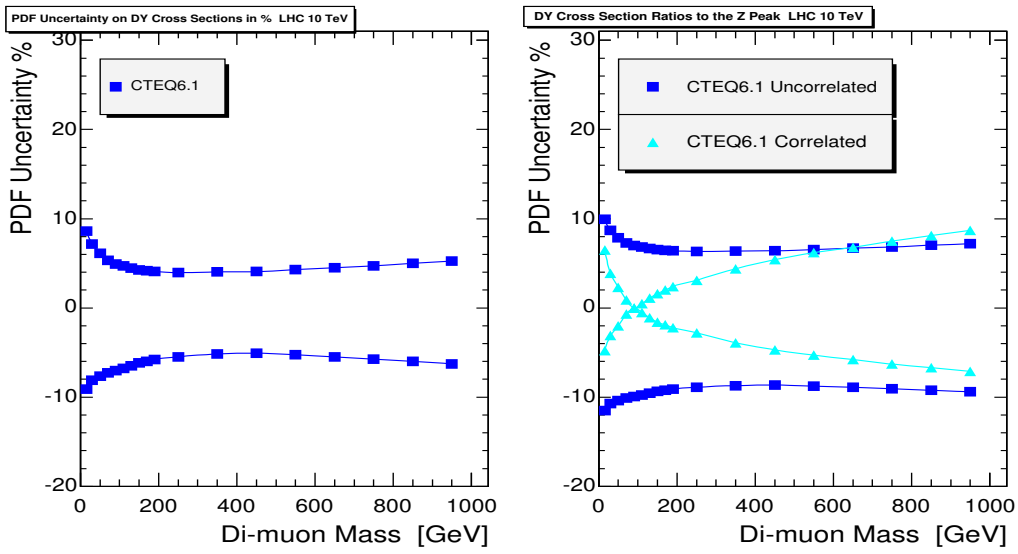

Figure 7.14. PDF uncertainties on the Drell-Yan cross sections, estimated with PYTHIA and the LHAGLUE/LHAPDF parton distribution functions library (left panel). PDF uncertainties on the Drell-Yan cross sections ratios to the Z peak (right panel). The re-weighting technique with asymmetric errors is used.

channel for this mass range. The PDF uncertainties on the ratios to the Z peak are shown in figure 7.14 (right) for CTEQ6.1. The 'correlated' approach indeed gives much smaller uncertainties not far from the normalization point and seems to be the correct approach. Gradually the correlation is lost and at high masses the error estimates become comparable, as expected. It is interesting to observe that the PDF uncertainties on the ratios to the Z peak are more symmetric than the errors on the cross sections for individual points.

The dependence of the Drell-Yan cross section on QCD corrections is studied in NLO and NNLO with the program FEWZ [77]. The results in the CMS acceptance region are shown in figure 7.15. The changes in going from NLO to NNLO are much smaller, so the two sets of k-factors are quite similar, starting to deviate more substantially only at the highest mass point. The variation of NNLO k-factors in the mass region under study is below 5% if a normalization to the Z is used.

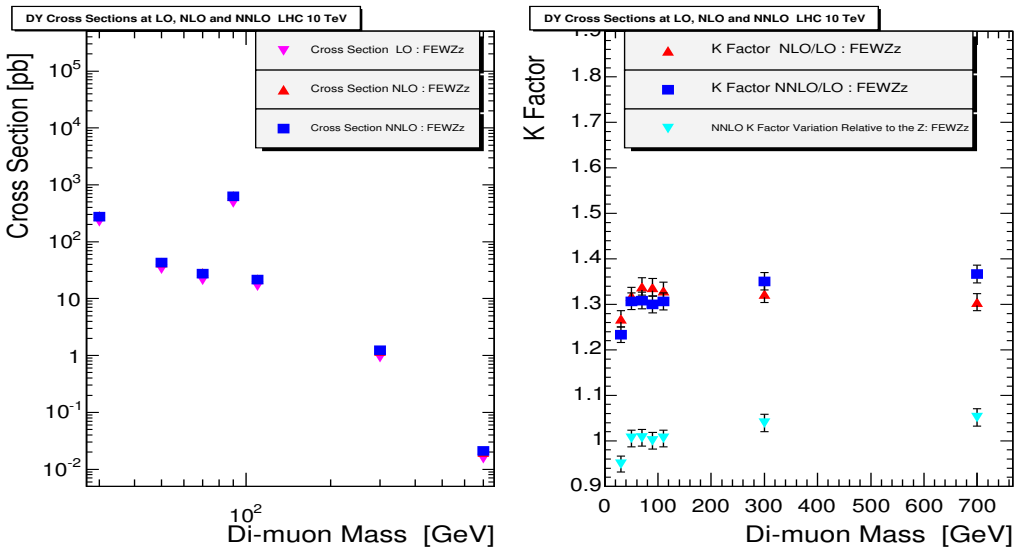

Figure 7.15. Drell-Yan cross sections at LO, NLO and NNLO, computed with FEWZz in the CMS acceptance region for muon pseudo-rapidities $\eta < 2.4$ (left). Mass dependence of k-factors (right).

7.6.3 Luminosity

The luminosity is needed for the absolute cross section measurements. Its uncertainty will enter directly in the final result, and is expected to be about 10% at the beginning of the LHC data-taking. It is the largest systematic uncertainty for the cross section measurements.

7.6.4 Summary

All the estimated relative systematic uncertainties are summarized in table 7.4. The main source of uncertainty is expected from the luminosity measurement. The uncertainties highly depend on the dimuon mass range. The selection is expected to have leading effects in the low mass region, while the alignment, especially between the tracker and muon systems, is expected to have the highest uncertainty in the high mass region.

Source	Uncertainty (%)
Selection efficiency	~ 2.0
Offline efficiency	~ 1.0
Magnetic field	~ 0.1
Alignment	~ 1.0
Trigger efficiency	~ 1.0
Total experiment	~ 2.5
Total theory	~ 5.0
Luminosity	~ 10.0
Total	~ 12.0

Table 7.4
Relative systematic uncertainties on the Drell-Yan dimuon cross section measurement.

7.7 Cross Section Measurement

In figure 7.16 the invariant mass spectrum of the dimuon system after all selection cuts is shown both in linear and logarithmic scales. It can be observed that all the selection cuts have been very effective in reducing the QCD events mainly in the low mass region and $t\bar{t}$+jets background in the higher mass region respectively. Figure 7.17 shows the unfolded distribution.

7.7.1 Measurement of the Differential Cross Section

After unfolding the invariant mass distribution the differential Drell-Yan cross section for each mass bin is calculated by using the formula:

$$(\frac{d\sigma}{dM})_i = \frac{N_i}{\epsilon A \mathcal{L} \Delta M_i}. \tag{7.2}$$

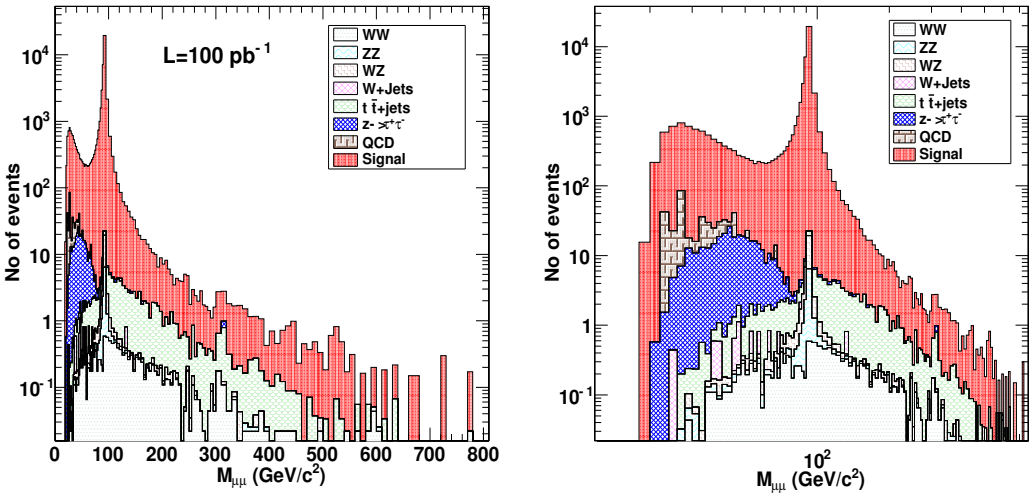

Figure 7.16. Invariant mass of two muons passing all selection cuts on a linear scale (left) and on a log(x) scale (right).

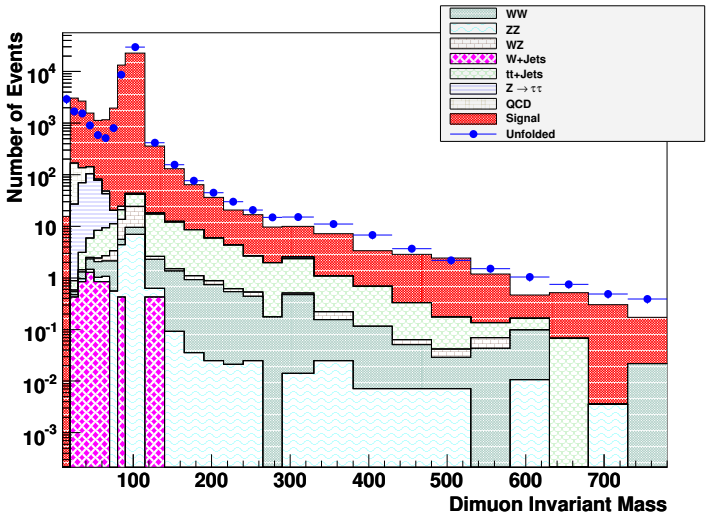

Figure 7.17. Invariant mass of two muons passing all selection cuts after unfolding. Solid points on top of the curves denote the unfolded distribution.

where ϵ is the total efficiency $\epsilon \equiv \epsilon_{\text{online}}\epsilon_{\text{offline}}\epsilon_{\text{selection}}$, A is the detector acceptance which can be estimated by simulation, $\mathcal{L}$ is the integrated luminosity, and N_i is the number of observed events in bin i.

The resulting Drell-Yan mass spectrum is compared with the SM expectations, as shown in figure 7.18.

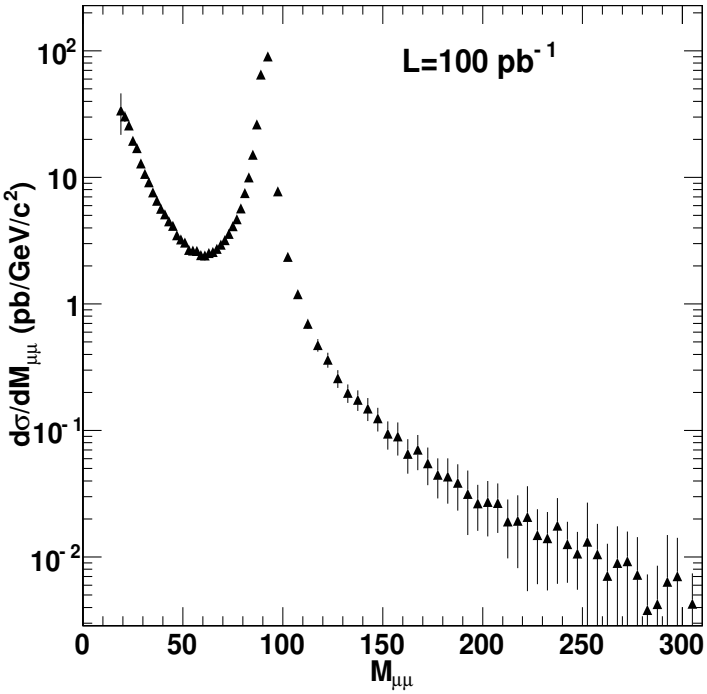

Figure 7.18. The Drell-Yan differential cross section.

7.7.2 Spectrum Normalized to the Z-Boson

The method of cross section measurement discussed so far depends on the knowledge of the absolute luminosity, which is expected to have large uncertainty. There is also an alternative approach to utilize the large cross section at the Z peak as a normalization for the theory predictions. As the number of events at the Z is large compared to the high-mass "tail", this approach can provide an anchor independent of luminosity measurements [78, 79].

A *ratio* method can be used in order to reduce the systematic uncertainties both on the experimental and theory sides. The number of observed events for a given bin in invariant mass is

$$N_{obs} = \mathcal{L} \cdot \sigma \cdot \varepsilon \tag{7.3}$$

where $\mathcal{L}$ is the integrated luminosity, σ is the differential cross section for the given mass bin, and ε counts the effective experimental efficiency including detector acceptance and smearing. Defining the Z peak region (80–100 GeV) as the zeroth *normalization* bin, the experimental ratios can be defined as:

$$R_i^{DATA} = \frac{N_i^D}{N_0^D} = \frac{\sigma_i^D \cdot \varepsilon_i^D}{\sigma_0^D \cdot \varepsilon_0^D}. \tag{7.4}$$

In this ration the luminosity cancels and only the shape of the cross sections and efficiencies as functions of invariant mass are important, which is a much smaller effect.

7.8 Summary

Various aspects of the measurement of the Drell-Yan cross section and the full mass spectrum in the dimuon channel with the CMS detector have been studied. Efficient signal selection and background rejection in the different mass ranges were examined and data-driven methods to measure trigger and offline efficiencies were tested. It was demonstrated that for collisions at $\sqrt{s} = 10$ TeV and an integrated luminosity of 100 pb^{-1}, the CMS detector can provide a clean first measurement of the Drell-Yan production cross section with a precision of $5\% \oplus$ luminosity uncertainty. The systematic uncertainty will be dominated by the luminosity measurement, but can be reduced by the ratio method utilizing large statistics of the Z resonance.

8. CONCLUSIONS

In order to prepare for challenging physics analysis at the LHC, the CMS detector was designed with a robust and sophisticated muon detection system, including the offline muon reconstruction software and the high-level trigger system. The performance of the muon reconstruction and the high-level trigger system is validated by Monte Carlo samples and real data taken during cosmic runs to have high efficiencies and good resolutions. The efficiency of global muon reconstruction is generally over 98%, and the resolution is a few percent up to a few hundred GeV.

The capacity of the physics potential of the CMS detector is demonstrated by real physics measurements using cosmic ray muons. Measurements of the muon charge ratio and absolute muon flux are performed using cosmic ray data collected during October and November 2008. Events with high-quality muons traversing the detector are selected. The cosmic muons are triggered and reconstructed by dedicated configurations and software components. Trigger and reconstruction efficiencies are estimated by dedicated data-driven methods. The measurements are performed within the detector volume first and then propagated to the earth's surface. The charge ratio of positive to negative muons is measured to be 1.26 ± 0.184 for muons with momentum $35 - 60$ GeV and 1.328 ± 0.207 for muons with momentum above 360 GeV, indicating a slight increasing trend. The muon flux weighted by p^3 is measured to be about 0.3 $\mathrm{GeV}^2\ \mathrm{cm}^{-2}\ \mathrm{s}^{-1}\ \mathrm{sr}^{-1}$. A peak around 100 GeV followed by a decreasing spectrum at high momentum is observed. Results of those measurements have shown reasonable agreements with previous experiments and is able to contribute the theoretical calculation. The uncertainties are dominated by the understanding of the molasse material shielding the CMS detector.

In preparation for first collisions at the LHC a study of the Drell-Yan dimuon cross section measurement using the first 100 pb^{-1} data from the LHC has been performed.

It has be demonstrated that this measurement will improve our understanding of electroweak physics as well as shed a light on the search for new high mass dimuon resonances. Trigger and reconstruction efficiencies are estimated by dedicated data-driven methods. Different sources of uncertainties and methods to control the effects of uncertainties are discussed. The uncertainty of the cross section measurement is dominated by the uncertainty of the luminosity measurement, which is expected to be about 10%.

The LHC has produced its first collisions successfully in 2009. In the near future, first data in a previously unexplored energy regime will be available, which makes exciting discovery possible. Future physics analyses will benefit from the efforts in the physics commissioning that is partly presented in this thesis.

LIST OF REFERENCES

LIST OF REFERENCES

[1] D. Griffiths. *Introduction to Elementary Particles*. Weinheim, USA: Wiley-VCH (2008) 454p.

[2] F. Halzen and Alan D. Martin. *Quarks and Leptons: an Introductory Course in Modern Particle Physics*. New York, USA: Wiley (1984) 396p.

[3] D. H. Perkins. *Introduction to High-Energy Physics*. Reading, USA: Addison-wesley (1982) 437p.

[4] S. L. Glashow. Partial Symmetries of Weak Interactions. *Nucl. Phys.*, 22:579–588, 1961.

[5] S. L. Glashow, J. Iliopoulos, and L. Maiani. Weak Interactions with Lepton-Hadron Symmetry. *Phys. Rev.*, D2:1285–1292, 1970.

[6] S. Weinberg. A Model of Leptons. *Phys. Rev. Lett.*, 19:1264–1266, 1967.

[7] M. Gell-Mann. A Schematic Model of Baryons and Mesons. *Phys. Lett.*, 8:214–215, 1964.

[8] H. Fritzsch, M. Gell-Mann, and H. Leutwyler. Advantages of the Color Octet Gluon Picture. *Phys. Lett.*, B47:365–368, 1973.

[9] D. J. Gross and F. Wilczek. Ultraviolet Behavior of Non-Abelian Gauge Theories. *Phys. Rev. Lett.*, 30:1343–1346, 1973.

[10] H. D. Politzer. Reliable Perturbative Results for Strong Interactions? *Phys. Rev. Lett.*, 30:1346–1349, 1973.

[11] P. W. Higgs. Broken Symmetries, Massless Particles and Gauge Fields. *Phys. Lett.*, 12:132–133, 1964.

[12] P. W. Higgs. Spontaneous Symmetry Breakdown without Massless Bosons. *Phys. Rev.*, 145:1156–1163, 1966.

[13] J. Pumplin et al. New Generation of Parton Distributions with Uncertainties from Global QCD Analysis. *JHEP*, 07:012, 2002.

[14] S. D. Drell and Tung-Mow Yan. Massive Lepton Pair Production in Hadron-Hadron Collisions at High-Energies. *Phys. Rev. Lett.*, 25:316–320, 1970.

[15] J. C. Collins and D. E. Soper. Angular Distribution of Dileptons in High-Energy Hadron Collisions. *Phys. Rev.*, D16:2219, 1977.

[16] J. D. Lykken. Introduction to Supersymmetry. 1996. hep-th/9612114.

[17] A. Einstein. On the Electrodynamics of Moving Bodies. *Annalen Phys.*, 17:891–921, 1905.

[18] Th. Kaluza. On the Problem of Unity in Physics. *Sitzungsber. Preuss. Akad. Wiss. Berlin (Math. Phys.)*, 1921:966–972, 1921.

[19] O. Klein. Quantum Theory and Five-Dimensional Theory of Relativity. *Z. Phys.*, 37:895–906, 1926.

[20] N. Seiberg and E. Witten. String Theory and Noncommutative Geometry. *JHEP*, 09:032, 1999.

[21] E. Witten. Solutions of Four-Dimensional Field Theories via M-Theory. *Nucl. Phys.*, B500:3–42, 1997.

[22] Nima Arkani-Hamed, Savas Dimopoulos, and G. R. Dvali. The Hierarchy Problem and New Dimensions at a Millimeter. *Phys. Lett.*, B429:263–272, 1998.

[23] Nima Arkani-Hamed, Lawrence J. Hall, David Tucker-Smith, and Neal Weiner. Solving the Hierarchy Problem with Exponentially Large Dimensions. *Phys. Rev.*, D62:105002, 2000.

[24] Panagiota Kanti, Keith A. Olive, and Maxim Pospelov. Solving the Hierarchy Problem in Two-Brane Cosmological Models. *Phys. Rev.*, D62:126004, 2000.

[25] Bobby Samir Acharya, Konstantin Bobkov, Gordon Kane, Piyush Kumar, and Diana Vaman. An M-Theory Solution to the Hierarchy Problem. *Phys. Rev. Lett.*, 97:191601, 2006.

[26] Yosef Nir. Gauge Unification, Yukawa Hierarchy and the Mu Problem. *Phys. Lett.*, B354:107–110, 1995.

[27] Merab Gogberashvili. Hierarchy Problem in the Shell-Universe Model. *Int. J. Mod. Phys.*, D11:1635–1638, 2002.

[28] Andrew G. Cohen and David B. Kaplan. Solving the Hierarchy Problem with Noncompact Extra Dimensions. *Phys. Lett.*, B470:52–58, 1999.

[29] Z. Chacko and Ann E. Nelson. A Solution to the Hierarchy Problem with an Infinitely Large Extra Dimension and Moduli Stabilization. *Phys. Rev.*, D62:085006, 2000.

[30] J. L. Hewett and M. Spiropulu. Particle Physics Probes of Extra Spacetime Dimensions. *Ann. Rev. Nucl. Part. Sci.*, 52:397–424, 2002.

[31] L. Randall and R. Sundrum. A Large Mass Hierarchy from a Small Extra Dimension. *Phys. Rev. Lett.*, 83:3370–3373, 1999.

[32] E. Witten. Anti-de Sitter Space and Holography. *Adv. Theor. Math. Phys.*, 2:253–291, 1998.

[33] R. Adolphi et al. The CMS Experiment at the CERN LHC. *JINST*, 0803:S08004, 2008.

[34] The CMS Collaboration. The CMS Physics Technical Design Report Volume 1. *CERN-LHCC-2006-001*, 2006.

[35] The CMS Collaboration. The Magnet Project: Technical Design Report. *CERN/LHCC 97-10*, 1997.

[36] P. Sphicas et al. CMS: The TriDAS Project. Technical Design Report, Vol. 2: Data Acquisition and High-Level Trigger. CERN-LHCC-2002-026.

[37] W. Adam et al. The CMS High Level Trigger. *Eur. Phys. J.*, C46:605–667, 2006.

[38] Bjarne Stroustrup. *The C++ Programming Language (Special Edition ed.)*. 2009. Addison-Wesley, ISBN 0-201-70073-5.

[39] `http://www.python.org`.

[40] R. Brun, F. Rademakers, and S. Panacek. ROOT, an Object Oriented Data Analysis Framework. Prepared for CERN School of Computing (CSC 2000), Marathon, Greece, 17-30 Sep 2000.

[41] R. K. Bock H. Grote R. Fruhwirth, M. Regler. *Data Analysis Techniques for High-Energy Physics*. Cambridge University Press, second edition, 2000.

[42] C. Amsler et al. Review of Particle Physics. *Phys. Lett.*, B667:1, 2008.

[43] V. Drollinger. Simulation of Beam-Halo and Cosmic Muons. CMS-NOTE-2006-012.

[44] W. Adam et al. Track Reconstruction with Cosmic Ray Data at the Tracker Integration Facility. CMS-NOTE-2009-003.

[45] The CMS Collaboration. Measuring Electron Efficiencies at CMS with Early Data. CMS-AN-2007-019.

[46] R. Fruhwirth. Application of Kalman Filtering to Track and Vertex Fitting. *Nucl. Instrum. Meth. A*, 262, 1987.

[47] K. Hoepfner P. Biallass, T. Hebbeker. Simulation of Cosmic Muons and Comparison with Data from the Cosmic Challenge Using Drift Tube Chambers. CMS-NOTE-2007-024.

[48] S. Agostinelli et al. GEANT4: A Simulation Toolkit. *Nucl. Instrum. Meth.*, A506:250–303, 2003.

[49] M. Chen et al. Measurement of the Charge Ratio in Cosmic Rays Using Global Muon Reconstruction in CRAFT Data. CMS-NOTE-2009-102.

[50] P. Avery et al. Measurement of the Cosmic Muon Flux Using CRAFT Data. CMS-NOTE-2009-150.

[51] M. J. Tannenbaum. Comparison of Two Formulas for Muon Bremsstrahlung. CERN-PPE-91-134.

[52] R. Bellotti et al. Study of High-Energy Cosmic Rays through the Measurement of the Electromagnetic and TeV Muon Components of Extensive Air Showers by EAS-TOP and MACRO. Contributed to the Int. Cosmic Ray Conf., Dublin, Ireland, Aug 11-23, 1991.

[53] L. G. Bugel et al. Measuring the Energy of Cosmic Ray Muons in a Sampling Calorimeter. *Williamsburg 1996, Particles and Nuclei 711-712*.

[54] P. Amaral et al. A Precise Measurement of 180 GeV Muon Energy Losses in Iron. *Eur. Phys. J.*, C20:487–495, 2001.

[55] A. Airapetian et al. ATLAS Calorimeter Performance. CERN-LHCC-96-40.

[56] S. R. Kelner, R. P. Kokoulin, and A. A. Petrukhin. Direct Production of Muon Pairs by High-Energy Muons. *Phys. Atom. Nucl.*, 63:1603–1611, 2000.

[57] Yu. M. Andreev and E. V. Bugaev. Muon Bremsstrahlung on Heavy Atoms. *Phys. Rev.*, D55:1233–1243, 1997.

[58] T. Hebbeker and C. Timmermans. A Compilation of High Energy Atmospheric Muon Data at Sea Level. *Astropart. Phys. 18 (2002) 107*.

[59] P. Adamson et al. Measurement of the Atmospheric Muon Charge Ratio at TeV Energies with MINOS. *Phys. Rev.*, D76:052003, 2007.

[60] C. Liu et al. Reconstruction of Cosmic and Beam-Halo Muons with the CMS Detector. *Eur. Phys. J. C (2008) 56: 449 460*, 2008.

[61] G. Cowan. A Survey of Unfolding Methods for Particle Physics. Prepared for Conference on Advanced Statistical Techniques in Particle Physics, Durham, England, 18-22 Mar 2002.

[62] K. Hoepfner. Simulation of Cosmics Rays: Status, Samples and Plans. International CMS Workshop on cosmic ray data analysis, 11-13 March 2009.

[63] M. Aldaya and P. Garcia-Abia. Measurement of the Charge Ratio of Cosmic Muons Using CMS Data. CMS-NOTE-2008-016.

[64] R. Engel, T. K. Gaisser, and T. Stanev. Pion Production in Proton Collisions with Light Nuclei: Implications for Atmospheric Neutrinos. *Phys. Lett.*, B472:113–118, 2000.

[65] P. Achard et al. Measurement of the Atmospheric Muon Spectrum from 20 GeV to 3000 GeV. *Phys. Lett.*, B598:15–32, 2004.

[66] D. Bourilkov et al. Towards a Measurement of the Drell-Yan Production Cross Sections in pp Collisions at $\sqrt{s} = 10$ TeV with Di-muons in CMS. CMS-AN-2009-151.

[67] T. Sjostrand, S. Mrenna, and P. Skands. PYTHIA 6.4 Physics and Manual. *JHEP*, 05:026, 2006.

[68] C. M. Carloni Calame, G. Montagna, O. Nicrosini, and A. Vicini. Precision Electroweak Calculation of the Production of a High Transverse-Momentum Lepton Pair at Hadron Colliders. *JHEP*, 10:109, 2007.

[69] K. Mazumdar J.B. Singh M. Jindal, D. Bourilkov. Study of the Drell-Yan Process Using Horace Event Generator. CMS-AN-2009-113.

[70] Andreas Hocker and Vakhtang Kartvelishvili. SVD Approach to Data Unfolding. *Nucl. Instrum. Meth.*, A372:469–481, 1996.

[71] http://hepunx.rl.ac.uk/~adye/software/unfold/roounfold.html.

[72] https://twiki.cern.ch/twiki/bin/view/cms/triggertables.

[73] D. Bourilkov. Study of Parton Density Function Uncertainties with LHAPDF and PYTHIA at LHC. 2003. hep-ph/0305126.

[74] M. R. Whalley, D. Bourilkov, and R. C. Group. The Les Houches accord PDFs (LHAPDF) and LHAGLUE. 2005. hep-ph/0508110.

[75] D. Bourilkov, R. C. Group, and M. R. Whalley. LHAPDF: PDF Use from the Tevatron to the LHC. 2006. hep-ph/0605240.

[76] M. Chen et al. Search for New High-Mass Resonances Decaying to Muon Pairs in the CMS Experiment. CMS-NOTE-2007-038.

[77] K. Melnikov and F. Petriello. Electroweak Gauge Boson Production at Hadron Colliders through $O(\alpha(s)^2)$. *Phys. Rev.*, D74:114017, 2006.

[78] M. Dittmar, F. Pauss, and D. Zurcher. Towards a Precise Parton Luminosity Determination at the CERN LHC. *Phys. Rev.*, D56:7284–7290, 1997.

[79] D. Bourilkov. Compositeness Search with Di-muons in CMS. CMS-NOTE-2006-085.